

**HIGH-POWER HIGH-REPETITION-RATE 1- μ M FIBER
LASER SYSTEM FOR STRONG-FIELD PHYSICS AND MID-
INFRARED GENERATION**

DISSERTATION

Zur Erlangung des Doktorgrades

And der Fakultät für Mathematik, Informatik und Naturwissenschaften

Fachbereich Phsik

Der Universität Hamburg

vorgelegt von

YIZHOU LIU

B.S. in Electronic Science and Technology,

China University of Mining and Technology, 2012

M.E. in Electronics and Communication Engineering,

Peking University, 2015

Hamburg, October 2019

Gutachter der Dissertation

Prof. Dr. Franz X. Kärtner
Prof. Dr. Markus Drescher

Mitglieder der Prüfungskommission

Prof. Dr. Franz X. Kärtner
Prof. Dr. Ludwig Mathey
Prof. Dr. Andrea Cavalleri
Prof. Dr. Markus Drescher
Prof. Dr. Peter Schmelcher

Vorsitzender des Promotionsausschusses

Prof. Dr. Peter Schmelcher

Datum der Disputation

22.10.2019

STATEMENT OF ORIGINAL AUTHORSHIP

I hereby declare that this dissertation has been written solely by myself except where due reference is made. Any help that I have received in my research work and the preparation of the thesis itself has been acknowledged.

Yizhou Liu

Hamburg, October 2019

ABSTRACT

Because of their ultrashort pulse duration and extremely high peak power, interest in ultrashort pulse lasers for strong-field experiments has been rapidly increasing over the past decades. After the invention of passively mode-locked lasers, further developments of ultrashort pulses in achieving ultrashort pulse duration, extremely high peak power and phase stabilization enable scientists to do frontier research such as bio-imaging, astronomical spectroscopy, solid-state high-harmonic generation, optical-field-driven electron emission from nanostructures, light-matter interaction in new materials, etc. A breakthrough in pulse amplification of ultrashort laser pulses, including fiber lasers, to extremely high levels was accomplished through chirped-pulse amplification. High power fiber lasers realized by using large-mode-area photonic crystal gain fibers become popular in strong-field applications due their compactness, stability and perfect beam profile. Furthermore, high power fiber lasers can also serve as front-end lasers for subsequent solid-state laser amplifiers and nonlinear frequency conversion stages to enable applications such as high power mid-infrared generation, terahertz-driven linear electron acceleration, etc. High repetition rates are also a very important characteristic of ultrashort pulse lasers besides the pulse duration and the pulse peak power. This can extremely improve the photon flux and signal-to-noise ratio in many state-of-the-art strong-field experiments. However, especially in parametric amplifiers, realizing high repetition rate ultrafast lasers with high average power is still limited by the crystal size and remaining thermal effects.

The aim of this thesis is to develop and provide a roadmap to build well dispersion managed, high power, repetition rate tunable 1- μm all-fiber lasers and mid-infrared lasers based on nonlinear frequency conversion. Such lasers are heavily needed in strong-field applications. Here, we demonstrate a MHz-level fiber laser system with >55 μJ pulse energy using chirped-pulse amplification. The repetition rate system can be further tuned, here reduced, by applying an acousto-optic modulator. Amplified pulses at $\approx\text{ns}$ pulse duration can be compressed to near transform-limited duration with a grating pair compressor due to a well-engineered dispersion management. The method

of hundred-watts-level circularly polarized pre-chirp managed amplification is invented and proven for the first time in this thesis. This method indicates that the peak power of the circularly polarized pulse can be amplified to 1.5 times higher than the linearly polarized pulse accumulating the same nonlinear phase. We also applied the method of optical parametric amplification to generate high repetition rate mid-infrared lasers using the high repetition rate, high power, 1- μm lasers. μJ -level, few-cycle, passively CEP-stable, 2.1- μm pulses at MHz-level repetition rate have been generated in dispersion-managed OPAs. The broadband 2.1- μm seed is generated from the chirped-pulse DFG stage. Ideas for further experiments to generate high repetition rate mid-infrared sources with much longer wavelength are also presented in this thesis. Our work paves the way to construct high repetition rate ultrafast sources satisfying the needs of many applications requiring high optical intensities, high photon flux and high signal-to-noise ratio.

ZUSAMMENFASSUNG

Auf Grund der ultrakurzen Impulsdauern mit zugleich extremen Spitzenleistungen ist das Interesse an Ultrakurzimpulslasern für die Erforschung der Stark-Feld Physik in den letzten Jahrzehnten rapide gewachsen. Durch die Entwicklung des passiv modengekoppelten Lasers und der anschließenden technischen Weiterentwicklung, ist es routinemäßig möglich, ultrakurze Impulsdauern bei extremen Spitzenleistungen und zugleich optischer Phasenstabilität zu erreichen. Dies erschließt der Wissenschaft unzählige Anwendungsgebiete wie Bildgebung in lebender Materie, Spektroskopieverfahren in der Astronomie, Erzeugung hoher Harmonischer in Festkörpern, das Treiben von ultrakurzen Elektronen-Emissionsprozessen in Nanostrukturen oder der Licht-Materie Wechselwirkung in neuen Materialien. Ein Durchbruch in der Verstärkung ultrakurzer Laserimpulse, auch in Faserlasern, war die Entwicklung der Verstärkung gechirpter Impulse, welche extrem hohe Spitzenleistungen ermöglichte. Faserlaser mit hoher Durchschnittsleistung basieren auf dieser Technik und realisieren diese durch die Verwendung photonischer Kristall-Verstärkungsfasern mit großen Modenquerschnitten. Diese Systeme finden zahlreiche Anwendung in der Stark-Feld Physik aufgrund ihrer Kompaktheit, Zuverlässigkeit und Stabilität. Des Weiteren können Faserlaser mit hoher Spitzenleistung auch als Seedlaser für nachgeschaltete Festkörper-Verstärker oder als Vorstufen für nichtlineare Konversionsstufen dienen, die zur Erzeugung hoch intensiver Strahlung im mittleren Infraroten bis in den Terahertz-Bereich, mit Anwendungen in der Terahertz-getriebenen linearen Elektronenbeschleunigung, verwendet werden können. Neben den zuvor genannten Eigenschaften zeichnen sich die Lasersysteme auch durch hohe Repetitionsraten aus, die bei vielen Stark-Feld Experimenten zu extrem erhöhtem Photonenfluss und verbessertem Signal-zu-Rausch Verhältnis beitragen. Nichtsdestotrotz ist es immer noch eine technische Herausforderung parametrische Verstärker, mit ultrakurzen Impulsen, hoher Repetitionsrate und vor allem hoher Durchschnittsleistung zu realisieren, da thermische Effekte an Einfluss und Kristallgröße gewinnen.

Das Ziel dieser Arbeit ist es daher, eine Richtlinie für die Entwicklung eines dispersionsangepassten Faserlasers mit hoher Durchschnittsleistung bei $1\mu\text{m}$ Wellenlänge und variabler Repetitionsrate zu liefern. Des Weiteren soll gezeigt werden, wie dieser als Pumpquelle für die Erzeugung von ultrakurzen Impulsen im mittleren Infrarot-Bereich durch nichtlineare Frequenzkonversion dienen kann. Solche Quellen werden dringend für Stark-Feld Experimente benötigt. In dieser Arbeit wird ein Faserlasersystem mit MHz Repetitionsrate und Impulsenergie $>55\ \mu\text{J}$ basierend auf der Methode der Verstärkung gechirpter Impulse demonstriert. Die Repetitionsrate kann zudem, durch einen akusto-optischen Modulator flexibel eingestellt werden. Durch die speziell designte Dispersion im System können die verstärkten Impulse mit Nanosekunden-Impulsdauern auf den Bandbreite-limitierten Wert mit einem Gitter-Kompressor reduziert werden. Außerdem wurde die neuartige Methode der pre-Chirp-angepassten Verstärkung von zirkular polarisiertem Licht erfunden und demonstriert. Diese Methode erlaubt es, 1.5-fach höhere Spitzenleistung bei gleicher nichtlinearer Phase, im Vergleich zu linear polarisierter Verstärkung, zu erzeugen. Außerdem, basierend auf optisch parametrischer Verstärkung wird ein Schema zur Erzeugung von Impulsen bei einer Wellenlänge von $2.1\text{-}\mu\text{m}$ bei MHz-Repetitionsrate demonstriert. Diese Impulse sind zudem passiv stabil in der Trägereinhüllenden-Phase und können auf ihr Bandbreitelimit komprimiert werden, wodurch sie nur noch wenige Lichtzyklen aufweisen. Der breitbandige $2.1\text{-}\mu\text{m}$ Seedimpuls wird in einer gechirpten Differenzfrequenzstufe erzeugt. Konzepte zur Erzeugung von noch längerwelliger Infrarotstrahlung werden ebenfalls aufgezeigt. Diese Arbeit demonstriert abschließend einen Weg zur Erzeugung ultrakurzer Impulse mit hoher Repetitionsrate, die den Anforderungen von vielen Stark-Feld Experimenten genügen, die hohe Intensitäten, hoher Photonenfluss und hohes Signal-zu-Rausch Verhältnis benötigen.

ACKNOWLEDGEMENTS

I would like to acknowledge all of those who helped and encouraged me along my research journey. I would like to also acknowledge the China Scholarship Council for funding my 4 years of study at Universität Hamburg.

First and most, I would like to thank my supervisors Professors Franz X. Kärtner and Guoqing Chang, who provided me with the opportunity to realize my dream in developing high power ultrafast lasers, and Dr. Phillip Keathley, Dr. Peter Krogen, Dr. Michaël Hemmer and Dr. Mikhail Pergament who trained me and gave me countless valuable suggestions for my experiments. Furthermore, I would give my most gratitude to my parents who encouraged and supported me to pursue my interests in physics through the decades of schooling needed to make this all possible. I would also thank all of my colleagues who have been involved in these laser development projects, in particular, Dr. Ming Xin, Dr. Hüseyin Çankaya, Dr. Kemal Shafak, Dr. Gengji Zhou, Dr. Yudong Yang, Qian Cao, Yi Hua and Anan Dai. It would not have been possible for me to achieve the experimental results without their help. Finally, I want to give my most heartfelt thanks to my wife Linxu Zhu, who is always there waiting for me and encouraging me.

PUBLICATION LIST

Publications in refereed journals

1. Y. Liu, P. Krogen, K.-H. Hong, Q. Cao, P. Keathley, and F. X. Kärtner, "Fiber-amplifier-pumped, 1-MHz, 1- μ J, 2.1- μ m, femtosecond OPAs with chirped-pulse DFG front-end," *Opt. Express* 27(6), 9144-9154, 2019.
2. Y. Liu, Y. Hua, S. M. Mohamadi, M. Pergament, F. X. Kärtner, "10-Hz, 636-ps, 1064-nm, all polarization maintaining fiber front-end based on fast optical pulse chopping," manuscript in preparation.

Publications in refereed conferences

1. Y. Liu, W. Liu, D. Schimpf, T. Eidam, J. Limpert, A. Tünnermann, F. X. Kärtner, and G. Chang, "Energy scaling of pre-chirp managed nonlinear amplification using circular polarization," 7th EPS-QEOD Europhoton Conference, 2016.
2. Y. Liu, W. Liu, D. Schimpf, T. Eidam, J. Limpert, A. Tünnermann, F. X. Kärtner, and G. Chang, "100-W few-cycle Yb-fiber laser source based on pre-chirp managed amplification employing circular polarization," ASSL, paper JTh2A.38, 2016.
3. W. Liu, Y. Liu, D. Schimpf, T. Eidam, J. Limpert, A. Tünnermann, F. X. Kärtner, and G. Chang, "Pre-chirp managed nonlinear amplification for >100-W ultrafast sources," The 8th International Symposium on Ultrafast Phenomena and Terahertz Waves, paper IW2C.1, 2016.
4. G. Zhou, M. Xin, Y. Liu, F. X. Kärtner, and G. Chang, "SPM-enabled fiber laser source beyond 1.2 μ m," ASSL, Page ATh1A.4, 2016.
5. Q. Cao, C. Li, Y. Liu, X. Gao, Z. Zhang, F. X. Kärtner, and G. Chang, "Passively Offset-free Yb: fiber Laser Source with 1 GHz Repetition Rate," CLEO: QELS_Fundamental Science 2016, Page JTh2A.141, 2016.
6. Y. Liu, P. Krogen, D. Schimpf, G. Chang, P. Keathley, and F. X. Kärtner, "Compact, 200 MW Peak Power, 1 μ m Source With All-fiber Front-End," CLEO Pacific Rim 2018, paper W1G. 3, 2018.
7. L. E. Zapata, S. Schweisthal, J. Thesinga, C. Zapata, M. Schust, Y. Liu, M. Pergament, and F. X. Kärtner, "Joule-class 500 Hz Cryogenic Yb: YAG Chirped Pulse Amplifier," CLEO: Science and Innovations 2019, Page SM4E.1, 2019.
8. Y. Liu, P. Krogen, K.-H. Hong, Q. Cao, P. Keathley, and F. X. Kärtner, "Compact 1-MHz, 1- μ J, Few-cycle, Passively CEP-stable 2- μ m Source," CLEO: Science and Innovations 2019, Page STh3E.5, 2019.

CONTENTS

Abstract	i
Zusammenfassung	iii
Acknowledgements	v
Publication list	vii
Contents	1
List of figures	3
List of tables	7
List of abbreviations	9
Foreword	11
Chapter 1: Introduction	13
1.1 Introduction of nonlinear optics.....	15
1.2 Fiber and fiber lasers.....	16
<i>1.2.1 Fibers</i>	16
<i>1.2.2 Nonlinear Schrödinger equation</i>	18
<i>1.2.3 Fiber lasers</i>	19
<i>1.2.4 Ultrafast, high power fiber lasers</i>	20
1.3 High power MIR generation.....	22
1.4 Structure of the thesis	24
Chapter 2: High-power all-fiber 1-μm CPA laser systems	27
2.1 Methods for fiber amplification	28
2.2 High power 1 μm all-fiber front end based on CPA	30
<i>2.2.1 28 MHz home-made stretched pulse mode-locked fiber oscillator</i>	31
<i>2.2.2 Home-made all fiber stretcher for broadband fiber amplification</i>	34
<i>2.2.3 Repetition rate Reducton module using an AOM</i>	39
<i>2.2.4 Dispersion management, spectral management and compression</i>	41
<i>2.2.5 Design of the fiber power amplifier and compressor</i>	43
2.3 Schematic Layout of the setup.....	46

2.4 Joule-class 500 Hz cryogenic Yb:YAG chirped pulse amplifier based on all-fiber front-end.....	47
2.5 Conclusions.....	50
Chapter 3: High-power femtosecond 1-μm circularly polarized pre-chirp managed amplification system	51
3.1 System layout of the 100-W 1- μ m laser system.....	52
3.2 Pre-CPA stage for CP-PCMA.....	53
3.3 Results and analysis of the CP-PCMA system.....	56
3.4 Schematic construction of the CP-PCMA system.....	64
3.5 Conclusions.....	65
Chapter 4: 1-MHz, 1-μJ, passively CEP-stable, femtosecond 2.1-μm OPA system ...	67
4.1 System layout of the 2.1- μ m OPA system	68
4.2 Broadband passively CEP-stable 2.1- μ m generation	69
4.2.1 Dispersive wave generation.....	69
4.2.2 The chirped pulse difference frequency generation	72
4.3 High repetition rate, μ J-level, femtosecond, 2.1- μ m OPA system.....	76
4.3.1 Schematic construction of the dispersion managed 2.1- μ m OPA system	78
4.3.2 Signal amplifier of the 2- μ m signal pulses.....	80
4.3.3 Power amplifier for the 2- μ m signal pulses.....	82
4.4 Schematic Layout of the 2- μ m system	87
4.5 Conclusions.....	88
Chapter 5: Conclusion and outlook.....	91
5.1 Further improvement and applications of the 1- μ m system.....	92
5.2 Further improvement and applications of the 2.1- μ m system	94
Bibliography.....	97

LIST OF FIGURES

Figure 1. 1: Nonlinear susceptibility and its corresponding nonlinear process.....	16
Figure 1. 2: Simple construction of the optical fiber.....	17
Figure 1. 3: Typical pulse energies achieved with different amplifier technologies.....	21
Figure 1. 4: System layout of the ultrafast CPA system.	22
Figure 1. 5: System layout of second order nonlinear process.....	23
Figure 2. 1: Schematic constructions of the CPA (a) and DPA (b).	29
Figure 2. 2: Schematic constructions of the CPPA (a) and PCMA (b).	30
Figure 2. 3: System layout of the home-built 1 MHz 1 μm CPA system.....	31
Figure 2. 4: Schematic layout of the home-built 28 MHz oscillator and the corresponding output spectrum.	33
Figure 2. 5: Layout of the general stretcher.	34
Figure 2. 6: Schematic construction of the 5-nm four-CFBG fiber stretcher.	35
Figure 2. 7: Pulse profile of the stretched pulse with 3.6 ns pulse width.....	36
Figure 2. 8: (a) Picture of the 41.3-MHz oscillator, (b) picture of the CFBG stretcher.	37
Figure 2. 9: Schematic layout of the all-fiber 4-pass stretcher.	38
Figure 2. 10: Pulse profile of the stretched pulses after the stretcher taken from sampling oscilloscope.....	39
Figure 2. 11: Layout of an acousto-optic modulator used as optical pulse picker.....	40
Figure 2. 12: Schematic layout of the repetition rate reduction module.....	41
Figure 2. 13: Simulation results for compression and its effect on spectral content.....	42
Figure 2. 14: Output beam profile after rod-type fiber amplifier.	44
Figure 2. 15: Schematic construction of the rod-type fiber amplifier and compressor....	45
Figure 2. 16: Final output results of the 1- μm laser source.	46
Figure 2. 17: Calculated 186×1.4 fs transform-limited intensity auto-correlation trace.	46
Figure 2. 18: Pictures of the home-build high power 1-MHz 1- μm laser source.....	46
Figure 2. 19: Schematic construction of the 1- μm laser source.	47

Figure 2. 20: Spectra of the seed pulse (red dashed curve) and amplified pulse after regenerative amplifier (black curve). The inset picture is the beam profile after the amplifier.....	48
Figure 2. 21: Picture of mJ-level regenerative amplifier.....	48
Figure 2. 22: (a) Picture of the 12-pass cryogenic Yb:YAG composite-thin-disk amplifier, (b) Picture of the Joule-class 500-Hz 16-pass cryogenic Yb:YAG composite-thin-disk amplifier.....	49
Figure 2. 23: The ~ 18 mm beam shows a supergaussian near-field profile, diffraction limited spot (plus some scatter) is in the inset picture of the far-field.....	49
Figure 3. 1: System layout of the home-built 100-W 1- μ m laser source.....	53
Figure 3. 2: Schematic construction of the pre-CPA stage for CP-PCMA.....	54
Figure 3. 3: Spectrum of the seed pulse output from the 24-MHz oscillator.	55
Figure 3. 4: (a) Spectrum of the clipped amplified seed pulse; (b) Calculated intensity auto-correlation trace and measured intensity auto-correlation trace.	56
Figure 3. 5: Schematic layout of the CP-PCMA using the rod-type fiber amplifier.	56
Figure 3. 6: Spectra and intensity auto-correlation trace of the amplified negatively pre-chirped seed pulses with linearly polarization and circularly polarization.....	58
Figure 3. 7: Spectrum of the 100 W amplified negatively pre-chirped pulse and its intensity auto-correlation trace.....	59
Figure 3. 8: Spectra of the 40 W linearly polarized pulse, 60 W circularly polarized pulse and 60W linearly polarized pulse.	60
Figure 3. 9: (a) Spectra of the negatively pre-chirped 75 W circularly polarized pulse with different input power; (b) Spectra of the positively pre-chirped 75 W circularly polarized pulse with different input power.....	61
Figure 3. 10: (a) Calculated spectra of the negatively pre-chirped 95 W circularly polarized pulse with different input power; (b) Calculated spectra of the positively pre-chirped 95 W circularly polarized pulse with different input power.	62
Figure 3. 11: (a) Calculated auto-correlation trace of the compressed negatively pre-chirped pulse; (b) Calculated auto-correlation trace of the compressed positively pre-chirped pulse.....	63
Figure 3. 12: (a) Calculated amplified output power (red dashed curve) and related pump power (blue dashed curve) during the process of the amplification; (b) Gain curve of the rod-type fiber amplifier.....	63

Figure 3. 13: Schematic construction of the 100-W 1- μm CP-PCMA system.	64
Figure 3. 14: Picture of the home-build 100-W experimental setup.....	65
Figure 4. 1: System layout of the 2- μm OPA system.	68
Figure 4. 2: (a) 3D Spectral evolution inside the photonic crystal fiber HNF 945; (b) The output spectrum after the 1- μm pulse propagating through 4.3 cm distance inside the HNF 945.	69
Figure 4. 3: (a) Schematic construction of the dispersive wave generation; (b) Photonics crystal fiber structure [133].....	71
Figure 4. 4: (a) Spectrum of the 1- μm pulse; (b) Spectrum of the generated dispersive wave.....	71
Figure 4. 5: (a) Sum frequency generation and (b) difference frequency generation.....	72
Figure 4. 6: Schematic construction of the chirped pulse difference frequency generation.	74
Figure 4. 7: (a) Schematic structure of the 1-mm type I BBO crystal; (b) Transmission spectrum of ta 1-cm thick BBO crystal [144].....	74
Figure 4. 8: (a) The spectrum of the generated broadband 2- μm pulse during the chirped pulse DFG in the 1-mm thick BBO crystal; (b) Numerically calculated spectrum of the chirped pulse DFG in the 1-mm thick BBO crystal.	76
Figure 4. 9: Principle scheme of the OPA process.....	77
Figure 4. 10: Schematic construction of the non-collinear interaction geometry.....	78
Figure 4. 11: Schematic construction of the dispersion managed 2- μm OPA system.....	79
Figure 4. 12: Construction layout of the 1st OPA stage.	80
Figure 4. 13: (a) Phase matching poling period for 2.1- μm laser inside the MgO:PPLN crystal working under 100 degree; (b) Transmission curve of the MgO:PPLN crystal [145].	81
Figure 4. 14: Spectrum of the 2- μm signal pulse (red curve) of the 1st stage OPA, spectrum of the 2- μm amplified pulse after the 1st stage OPA (black curve), the superfluorescence spectrum of PPLN OPA after blocking the 2.1 μm seed at 2 W pump power.	82
Figure 4. 15: Signal power versus pump power. Inset shows beam profile of the output signal beam.	82
Figure 4. 16: Spectrum of the 2- μm signal pulse (red dashed curve) of the 2nd stage OPA, spectrum of the 2- μm amplified pulse after the 2nd stage OPA (black curve).....	83

Figure 4. 17: Signal power versus pump power. Inset shows near-field beam profile of the output signal beam.....	84
Figure 4. 18: Schematic construction of the home-built interferometric auto-correlator.	85
Figure 4. 19: The calculated transform-limited IAC trace (blue curve) based on the output spectrum and the measured IAC trace (red curve) of the output pulses without compression.	85
Figure 4. 20: Calculation results by adding GDD and 10000 fs ³ to fit the measured results, (a) 0 fs ² , (b) -600 fs ² , (c) -1200 fs ² , (d) -1800 fs ²	86
Figure 4. 21: Calculation results by (a) adding -1200 fs ² GDD and 10000 fs ³ and (b) adding -1200 fs ² GDD and 0 fs ³ to fit measured results.....	86
Figure 4. 22: Calculation results of (a), (b) transform-limited IAC trace and electronic field of the pulse; (c), (d) adding -1200 fs ² and 0 fs ³ to the calculation; (e), (f) adding 0 fs ² and 10000 fs ³ to the calculation.....	87
Figure 4. 23: Schematic Layout of the overall passively CEP-stable, 1-MHz, μ J-level, 2- μ m system.	88
Figure 4. 24: Full wavelength range spectrum includes the 690 nm dispersive wave (red curve), 1035 nm pump laser (green curve), 2.1- μ m signal laser (blue curve) and 2.1- μ m output laser (black curve).....	89
Figure 5. 1: Schematic construction of DPA with the method of dividing the seed pulses with (a) PBS and (b) birefringent crystal.....	93
Figure 5. 2: Schematic construction of nonlinear compression with hollow core fiber. ..	94
Figure 5. 3: Schematic illustration showing optical excitation and charge extraction from the nanoantenna array in the experimental setup.	95
Figure 5. 4: Schematic construction of 6- μ m generation.	96

LIST OF TABLES

Table 2.1: Parameters of the 28 MHz Oscillator	33
Table 2.2: Parameters of the CFBG	36
Table 2.3: Dispersion parameters of the OFS stretcher fiber and PMSMF	38
Table 2.4: Parameters of the aeroGAIN-ROD module	44
Table 4.1: Phase matching conditions	73
Table 4.1: Dispersion parameters of different materials	79
Table 5.1: Summary of the HHG laser sources	94



LIST OF ABBREVIATIONS

AOM	acousto-optic modulator
ASE	amplified spontaneous emission
CFBG	chirped fiber Bragg grating
CPA	chirped-pulse amplification
CP-PCMA	circularly polarized pre-chirp managed amplification
CPPA	circularly polarized pulses amplification
DCF	dispersion compensation fiber
DFG	difference frequency generation
DPA	divided pulse amplification
EOM	electro-optic modulator
EUV	extreme ultraviolet
FBG	fiber Bragg grating
FOD	fourth order dispersion
FR	Faraday rotator
FWM	four-wave mixing
FWHM	full width at half maximum
GVD	group-velocity dispersion
GDD	group delay dispersion
HHG	high-harmonic generation
HNF	high nonlinear fiber
IAC	interferometric auto-correlation
LP-PCMA	linearly polarized pre-chirp managed amplification
MIR	mid-infrared

NIR	near-infrared
NPE	nonlinear polarization evolution
OPA	optical parametric amplification
OPCPA	optical parametric chirped pulse amplification
PBS	polarization beam splitter
PCF	photonic crystal fiber
PCMA	pre-chirp managed amplification
PM	polarization maintaining
PMSMF	polarization maintaining single-mode fiber
PMWDM	polarization maintaining wavelength division multiplexer
SFG	sum frequency generation
SMF	single-mode fiber
SNR	signal-to-noise ratio
SPM	self-phase modulation
SRS	stimulated Raman scattering
TOD	third-order dispersion
UV	ultraviolet
ZGP	zinc germanium phosphide

FOREWORD

“Knowledge is human nature”. For the past hundreds of years, based on the efforts of generations of scientists, scientific technologies and theories have developed in a fast and efficient way. The discovery of atomic structure, quantum mechanics, relativity, the photoelectric effect, the laser, etc enables human beings to have a better understanding of nature. The laser is one of the most famous inventions having an enormous influence on society. Starting from the 1950s, the laser experienced rapid development and became extremely useful for different kinds of applications because of its characteristics such as high field-intensity, coherence, short pulse duration, small divergent angle, narrow output spectrum, etc.

“Every field of nature is wonderful”. The word “LASER” is an acronym for “Light Amplification by Stimulated Emission of Radiation”. It is now used to indicate laser oscillators and sometimes also includes devices with laser amplifiers. The acronym was coined in 1957 by the laser pioneer Gordon Gould. In 1960, the pulsed ruby laser demonstrated by Theodore Maiman was the first laser device in the world [1]. The first gas laser device (a He-Ne laser) [2] and the first laser diode were also demonstrated in the same year. In the late 1980s, the development of semiconductor lasers made it possible to manufacture more efficient and durable semiconductor laser diodes, which were then used in low-power CD and DVD drives and fiber optical communication. In the 1990s, high-power thin-disk lasers and high-power fiber lasers were realized, which have been applied to the field of material processing, replacing CO₂ lasers and Nd: YAG

lasers. In the 2000s, due to the development of ultrafast nonlinear optics, laser sources with output wavelengths ranging from extreme ultraviolet to THz have been realized.

“By standing on the shoulders of giants,” more and more important scientific results are published by different groups with international collaboration in the field of ultrafast nonlinear optics and X-ray science. However, there are still fascinating ideas that have yet to be realized or further studied. The Deutsches Elektronen-Synchrotron (DESY) is one of the world’s leading international research centers in photon science, accelerator, particle and astroparticle physics. As a graduate student working here, I benefited a lot from these diverse fields of physics as well as international research environment and hope that my research further strengthens the overall research effort at DESY.

CHAPTER 1: INTRODUCTION

For the past decades, interest in using high power ultrafast laser pulses for strong-field experiments has been on the rise [3-7]. There are two key reasons for this. First, nonlinear optical interactions are more efficiently excited using laser pulses with extremely short durations. Second, because most of the pulse energy is accumulated in the central peak of the pulse, ultrafast laser pulses have extremely high peak power compared with long pulses, which can fulfil the requirements for high energy density in strong-field experiments.

Ultrafast laser sources have experienced rapid development after the invention of the passively mode-locked lasers, which exhibit broader optical spectra, shorter pulse duration and more stable phase-control. These improvements can be achieved by applying different methods illustrated in ultrafast nonlinear optics. For bio-imaging and astronomical spectroscopy, there were great breakthroughs in the past 20 years using phase-controlled broadband ultrafast laser sources [8,9]. Ultrashort pulses with few optical cycle pulse durations enabled scientists to do optical-field-driven electron emission on nanostructures and pump probe experiments to investigate electronic and molecular dynamics of light-matter interaction, chemical and biological process [10-12]. Due to improvements in phase-control and reducing timing jitters of ultrafast laser sources, scientific research using high-precision optical measurements has experienced substantial improvement [13,14]. The invention and development of the chirped-pulse amplification (CPA) and nonlinear compression enabled ultrafast optical pulse generation with extremely high peak power for further investigations in strong-field physics [3,15].

The creation of ultrafast laser sources that span different wavelength ranges are also a very important research area. Thanks to the developments in ultrafast nonlinear optics over the past decades, methods like optical parametric amplification (OPA)/ optical parametric chirped pulse amplification (OPCPA) [16,17], difference frequency generation (DFG), sum frequency generation (SFG) [18,19], high harmonic generation (HHG) [20-22], self-phase modulation (SPM) [23,24] and supercontinuum generation [25], have enabled laser scientists to realize ultrafast laser sources with short pulse duration operating over vastly different wavelength ranges. With the method of DFG and OPA/OPCPA, mid-infrared (MIR) ultrashort pulses can be generated from near-infrared (NIR) high power ultrafast laser sources (Ti:Sapphire laser, high power ytterbium fiber laser). With the method of HHG, the ultraviolet (UV)/ extreme ultraviolet (EUV) ultrashort pulses can be generated from the high power ultrafast NIR or MIR laser sources. With the method of SPM, the spectrum bandwidth of the ultrafast laser pulse can be broadened to create $\approx 200\text{-}400$ nm spectral bandwidth, and can be used to generate a tunable broadband ultrafast laser sources with a linear chirp. With the method of supercontinuum generation, the octave-spanning spectrum can be generated during the process. Applying the chirped mirror compressor, the pulse with the octave-spanning spectrum can be compressed to a single cycle pulse duration level.

High repetition rate is another important characteristic aiming to get a higher SNR, shorter response time and higher photon flux in strong-field experiments,. The acousto-optic modulator (AOM) and the electro-optic modulator (EOM) enable scientists to operate ultrafast laser sources with variable repetition rates. Operating the ultrafast laser source with a low repetition rate, it is easy to get higher pulse peak power with relatively low average power, which is good for nonlinear interaction experiments without requiring high photon flux. However, there will be problems in maintaining the stability of a low repetition rate oscillator. Realizing the long separation distance free-space delay stage for pulses with low repetition rate can lead to systematic instability. Furthermore, the relatively low photon flux of the ultrafast laser makes it very hard to obtain a high signal-to-noise ratio (SNR) regarding the low repetition rate. In contrast, operating the ultrafast laser source with high repetition rate, high-power ultrafast laser sources can enable scientific applications in several emerging areas, such as by improving the signal to noise ratio in attosecond time-resolved spectroscopy using high-harmonic generation (HHG), by avoiding space charge effects in photoelectron

spectroscopy [26-30], by increasing solid-state high-harmonic generation (HHG) photon flux [31,32], by studying electron and exciton dynamics in graphene [33,34], or by studying optical-field-driven electron emission from nanostructures [35-39].

Great advancements have been made in realizing these characteristics either in fiber lasers or solid-state lasers. Though both fiber and solid-state laser sources have an important influence on strong-field research, there are three main differences between the solid-state and fiber laser: (1) the power level; (2) the long term stability; and (3) the beam profile. Using multi-pass solid-state amplifiers and regenerative amplifiers, solid-state lasers can satisfy high power applications. Though the newly invented rod-type fiber amplifier significantly improved amplified average power up to 1000 kW [40], solid-state amplifiers still dominate high-power laser systems. Regardless of their lower output power level, fiber lasers have several advantages compared with solid-state lasers, such as compactness, long term stability and perfect Gaussian beam profile. Therefore, there is a proper way in building ultrafast high power laser sources using the fiber lasers as the seed laser and pre-signal-amplifiers and using the solid-state amplifiers as the power-amplifiers.

1.1 INTRODUCTION OF NONLINEAR OPTICS

This section is a brief introduction to concepts in nonlinear optics important to understanding the remainder of this thesis [41]. Besides industrial applications, ultrafast laser sources can also be applied for both fundamental research and applications such as nonlinear frequency conversion, high-order harmonic generation, and strong-field physics in gases, liquids and solids [42-44]. Ultrafast pulses with intense peak power modify the susceptibility of the optical media during propagation leading to nonlinear effects. The polarization P shown in equation 1.1.1 represents the material response during the nonlinear process when the optical frequency is far from the medium resonance. $\chi^{(n)}$ is the n^{th} -order susceptibility at optical frequencies, which is the $(n + 1)^{\text{th}}$ tensor. Figure 1.1 briefly illustrates the nonlinear processes corresponding to second and third order nonlinear susceptibility.

$$P = \epsilon_0 [\chi^{(1)} \cdot E + \chi^{(2)} : EE + \chi^{(3)} : EEE] \quad (1.1.1)$$

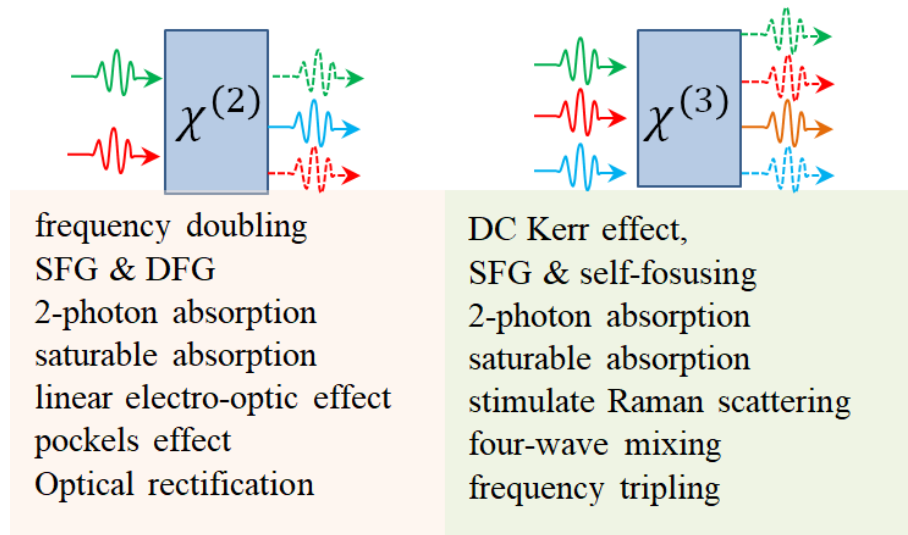


Figure 1. 1: Nonlinear susceptibility and its corresponding nonlinear process.

In anisotropic media, lacking the inversion symmetry enables the second order nonlinear susceptibility $\chi^{(2)}$ to imply important impacts in nonlinear processes. SFG, DFG, frequency doubling and parametric amplification can occur inside anisotropic media after fulfilling phase matching conditions. During these nonlinear processes, the pulse energy of pump pulses can be converted to generated idler pulses (SFG, DFG and frequency doubling) and even the signal pulses (parametric amplification).

In isotropic media, the inversion symmetry does not allow second-order processes meaning the lowest-order response of the nonlinear refractive index is a quadratic dependence on the electric field strength according to equation 1.1.2. Therefore, if an ultrafast pulse of sufficient peak intensity propagates through isotropic media, the peak part of the pulse receives a larger phase shift than the wings of the pulse, which results in SPM. Various types of nonlinearities can be expressed in terms of the real part and imaginary part of the third-order nonlinear susceptibility $\chi^{(3)}$. The real part of the susceptibility is associated with the refractive index. The imaginary part corresponds to irreversible processes in the material response giving rise to either loss or gain.

$$n = n_0 + \frac{3\chi^{(3)}}{8n_0} |E|^2 = n_0 + n_2 I \quad (1.1.2)$$

1.2 FIBER AND FIBER LASERS

1.2.1 FIBERS

Uncladded glass fibers were fabricated in the 1920s. The method of using a cladding layer to improve fiber characteristics was not invented until the 1950s, which can be considered as a generational shift in optical fiber technology. After the 1960s, fiber optics experienced rapid development. For the past decades, optical fibers became core components and widely used for optical communications and nonlinear fiber optics [45-49].

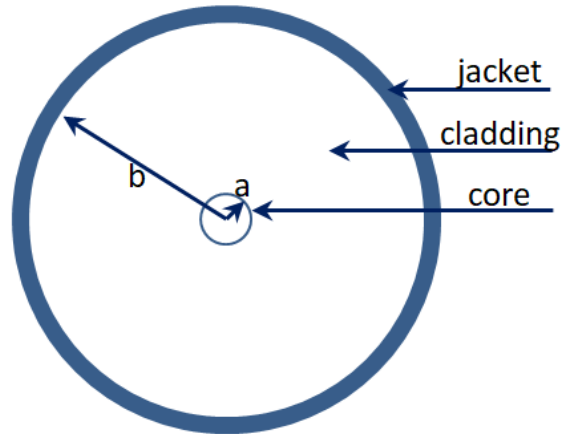


Figure 1. 2: Simple construction of the optical fiber.

Because of low propagation losses and high mechanical strength against pulling and bending, silica became the most common material for manufacturing optical fibers. The general construction of an optical fiber is shown in Figure 1.2. In this simple construction, the optical fiber consists of a glass core, a cladding layer with lower refractive index n_2 compared with core refractive index n_1 and a jacket to protect the fiber. The V parameter is defined in equation 1.2.1, where a is the core radius, and b is the cladding layer radius. The V parameter of step-index single-mode fiber (SMF) should be < 2.405 [50]. There are highly nonlinear fibers, polarization-maintaining fibers, large-mode-area fibers, rare-earth-doped fibers and multimode fibers designed for different applications. Some of these fibers belong to the group of photonic crystal fibers (PCFs) [51,52].

$$V = \frac{2\pi}{\lambda} a(n_1^2 - n_2^2)^{\frac{1}{2}} \quad (1.2.1)$$

A photonic crystal fiber (PCF) is a special type of optical fiber. It is fabricated by drawing fiber preforms prepared by stacking capillary tubes containing small air holes

with small diameters. By varying the arrangement of air holes, PCFs can be fabricated with customized properties [a-d]:

- a. Large- or small-mode area leading to weak or strong optical nonlinearities.
- b. Single-mode guidance in wide wavelength ranges.
- c. Unusual customized dispersion properties (abnormal dispersion in visible wavelength range).
- d. Air-guiding photonic bandgap fibers, with the light field dominantly propagating in the air hole.

1.2.2 NONLINEAR SCHRÖDINGER EQUATION

After propagating through an SMF, the optical output beam can be expressed as the fundamental mode of the fiber. Accumulated dispersion and nonlinearity of optical pulses during propagation need to be accounted for to accurately analyze the optical spectrum and pulse evolution inside fibers. In the normal dispersion region of fibers, lower frequency contents move faster than higher frequency contents leading to longer pulse duration for zero pre-chirped pulses. This is contrary to the anomalous dispersion region of fibers. When propagating negative pre-chirped pulses through a long piece of fiber in the normal dispersion region, the accumulated normal dispersion can compensate negative pre-chirp. Further, the normal dispersion of the remaining fiber can further stretch the pulse duration of the input pulses during propagation.

Due to the Kerr effect inside of isotropic fibers, nonlinear effects can also occur, such as SPM due to the nonlinear susceptibility $\chi^{(3)}$ stimulated Raman scattering (SRS), four-wave mixing (FWM), etc. The propagation equation can help us obtain a better understanding of the propagation processes inside fibers. The propagation equation is governed by Maxwell's equations, which were formulated by James Clerk Maxwell in the 1860s. Applying the slowly varying envelope approximation, the propagation equation of pulses propagating through fibers can be written as in equation 1.2.2 [53-55].

$$\begin{aligned} & \frac{\partial A}{\partial z} + \beta_1 \frac{\partial A}{\partial t} + \frac{i\beta_2}{2} \frac{\partial^2 A}{\partial t^2} - \frac{\beta_3}{6} \frac{\partial^3 A}{\partial t^3} + \frac{1}{2} \left(\alpha(\omega_0) + i\alpha_1 \frac{\partial}{\partial t} \right) A \\ & = i \left(\gamma(\omega_0) + i\gamma_1 \frac{\partial}{\partial t} \right) \left(A(z, t) \int_0^\infty R(t') |A(z, t - t')|^2 dt' \right) \end{aligned} \quad (1.2.2)$$

$\gamma(\omega_0) = n_2(\omega_0)(\omega_0)/cA_{\text{eff}}$ is the nonlinear parameter, γ_1 is the first order of Taylor's Formula of γ , $A_{\text{eff}} = (\iint_{-\infty}^{\infty} |F(x, y)|^2 dx dy)^2 / \iint_{-\infty}^{\infty} |F(x, y)|^4 dx dy$ is the effective core area, $F(x, y)$ is the modal distribution for the fundamental fiber mode and $R(t)$ is the nonlinear response function. In general, we can simplify equation 1.2.2 to equation 1.2.3. If α is equal to 0, equation 1.2.3 is identical to the nonlinear Schrödinger equation [53-55].

$$i \frac{\partial A}{\partial z} - \frac{\beta_2}{2} \frac{\partial^2 A}{\partial t^2} + \frac{i}{2} \alpha A + \gamma |A|^2 A = 0 \quad (1.2.3)$$

1.2.3 FIBER LASERS

Fiber lasers are usually meant to be lasers with rare-earth-doped fibers as gain media. Laser devices containing fiber components and fiber amplifiers can be called fiber lasers. In most cases, rare-earth-doped fibers are fibers doped with rare earth ions like erbium (Er^{3+}), neodymium (Nd^{3+}), ytterbium (Yb^{3+}), thulium (Tm^{3+}), or praseodymium (Pr^{3+}), which are three-level systems. Using rare-earth-doped fibers as gain media enables one to build fiber oscillators and fiber amplifiers [56,57]. Passively mode-locked fiber lasers applying the saturable absorption effect can be built using rare-earth-doped fibers as gain media [58]. Since rare-earth-doped fibers usually have broadband gain bandwidth, the output spectra of mode-locked fiber lasers can be also very broadband. With long-term stability and Gaussian output beam profile, compact mode-locked fiber oscillators are an attractive choice for seeding ultrafast lasers for applications [59-64]. In this thesis, we will focus on Yb-doped fiber lasers which emit in a typical wavelength range spanning 1020-1060 nm.

When ultrafast lasers propagate through optical media in oscillators or amplifiers, the dispersion should be carefully managed to make sure the output pulses can be compressed. The pulse duration of the output pulses from mode-locked fiber oscillators ranges from sub-ps to 10 ps corresponding to different mode locking regimes (i.e. soliton, stretched-pulse and all-normal) and different cavity structures (i.e. linear cavity using SESAM, ring cavity and figure 8 and figure 9 using nonlinear loop mirror). For 1- μm lasers pulses propagating inside SMF accumulate positive group-velocity dispersion (GVD) and positive third-order dispersion (TOD) [65,66]. However, there is also the dispersion compensating fiber like OFS stretcher fiber, which offers positive GVD and negative TOD at 1 μm [66-69]. There are optical components such as fiber Bragg gratings, reflection/transmission grating pairs, prism pairs and chirped mirrors, that can

be used as dispersion elements to provide designed chirp or compensate the chirp of chirped pulses.

Using rare-earth-doped fibers as gain media for fiber amplifiers [70-73], >30 dB small signal gain can be achieved using the Yb-doped gain fiber for small signal amplification offering a large optical alignment tolerance and reducing the complexity of system construction. Besides single-mode gain fibers and double-cladding large-core diameter gain fibers, newly invented rod-type photonic crystal gain fiber with tens of μm core diameters can easily scale the amplified output power up to hundreds of watts [74]. Inside fiber amplifiers, the pump beam and the signal beam can propagate in the same or opposite direction. Performance is nearly the same in these two pumping configurations when the signal power is small enough to make fiber amplifiers remain unsaturated. If fiber amplifiers work in the saturation regime, power-conversion efficiency is better in the backwards-pumping configuration because of lower amplified spontaneous emission [75].

1.2.4 ULTRAFAST, HIGH POWER FIBER LASERS

In October 2018, half of the Nobel Prize in physics was awarded to Arthur Ashkin for work on optical tweezer [76] and the other half jointly to Gérard Mourou and Donna Strickland for work on CPA [77]. Before the invention of CPA, the peak power of ultrafast laser pulses was limited by nonlinear processes such as the self-focusing effect. Laser pulses with optical intensities of GW/cm^2 can cause serious damage to optical media by the self-focusing effect. In order to keep the intensity of optical pulses below the damage threshold, laser systems had to be built on a large scale increasing their cost. Therefore, the peak power of optical pulses was limited to the GW level or TW level for very large multi-beam facilities. Applying the method of CPA, an ultrashort optical pulse can be stretched long enough to avoid intensities greater than the damage threshold inside the gain media, enabling high gain during amplification processes and extremely high peak power after compression. Gratings, prisms, grisms, chirped mirrors, fiber Bragg gratings (FBGs) and dispersion compensating fibers are ideal elements to stretch and compress high power ultrafast laser pulses. Besides CPA, the well-developed technique of divided-pulse amplification (DPA) is an alternative for amplifying optical pulses with relatively long durations (several picoseconds or longer).

Fig 1.3 shows different pulse energy levels achieved via different kinds of amplifiers. Using solid-state multi-pass amplifiers, the pulse energy can scale up to the J-level [78,79]. Using fiber amplifiers, the maximum pulse energy achieved so far was in the mJ-level [38], which was realized by applying the combination of CPA and DPA [80].

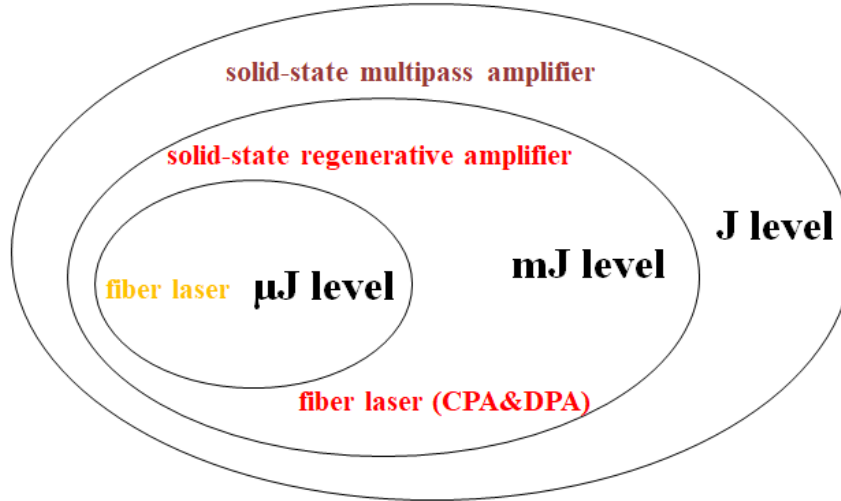


Figure 1. 3: Typical pulse energies achieved with different amplifier technologies.

Microjoule-level ultrafast fiber laser sources can be applied to numerous state-of-the-art ultrafast applications. For example, MHz-level repetition rate ultrafast fiber laser sources with μJ -level pulse energy can significantly increase data acquisition rates and the SNR in strong-field experiments. Both attosecond time-resolved spectroscopy using HHG and space-charge-limited ultrafast photoelectron spectroscopy can benefit from using ultrafast high-repetition-rate source lasers. [81,82] Applying μJ -level ultrafast fiber laser sources, passively CEP-stable, μJ -level MIR laser pulses can be generated by DFG and OPA/OPCPA. Solid-state HHG can greatly benefit from ultrafast high-repetition-rate pump lasers with sub- μJ -level pump pulses, which can significantly increase the photon flux and increase the SNR [83,84]. High-repetition-rate ultrafast fiber sources can be also applied in the ultrafast optical-field-driven electron emission from nanostructures. The applicable pulse energy is limited by the damage threshold of devices making an ultrafast, high-repetition-rate fiber source necessary for detecting the photo-electron current with higher SNR [85].

Figure 1.4 illustrates a method using CPA to realize a μJ -level ultrafast fiber laser system. The pulse duration of seed pulses generated from the fiber oscillator can be stretched by a fiber stretcher to the $\sim\text{ns}$ -level. Sub-mJ-level pulses with hundreds of fs pulse duration energy can be achieved at the output port after propagating through fiber amplifiers and compressors. Further compression can be achieved by using nonlinear

media and further compression to achieve high power single optical cycle pulses for strong-field experiments requiring extremely short pulses.

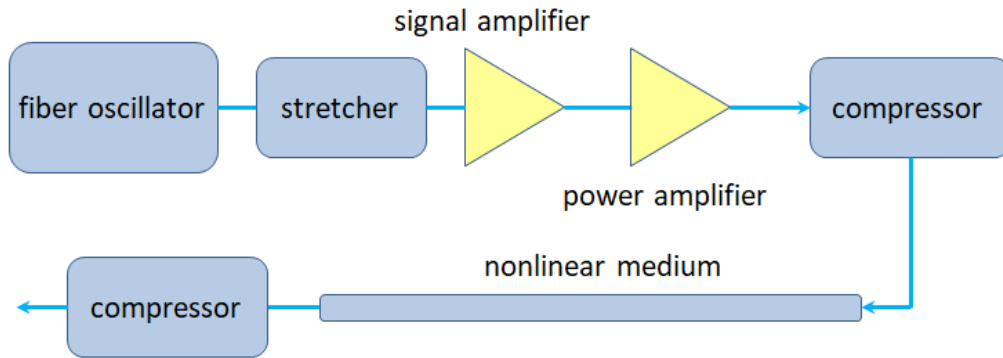


Figure 1. 4: System layout of the ultrafast CPA system.

1.3 HIGH POWER MIR GENERATION

High-power, ultrafast MIR sources [86-88] have been implemented at various repetition rates and average powers for strong-field applications, especially in field-driven electron emission on nanostructures, solid-state HHG and light-matter interaction in graphene. However, the absence of proper gain media for MIR spectral range makes high power ultrafast MIR laser sources have to be derived from the ultrafast NIR laser source via nonlinear frequency conversion processes. The general method is applying second-order nonlinear effects (DFG and OPA/OPCPA) to generate high power ultrafast MIR lasers inside nonlinear crystals [88-91]. Fig 1.5 shows the layout of the second-order nonlinear process. After fulfilling the phase matching condition, idler pulses can be generated during the nonlinear process. The combination of DFG and OPA/OPCPAs has been an excellent choice for generating high-repetition-rate, passively CEP-stable, few-cycle optical pulses.

Utilizing the method of DFG can help to generate broadband ultrafast MIR pulses. A broadband MIR idler pulse with relatively short transform-limited pulse duration can be generated inside thin nonlinear crystals. The crystal length is inversely proportional to the phase matching bandwidth. Therefore, there is a trade-off between the suitable crystal length and the spectral bandwidth of generated idler pulses. Furthermore, generated idler pulses are passively CEP-stable making the DFG effect a well-established architecture for obtaining CEP-stable optical pulses without using electronic feedback to control the CEP.

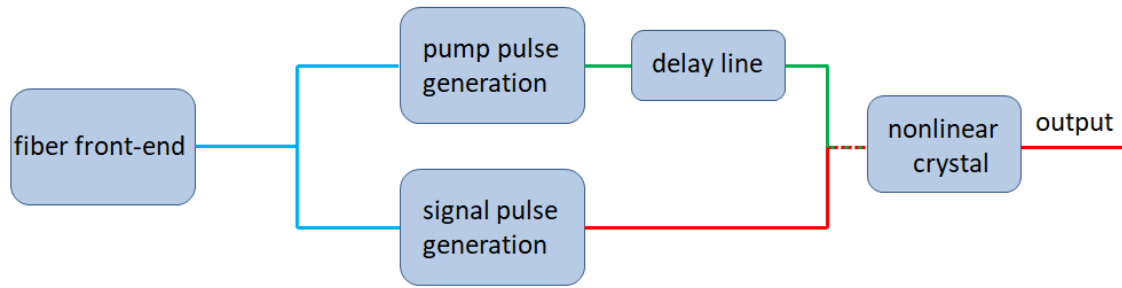


Figure 1. 5: System layout of second order nonlinear process.

Nowadays, OPA/OPCPA is the most promising technology for producing high-power ultrafast sources in the MIR spectral range. In OPA/OPCPA, a quasi-monochromatic, high-energy pump field is coupled to a chirped, low-energy broadband seeding field in a nonlinear crystal. If the seeding pulse is sufficiently stretched, good energy extraction from the pump field can be achieved. Subsequent recompression makes amplified pulses achieve extremely high peak power. The OPA/OPCPA has some important advantages compared with other kinds of laser amplifiers:

- 1) Parametric amplifiers are not limited to narrow wavelength ranges as defined by laser transitions of laser gain media.
- 2) The gain bandwidth is determined by dispersive properties and length of the nonlinear crystal. The parametric amplification process can support gain bandwidth well in excess of those achievable with conventional linear amplifiers allowing the generation of few-optical-cycle light pulses.
- 3) With pulsed pumping, the gain per unit length can be much higher than other amplifiers. OPA/OPCPA has the capability of providing a high gain in a relatively short path length minimizing the B-integral and allowing a compact, tabletop amplifier setup. Since the amplification only occurs when there is pump pulse, the amplified spontaneous emission and the consequent pre-pulse pedestal are reduced.
- 4) A parametric amplifier has no energy storage. It amplifies only while being pumped, which allows for very high intensity contrast between an amplified and any satellite pulses.
- 5) The absence of heat generation (provided that parasitic absorption losses are small) makes OPAs suitable for high-power operation.
- 6) In the case of degenerate parametric amplification, the amplification is phase-sensitive, and quantum excess noise can be avoided.

- 7) The center wavelength is tunable as long as conservation of photon energy and momentum are satisfied.

Thermal loading effects of OPA/OPCPA processes, apart from parasitic absorption, are completely absent reducing spatial aberration of the beams. Above all, these attributes allow OPA/OPCPA to push the limits of high peak power pulse generation over wide wavelength ranges, for which broadband laser amplification has not been developed. Yb-based and Nd-based ultrafast pump lasers can deliver hundreds of watts of average power over designed wavelength ranges promising simultaneous high peak power and high average power from OPA/OPCPA. There are strong interests in developing few-cycle, high-intensity, near-to-mid-infrared OPA/OPCPA as a light source for strong-field applications.

1.4 STRUCTURE OF THE THESIS

Technological advancements towards an ideal high power ultrafast laser source for doing research in strong-field physics are the focus of this thesis. The thesis is organized as follows. In chapter 1, essential background of the basic theory of nonlinear optics, fiber optics and fiber lasers, ultrafast high power fiber lasers and further nonlinear processes such as DFG and OPA/OPCPA for the generation of high-power ultrafast MIR sources are reviewed.

In chapter 2, the design and analysis of a high-power, all-fiber CPA system are presented. We introduce the construction of a home-built 28-MHz repetition rate, stretched-pulse, mode-locked 1- μm oscillator. We also introduce the design of a four-pass all-fiber stretcher and chirped fiber Bragg-grating all-fiber stretcher. The four-pass all-fiber stretcher was applied to stretch seeding pulses for CPA. We also discuss methods of systematic dispersion management and spectral management to ensure pulse compression can be achieved after CPA and grating pair compressor. Finally, the results of using the fiber front-end as the seeding beam for the 1-J amplifier are presented.

In chapter 3, design and analysis of a high power, ultrafast laser system based on the method of circularly polarized pre-chirp managed amplification (CP-PCMA) are presented. We first introduce the home-built 24-MHz mini-CPA system. We then carefully analyze the application of the CP-PCMA to amplify the peak power of circularly

polarized seeding pulses to 1.5 times higher than the critical power for self-focusing effect of linearly polarized seeding pulses. Amplification results using linearly polarized pre-chirp managed amplification (LP-PCMA) and CP-PCMA are compared in this chapter.

In chapter 4, the design and analysis of a high-power ultrafast 2- μm system based on methods of dispersive wave generation, chirped pulse DFG and a dispersion managed OPA are presented. First, we introduce the use of dispersive wave generation inside a high nonlinear fiber (HNF) to generate the positively chirped dispersive wave as the pump beam for the chirped-pulse DFG stage. Second, we introduce our work using a thin BBO crystal as a nonlinear crystal for the chirped-pulse DFG stage to generate broadband, passively CEP-stable 2- μm idler pulses. Third, we introduced our design and experimental results of our pre amplifier and power amplifier based on the theory of parametric amplification. Finally, we discuss and analyze our dispersion managed 2- μm system. We discuss the construction and use of an interferometric auto-correlator to measure the pulse duration.

In chapter 5, the conclusion of the thesis and future capabilities of these laser systems are presented. We introduce methods to scale up the power level of the two 1- μm all-fiber systems discussed in this thesis. We also discuss further applications of our few-cycle, high power, 2- μm OPA source.

CHAPTER 2: HIGH-POWER ALL-FIBER 1- μm CPA LASER SYSTEMS

The high repetition rate, high power, ultrafast 1- μm laser systems have experienced rapid technological advancements as an enabling technology for strong-field experiments, medical use and industrial applications [92-104]. Compared with solid state-lasers, fiber lasers can be more stable and more compact working with much better beam profile. Therefore, there are stronger demands for high power 1- μm fiber laser systems ensuring the long-term stability and perfect beam profile for further applications. In applications of precise measurements, by locking the repetition rate f_R and carrier-envelope offset frequency f_{ceo} with the atomic reference, low noise 1 μm fiber laser combs can be used as the reference for astronomical telescopes, and timing measurements [92,93]. The high power, high repetition rate, 1 μm ultra-fast laser sources can also be used to drive high harmonic generation in the vacuum chamber to generate UV/EUV lasers for example research in attosecond physics. During these high field experimental applications, high-repetition-rate 1- μm laser sources can significantly improve experimental parameters with super high photon fluxes, such as improving the signal to noise ratio in EUV-imaging, and avoid space charge effects in photoelectron spectroscopy [94-96]. For applications like OPA/OPCPA, the compact stable 1 μm fiber lasers can be used as an all-fiber powerful front-end for MIR wavelength generation [101]. High average power ultrafast 1 μm fiber lasers are also used in manufacturing by laser micromachining [102,103]. In this chapter, we will introduce the home-built >55-

W, 250-fs, 1-MHz, 1- μm all-fiber laser front-end of the CPA, the dispersion management and the spectral management. Using dispersion compensating fiber, we built a 4-pass all-fiber stretcher to stretch the seeding pulses and manage the dispersion together with the grating pair compressor. The spectral management optimizes the pulse compression in this system to achieve clean amplified pulses.

2.1 METHODS FOR FIBER AMPLIFICATION

In order to build high power ultrafast 1- μm fiber lasers, there are two well-established methods to amplify the average power of seed pulses to even above 1 kW, which are the CPA [77] and divided pulse amplification (DPA) [80]. For general fiber amplifiers without CPA or DPA, amplified seeding pulses can accumulate strong nonlinear effects during the propagation in fiber. The generated nonlinear effects during the amplification process can result in uncompensated nonlinear phase making it difficult to compress the amplified pulse to near its transform limited. The most efficient way to avoid the nonlinear effects during the amplification process is to inhibit the pulse peak power by stretching the pulse width before amplification. The general schematic of a CPA is shown in Figure 2.1 (a). In CPA, we use the stretcher to stretch seeding pulses to decrease the pulse peak power. The optical paths for different spectral content of seeding pulses are different by managing the dispersion parameters of the stretcher. This difference leads to the walk off of different spectral content in a pulse. Hence, it stretches the pulse duration during the propagation inside the stretcher. After the stretcher, the pulse duration is long enough to inhibit the peak power and prevent accumulating nonlinear phase during the amplification process. Shown in Figure 2.1 (b), the DPA uses the optical divider to divide seeding pulses to even replicas before sending them into amplifiers. In this way, the peak power of amplified pulses in the amplifier is decreased. The peak power for every amplified replica will be divided by the number of the replicas multiplied by the original amplified pulse peak power after dividing the seeding pulses into replicas. These amplified replicas can be combined by the optical combiner to become one replica before the compression stage. Therefore, further compression can be done in the grating pair compressor.

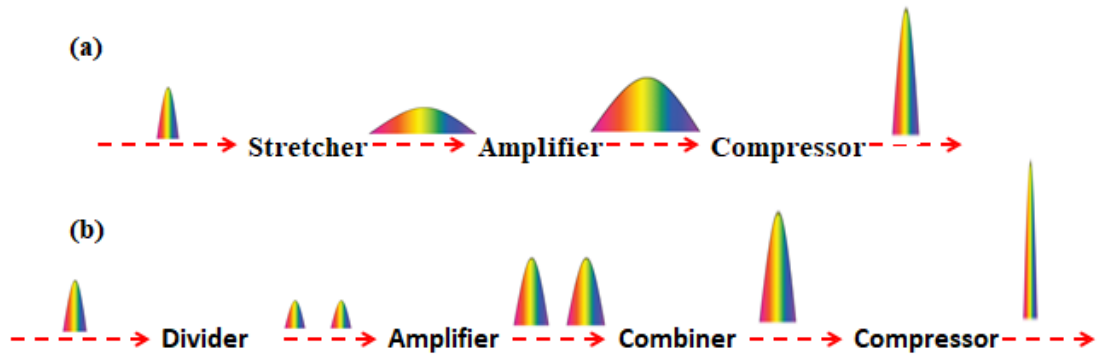


Figure 2. 1: Schematic constructions of the CPA (a) and DPA (b).

Stretcher is used stretch the pulse. Amplifier is used to amplify the average power of pulses. Compressor is used to compensate the dispersion and compress the pulse. Divider is used to split the pulse in temporal domain. Combiner is used to combine the splitted pulses.

There are also other methods to amplify seed pulses besides using CPA and DPA. The polarization of the seed pulses is linear for general polarization maintaining (PM) amplification. Using circularly polarized seeding pulses for PM amplification can lead to polarization dispersion. This is caused by the group velocity difference between fast optical axis and slow optical axis in the PM fiber. Using the circular polarization, the non-PM gain fiber should be isolated from environmental influences and bending stresses to avoid polarization rotation during the propagation. This is obviously impossible for general non-PM fiber. The newly invented rod-type rare-earth-doped PCF module makes it possible to apply the circular polarization amplification in the fiber amplifier. The polarization direction of the seed beam won't be changed by environmental influences and external tensions after keeping the straight PCF inside a well-sealed aluminium module.

The schematic of the circularly polarized pulse amplification (CPPA) is shown in Figure 2.2(a). The CPPA can amplify the peak power of the circularly polarized seeding pulses 1.5 times higher than the linearly polarized seed pulse [104]. The nonlinear coefficient of linearly polarized pulses is 1.5 times higher than the coefficient for circularly polarized pulses (equation 2.1.1 and 2.1.2). This means that the average power of circularly polarized pulses can be amplified 1.5 times higher than linearly polarized pulses accumulating same nonlinear phase during the amplification process. The general limitation for building fiber amplifiers is self-focusing. It can lead to ionization and plasma generation to damage the gain media. Applying the method of CPPA, the critical power of the threshold for self-focusing of circularly polarized seed

pulses is 1.5 times higher than for linearly polarized pulses. Therefore, we can avoid damage in fiber amplifiers when we try to amplify the average power of seed pulses to higher level. For light-matter interaction experiments, this method can help to get 0.5 times higher photon flux without doing significant changes to the experimental setup. For nonlinear frequency conversion inside short fibers, this method makes weak signal generation and amplification much easier to realize.

$$\left\{ \begin{array}{l} n_{2,L} = \frac{3 \operatorname{Re}(\chi_{xxxx}^{(3)})}{4 \varepsilon_0 c n_0^2} \\ n_{2,C} = \frac{2 \operatorname{Re}(\chi_{xxxx}^{(3)})}{4 \varepsilon_0 c n_0^2} \end{array} \right. \quad (2.1.1)$$

$$\left\{ \begin{array}{l} n_{2,L} = \frac{3 \operatorname{Re}(\chi_{xxxx}^{(3)})}{4 \varepsilon_0 c n_0^2} \\ n_{2,C} = \frac{2 \operatorname{Re}(\chi_{xxxx}^{(3)})}{4 \varepsilon_0 c n_0^2} \end{array} \right. \quad (2.1.2)$$

The schematic of pre-chirped pulse amplification (PCMA) is shown in Figure 2.2 (b). The PCMA amplifies seed pulses based on nonlinear fiber amplification [98]. It is a combination of the pre-chirper, PM fiber amplifier and compressor. The pre-chirped seed pulses are amplified during the nonlinear amplification process including nonlinear refractive index effects like SPM. The nonlinear phase generated by SPM can broaden the spectrum and mitigate high-order dispersion effects in the amplified seed pulses. By carefully optimizing the pre-chirper, few-cycle pulses can be generated right after the compressor without any further nonlinear compression necessary. The PCMA can also work together with CPPA to achieve higher average output power with few-cycle pulse duration.

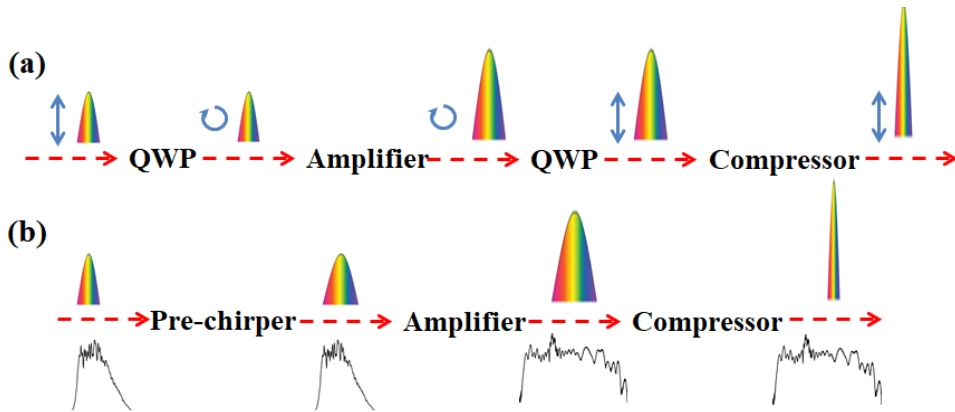


Figure 2. 2: Schematic constructions of the CPPA (a) and PCMA (b).
Pre-chirper is used to pre-chirped the pulses before amplifier. QWP: quarter wave-plate.

2.2 HIGH POWER 1 μM ALL-FIBER FRONT END BASED ON CPA

The method of CPA can help to avoid detrimental nonlinear effects inside the fiber laser systems to achieve high repetition rate and high peak power beyond above 100

MW. The general method to stretch seed pulses in the high power CPA system is using a free space stretcher. However, the free space stretcher can introduce long term mechanical drifts to the system leading to long term instability. Dispersion managed all-fiber stretchers become possible by applying dispersion compensation fiber (DCF) or chirped fiber Bragg gratings (CFBG). These kinds of all-fiber stretchers can be used in an all-fiber laser system with perfect long term stability. Amplified pulses with Gaussian profile can have over hundreds of megawatts peak power with femtosecond-level pulse duration after compression.

The system layout of the home-made 1- μm , 1-MHz laser system is shown in Figure 2.3. The temperature of the whole system was controlled by the water cooling system keeping the system temperature at 25 °C. The all-fiber stretcher was built to stretch the pulse duration of the seed pulses from 7 ps to 800 ps. The repetition rate of the seed pulses was decreased to 1 MHz by an AOM. The 1-MHz 800-ps pulses were finally compressed to 250 fs after being amplified to over 55 W by three stages of fiber amplifiers.

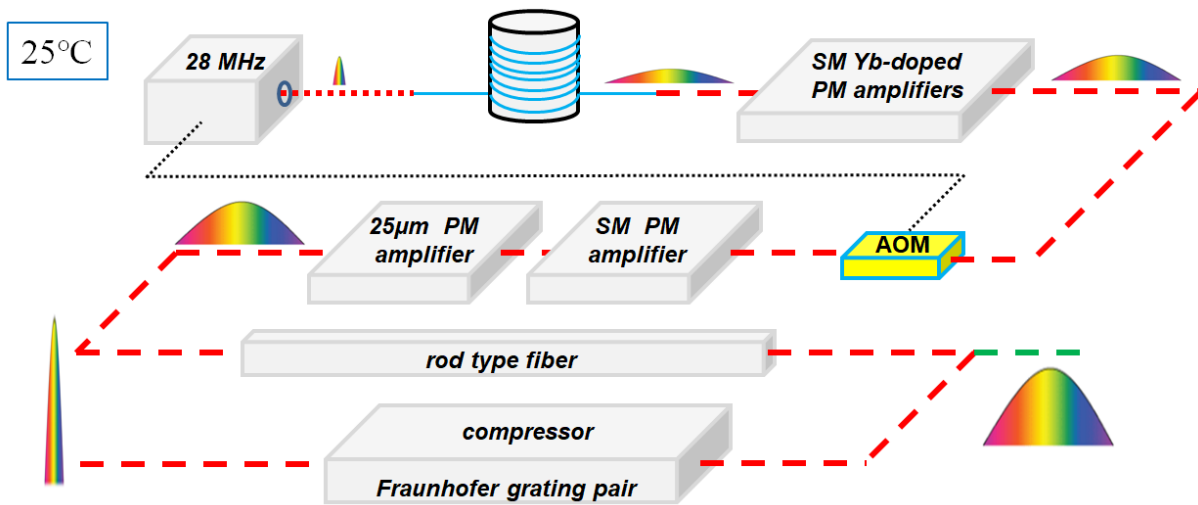


Figure 2. 3: System layout of the home-built 1 MHz 1 μm CPA system.

SM: single-mode; PM: polarization maintaining; AOM: acoustic optical modulator. Red dashed line means the 1 μm laser. Green dashed line means the 976 nm pump laser.

2.2.1 28 MHz HOME-MADE STRETCHED PULSE MODE-LOCKED FIBER OSCILLATOR

The passive mode-locking status allowing the generation of ultrafast pulses can be realized by using the saturable absorber as we mentioned in chapter 1. Based on the Kerr effect, there are three kinds of saturable absorbers that can be used to realize passive mode-locking status, SESAM, nonlinear loop mirror and the construction of the

nonlinear polarization evolution (NPE). The NPE mode-locking scheme is the best choice for our system considering the good self-starting status and short pulse operation. The polarization direction rotates inside the non-PM fiber inside the NPE mode locking cavity. This polarization rotation generates together with the fiber polarization controllers and polarizers as a fast saturable absorber realizing passive mode locking. The general types of NPE mode-locked fiber oscillators can be roughly categorized into three groups: (a) soliton mode-locked fiber oscillators, (b) stretched pulse mode-locked fiber oscillators and (c) all-normal-dispersion fiber oscillators [105].

- (a) A fundamental soliton can be generated in the negative dispersion regime by the interplay between SPM and dispersion. Since the soliton plays a key role in the self-amplitude modulation process, there are constraints for the peak power, pulse duration, and pulse energy to keep the fundamental soliton stable. The peak power of the soliton should not exceed the value required to reach the maximum of the nonlinear transmission curve.
- (b) The fiber cavity is constructed out of separate positive and negative dispersion sections. The net cavity dispersion can be zero or slightly positive. Dispersion and SPM still play a key role, but do not involve fundamental soliton propagation. Therefore, the laser output can scale to shorts pulses with broader spectra and higher energies.
- (c) The fiber oscillator consists only of components with normal GVD, which means no dispersion management is provided. By inserting a spectral filter and increasing the nonlinear phase shift accumulated by the pulse, self-amplitude modulation via spectral filtering is enhanced, which allows NPE to scale to higher pulse energies.

Here, we aimed at building a 1- μm oscillator to generate a mode-locked laser with spectra covering from 1030 nm to 1045 nm. The stretched pulse mode-locked fiber oscillator can generate an output spectrum covering 1020 nm to 1060 nm by adjusting the dispersion delay line (transmission grating pair) inside the cavity. The schematic layout of the home-built 28-MHz 1- μm oscillator and the output spectrum are shown in Figure 2.4. The isolator consists of two polarization beam splitters (PBS), a half wave-plate and a Faraday rotator (FR). The FR was used to enforce unidirectional operation acted as a polarizer. PBSs before and after the isolator were used to enforce bias the ring

for positive self-amplitude modulation (transmission through polarizer increase with increasing intensity). The transmission grating pair used as the dispersion delay line to control the net cavity dispersion to final control the bandwidth of the output spectrum. About 40 cm long Ytterbium doped single-mode gain fiber (Yb-401) was used as the gain material inside the ring cavity.

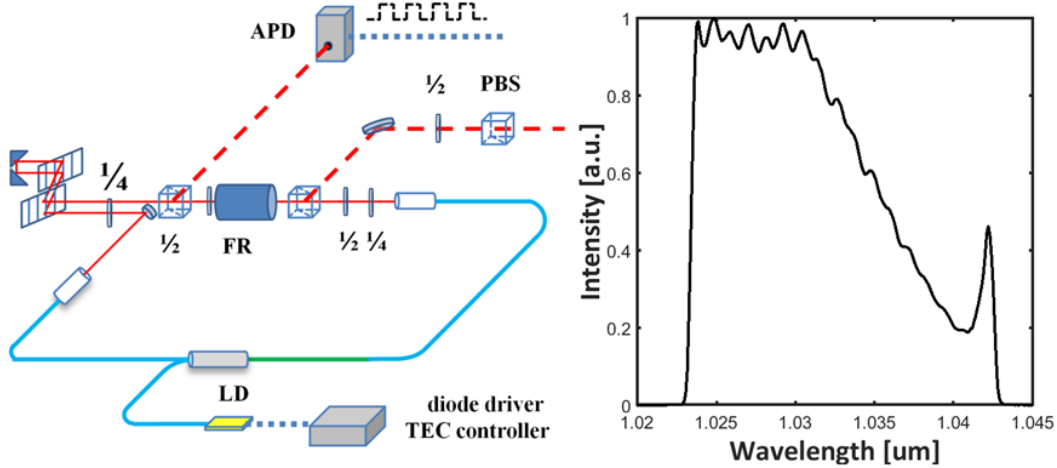


Figure 2. 4: Schematic layout of the home-built 28 MHz oscillator and the corresponding output spectrum. FR: faraday rotator; LD: laser diode; APD: avalanche photo diode; $\frac{1}{2}$: half wave-plate; $\frac{1}{4}$ quarter wave-plate; PBS: polarization beam splitter.

Table 2.1: Parameters of the 28 MHz Oscillator

Name	Value	Unit
Pump Power	90	mW
Pump Wavelength	976	Nm
Diode Working Temperature	20	$^{\circ}\text{C}$
Center Wavelength	1033	Nm
Output Power	5	mW
Grating Pair Separation	23	mm
Repetition Rate	28	MHz
Output Pulse Duration	7	Ps

The parameters of this 28-MHz 1- μm home-built oscillator are shown in Table 2.1. The final output power was attenuated to 1 mW by the combination of a half wave-plate and a PBS to minimize the generated nonlinear phase in the initial part of the fiber stretcher. The final output spectrum is shown in the right picture in Figure 2.4. The bandwidth of the final output spectrum covered 20 nm of wavelength ranging from 1023 nm to 1043nm. The separation of the grating pair inside the cavity was set to be 23 mm to realize the stretched pulse mode-locking scheme and generate a broadband

spectrum covering from 1030 nm to 1040 nm. The leaking output beam from the ring cavity was used to be the signal laser of the APD to generate the 28 MHz electronic rectangle signal for further repetition rate reduction module.

2.2.2 HOME-MADE ALL FIBER STRETCHER FOR BROADBAND FIBER AMPLIFICATION

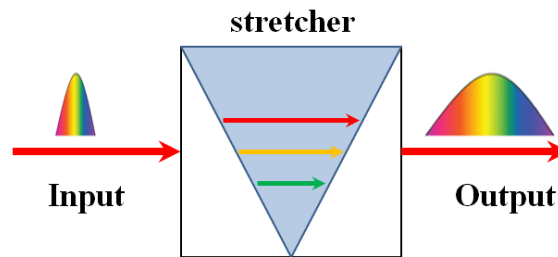


Figure 2. 5: Layout of the general stretcher.

The stretcher stretches pulses by adding dispersion to input pulses. As is shown in Figure 2.5, the stretcher provides different optical path for different optical wavelength stretching the pulse to inhibit nonlinear effects in following cascaded fiber amplifiers. There are two general methods for building the stretcher, free space stretcher and fiber stretcher. Compared with the free-space stretcher, the all-fiber stretcher can improve the long-term systematic stability, make the construction compact and keep the fundamental mode profile of the stretched pulses. Therefore, the all-fiber stretcher was a choice of the stretcher of this fiber CPA system.

The systematic dispersion management needs to be done to make sure the stretched pulses can be compressed by the compressor before building the stretcher. The general way to build the all-fiber stretcher is using the DCF or CFBG to be the dispersion management element. The dispersion curve of the CFBG can be manufactured to be conjugate with the dispersion curve of the grating pair compressor. The DCF with positive GVD and negative TOD at 1 μm is also a proper dispersion management element to make the dispersion curve of the fiber laser system conjugate to the final compressor. However, the CFBG has reflection bandwidth limitations making the stretcher built with CFBG only suit for narrow spectral bandwidth amplification. Therefore, the CFBG provides an efficient and compact way to stretch the seed pulses for narrow-band CPA,

especially for the narrow-band solid-state amplifiers. The combination of the DCF and normal signal mode fiber can become a proper stretcher for broadband amplification.

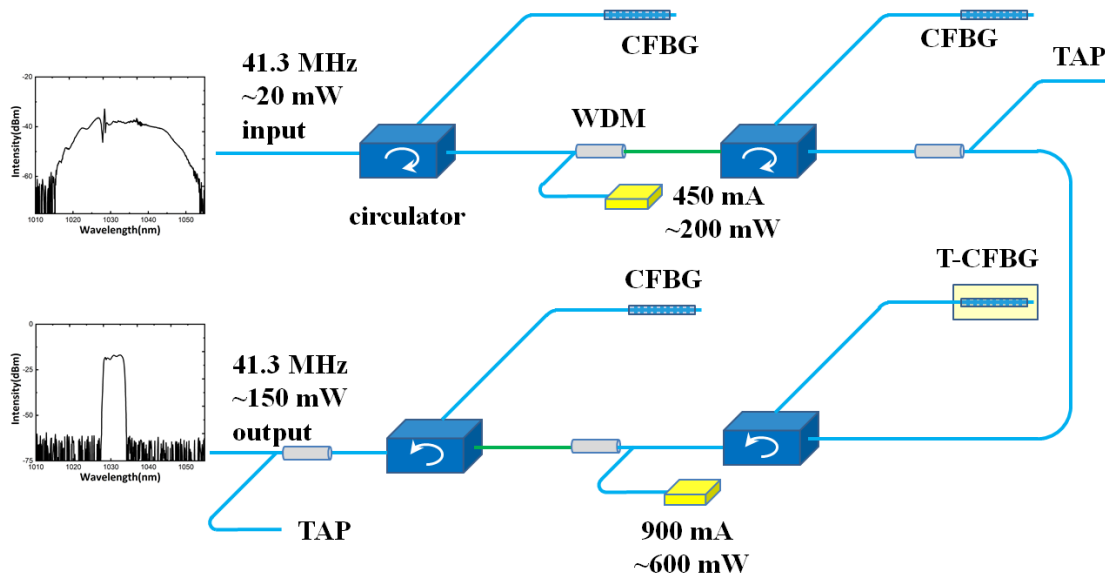


Figure 2. 6: Schematic construction of the 5-nm four-CFBG fiber stretcher.

T-CFBG: temperature controlled CFBG, TPSR. Inset picture shows the pulse profile taken from the sampling oscilloscope.

The schematic construction our four-CFBG fiber stretcher is shown in Figure 2.6. We built the stretcher to stretch 1- μm seed pulses at 41.3 MHz repetition rate. The pulse duration of the seed pulse was stretched from few picoseconds to ≈ 3.6 ns shown in Figure 2.7. It was measured by the 3.5 GHz oscilloscope using a >12.5 GHz bandwidth photo detector. Therefore, the stretched pulses were used as the seed pulses for the narrow-band regenerative amplification with the kHz Yb:KYW dual-crystal regenerative amplifier [106] and further amplification with cryogenic multi-pass solid state amplifiers [107,108], which will be introduced in this chapter.

Considering the insertion loss of the CFBGs, there were two polarization maintaining single-mode fiber amplifiers inside the four-CFBG fiber stretchers to compensate the 24-dB insertion loss of the whole CFBG stretcher system and amplify the average power of the output stretched seed beam high enough for seeding the Yb:KYW dual-crystal regenerative amplifier. There was a temperature controlled dispersion tunable CFBG inside the stretcher, which can be used to finely modify the dispersion management and stabilize the final output pulse duration of the whole four-CFBG fiber stretcher by tuning the temperature of this dispersion tunable CFBG. The 99:1 coupler at the output port was used to split about 1% stretched seed pulses monitoring the working status of the stretcher and triggering the modulator circuits for the Yb:KYW dual-crystal regenerative

amplifier. The pulse energy of the 3.6-ns output pulse was amplified to about 3.66 nJ at 41.3 MHz repetition rate.

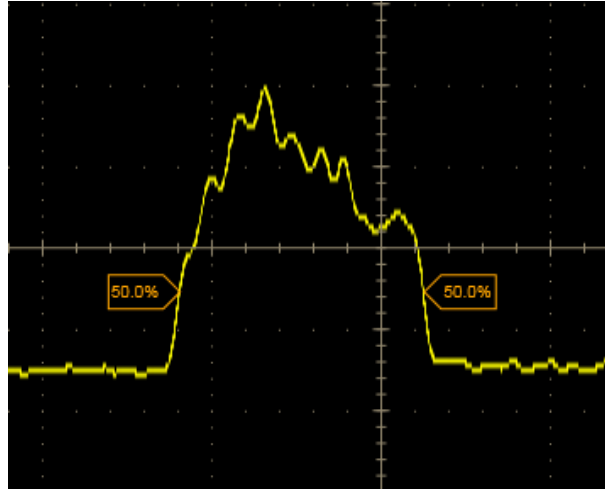


Figure 2. 7: Pulse profile of the stretched pulse with 3.6 ns pulse width.

Shown in Table 2.2, the $\geq 80\%$ reflection bandwidth of the CFBG is 6 nm which limits the bandwidth of the output spectrum to be < 6 nm. These CFBGs have a dispersion curve conjugate with the grating pair compressor to stretch seed pulses by adding positive group delay dispersion (GDD) and negative TOD. Therefore, the four-CFBG fiber stretchers can work perfectly at 1030 nm together with the narrow-band amplifiers and the grating compressor achieving near transform-limited pulses. Figure 2.8 shows the picture of the 41.3-MHz oscillator and the four-CFBG fiber stretchers. The system was sealed with optical enclosures to get rid of environmental influences.

Table 2.2: Parameters of the CFBG

Name	Number	Units
Center Wavelength @ 3dB	1030 ± 0.5	nm
Reflection Bandwidth @ 3dB	6.0 ± 0.6	nm
Min. Reflectivity over 80% of FWHM	≥ 80	%
D2	-174.7218	ps/nm
D3	-4.1457	ps/nm ²
D4	-0.10792	ps/nm ³
D5	-0.0034915	ps/nm ⁴

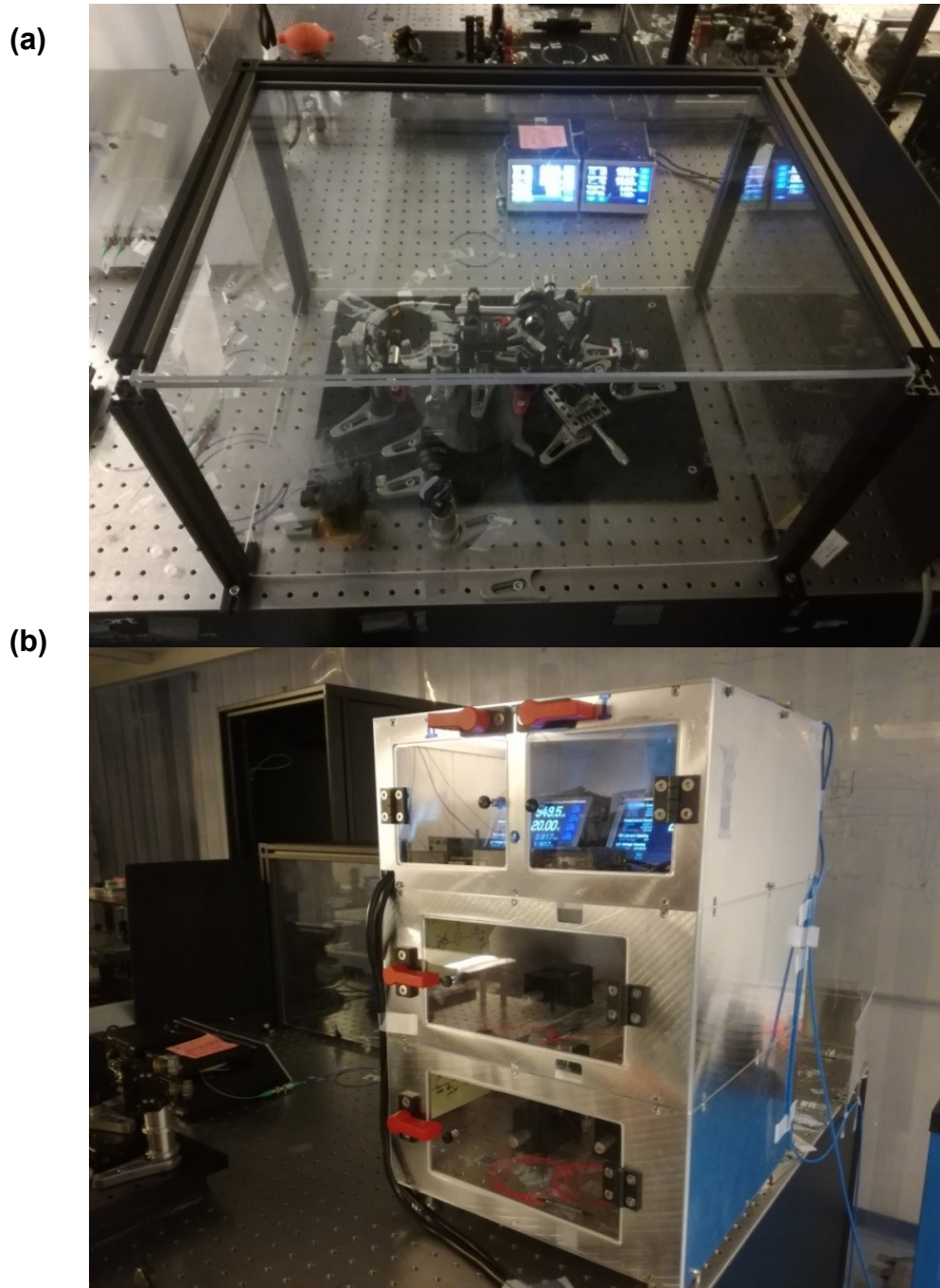
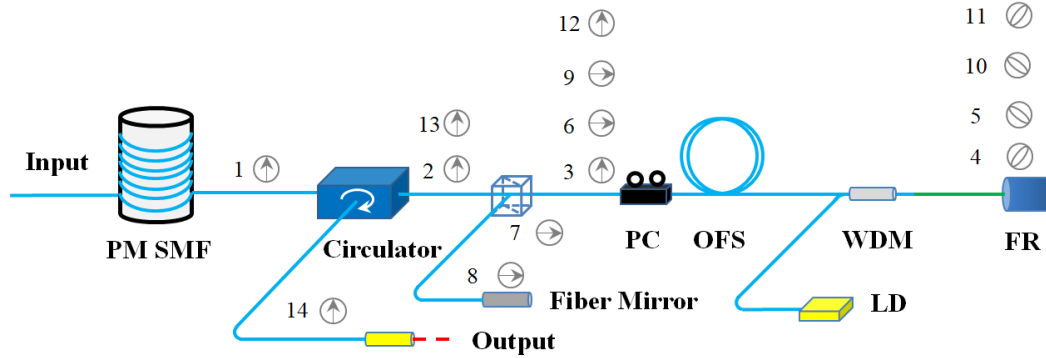


Figure 2. 8: (a) Picture of the 41.3-MHz oscillator, (b) picture of the CFBG stretcher.

Apparently, because of the reflection bandwidth limitations, the all-fiber CFBGs stretcher cannot be used as the stretcher for further broadband fiber-based amplification. Therefore, DCFs can be used to be the dispersion management element of the fiber stretcher for broadband amplification. Based on the systematic dispersion management, the polarization maintaining single-mode fiber (PMSMF) and negative TOD stretcher fiber (OFS FemtoComp) were chosen to build the all-fiber stretcher to stretch seed pulses from 7 ps to 800 ps for broadband fiber amplification.

Table 2.3: Dispersion parameters of the OFS stretcher fiber and PMSMF

Dispersion parameters at 1030nm	OFS	PMSMF
β_2 (ps^2/m)	0.12	0.023
β_3 (ps^3/m)	-9.6×10^{-4}	4.6×10^{-5}

**Figure 2. 9: Schematic layout of the all-fiber 4-pass stretcher.**

PMSMF: polarization maintaining single-mode fiber; FR: faraday rotator; LD: laser diode; PC: polarization controller; WDM: wavelength division multiplexer. The green line represents the Yb-doped gain fiber

The dispersion parameters of the PMSMF and OFS stretcher fiber are shown in Table 2.3. The TOD of the OFS stretcher fiber at 1 μm is negative. The TOD of the PMSMF and grating compressor at 1 μm is positive. The absolute value of the TOD of the OFS stretcher fiber is 20 times higher than the PMSMF. Therefore, based on carefully systematic dispersion design, the OFS stretcher fiber can be used to compensate the TOD of the high power, high-repetition-rate, 1- μm system. The grating pair compressor with negative GDD can be used to compensate the positive GDD of the 1- μm system. The designed 4-pass stretcher was built to compensate the TOD completely and nearly compensate the fourth order dispersion (FOD) together with the grating pair compressor at the end of the laser system.

The schematic construction of the all-fiber 4-pass stretcher is shown in Figure 2.9. The input power to the stretcher was minimized by an optical attenuator to ~ 1 mW to inhibit nonlinear effects in the 150 m long PMSMF. An Yb-doped single-mode fiber amplifier was spliced into the stretcher to compensate the 10-dB insertion loss of the circulator and OFS stretcher fiber while slowly boosting the seed power as the pulse is chirped to avoid nonlinear phase accumulation in the stretcher fiber. The B-integral of

this configuration for the stretcher is estimated to be roughly 1 radian. The polarization evolution is also illustrated in Figure 2.9 with arrows and ellipses. The fiber polarization controller was used to control the polarization of the pulses in the stretcher to make sure that the seed pulse can propagate through the OFS fiber 4 times with the help of the combination of fiber PBS and fiber mirror. The fiber polarization controller can also improve the polarization extinction ratio of the output pulses to about 20 dB to get rid of the potential polarization dispersion. With the combination of the fiber PBS, fiber polarization controller and the fiber faraday rotator, the 1- μm mode-locked laser propagated through the OFS stretcher fiber 4 times to stretch the pulses to 800 ps. The output power of the stretched pulses was set to be 1 mW, which is high enough to suppress the amplified spontaneous emission (ASE) in the subsequent amplifiers. The pulse profile of the stretched 800 ps pulse was measured by the sampling oscilloscope and can be found in Figure 2.10.

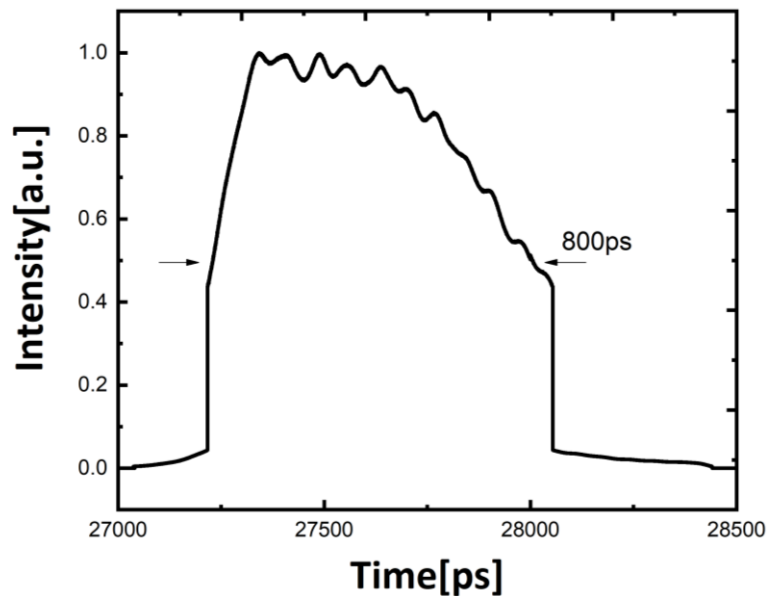


Figure 2. 10: Pulse profile of the stretched pulses after the stretcher taken from sampling oscilloscope.

2.2.3 REPETITION RATE REDUCTON MODULE USING AN AOM

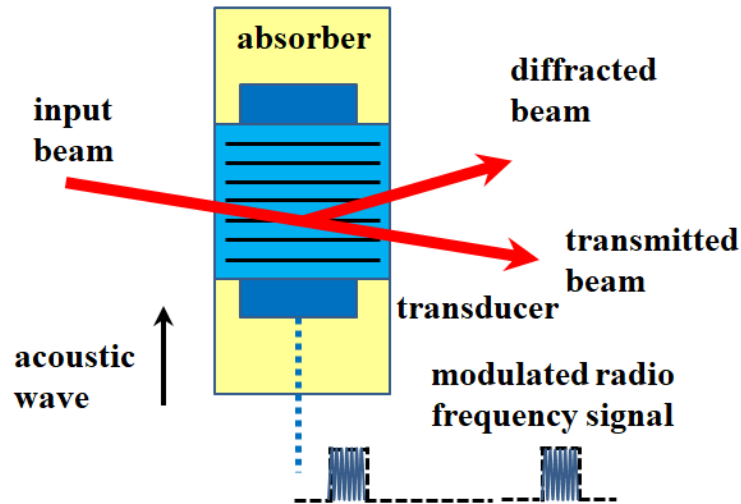


Figure 2. 11: Layout of an acousto-optic modulator used as optical pulse picker.

As the acousto-optic interaction or diffraction of light by acoustic waves, acousto-optic effect was first predicted by Brillouin in 1921 and experimentally revealed by Lucas, Biquard and Debye, Sears in 1932. Based on the acousto-optic effect, the AOM has an enormous impact on ultrafast nonlinear optics. The AOM can be used for controlling the power, frequency or spatial direction of lasers with the modulated electrical drive signal. It is based on the acousto-optic effect, which is the modification of the refractive index by the pressure waved of an acoustic wave. The layout of the AOM used as the pulse picker is shown in Figure 2.11. By injecting the modulated radio frequency signal into the AOM, the generated modulated sound wave inside the AOM can turn the acousto-optic crystal to be a modulated diffraction grating. The acousto-optic crystal can only work as a diffraction grating when the modulation signal is on. After sending the signal beam to the AOM, the acousto-optic crystal and the modulated acoustic wave make the AOM become an optical pulse picker, which can be used to decrease the repetition rate of the input mode-locking laser. Therefore, repetition rate tunable laser sources can be realized by using an AOM. The extinction ratio between picked pulses and residual satellite pulses are based on the raise time of the AOM and the repetition rate of input pulses. Therefore, the repetition rate of seed pulses should match with the raise time of the AOM to achieve high extinction ratios at the output of the AOM.

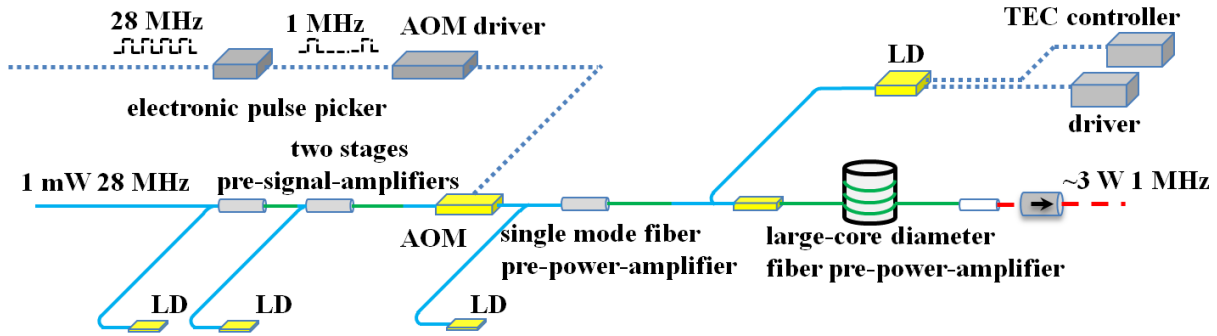


Figure 2. 12: Schematic layout of the repetition rate reduction module.
AOM: acousto-optic modulator; LD: laser diode.

The schematic construction of the repetition rate reduction module is shown in Figure 2.12. The input 28-MHz, 800-ps, 1-mW, 1- μm beam was amplified by two stages PMSMF pre-signal-amplifiers to about 100 mW before the AOM. For each stage of pre-signal-amplifiers, the PMSMF amplifier consists of a polarization maintaining wavelength division multiplexer (PMWDM), 976-nm pump laser, and 0.5-m high Yb-doped gain fiber (PM YB401). The electronic pulse picker circuits were used to reduce the repetition rate of the electronic signal from the APD shown in Figure 2.4 from 28 MHz to 1 MHz. This 1 MHz electronic signal was used to be the carrier envelope modulation signal to modulate the generated 200 MHz radio frequency signal from the AOM driver to make the AOM become an optical pulse picker. The insertion loss of the fiber AOM was about 4 dB, so that the output power of the 1 MHz pulse train was about 1 mW. The raise time of the AOM was <5 ns. The peak power ratio of the main pulse and satellite pulse was >20 dB. The PMSMF pre-power-amplifier consisted of the PMWDM, 976-nm single-mode laser diode and 0.75 m PM-YB-501 fiber. The PM large-core diameter fiber pre-power-amplifier consisted of the PM large-core diameter fiber combiner (25- μm core-diameter), 20 W multi-mode 976-nm pump diode, and 4 m Nufern PLMA-YDF-25/250 gain fiber. The generated high order modes inside the 25- μm core-diameter fiber were inhibited by tight coiling the fiber on the 8-cm diameter aluminum column. After these two pre-power-amplification stages, the 1-MHz, 800-ps, 1- μm laser were amplified to about 3 W at fundamental mode.

2.2.4 DISPERSION MANAGEMENT, SPECTRAL MANAGEMENT AND COMPRESSION

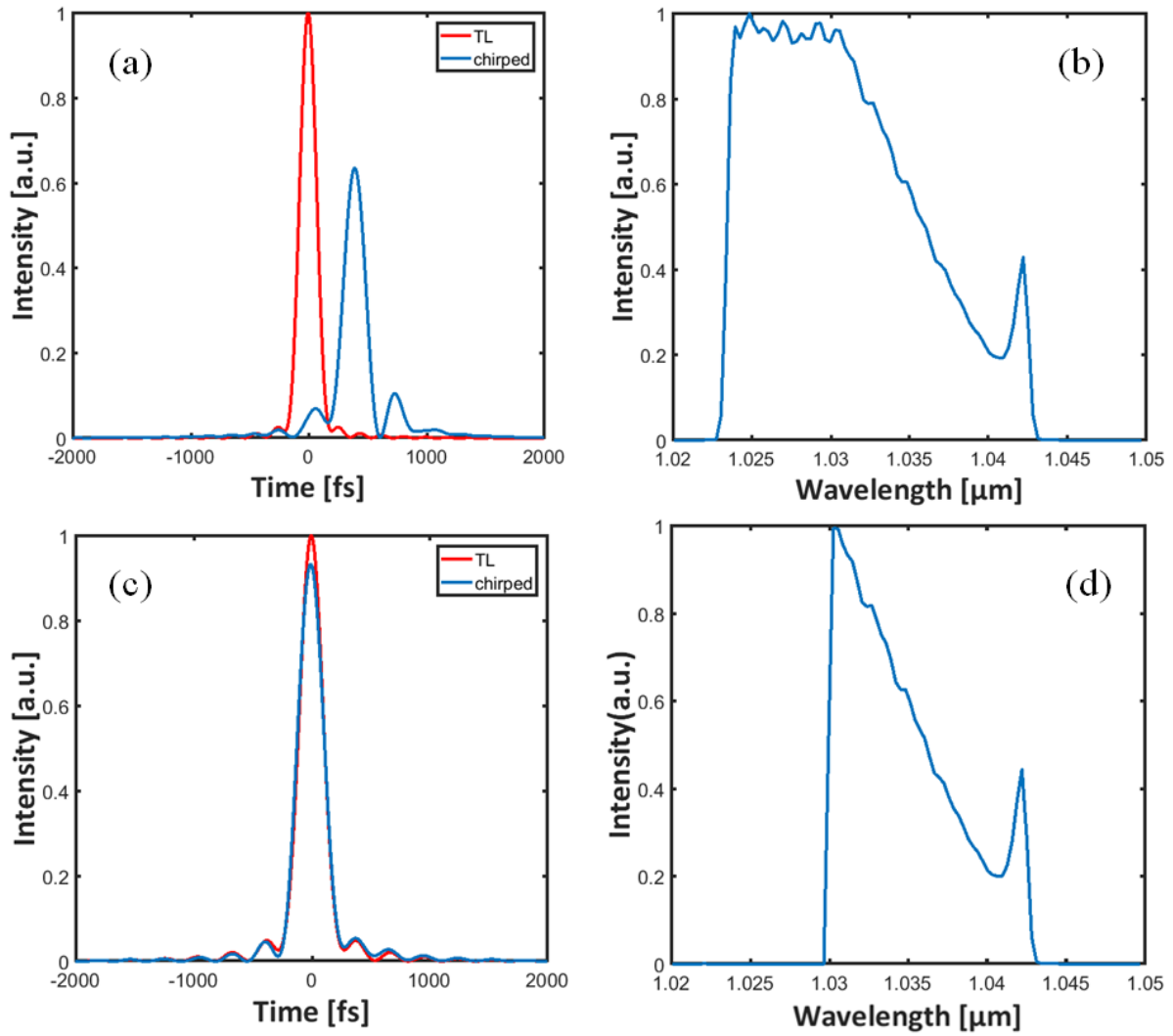


Figure 2. 13: Simulation results for compression and its effect on spectral content.

Numerical simulation of the spectral filtering effect on pulse compression in the fiber amplifier. The temporal profile of the compressed pulse (“chirped pulse”) in blue and corresponding transform-limited (TL) pulse in red (a), and the spectrum of the seed laser (b); the temporal profile of the compressed pulse (“chirped pulse”) in blue and corresponding TL pulse in red (c), and the spectrum after using a sharp long-pass filter at 1030 nm.

Since the gain bandwidth of the rod-type gain fiber of the final amplifier is in the range of 1030-1040 nm and the effective gain bandwidth of the PM double-cladding gain fiber is also above 1030 nm, the grating compressor is optimized at this wavelength range and therefore the spectral contents below 1030 nm are more susceptible to high-order spectral phase distortion. Based on the experimental parameters, we did the numerical simulation to further study the influence of the spectral content on compression. The calculation result is shown in Figure 2.13. The best simulated compression results by compensating the dispersion via the reflection grating compressor for the unfiltered seed spectrum shown in Figure 2.13(a) and Figure 2.13(b)

indicate that there were still significant pedestals after being compressed by the reflection grating pair. The simulated peak power of the chirped pulse is only about 66% of the calculated transform-limited pulse. The spectral wavelength range shorter than 1030nm is out of the gain bandwidth, which can generate uncompensated phase during the amplification process. Also, the residual fourth order dispersion for the shorter wavelength range is hard to be perfectly compensated by the grating pair compressor. Therefore, removing the spectral content below 1030 nm can help us to get better compression results. Furthermore, using the spectral filter to shape the spectrum in a parabolic way is helpful to increase the peak power by inhibiting the intensity of the pedestals [109-111].

By using a sharp spectral filter to get rid of the spectral content in the wavelength range shorter than 1030nm, the simulation results in Figure 2.13(c) show that the compressed pulse can perfectly match with the calculated transform-limited pulse based on spectral filtering. This result indicates that the chirped pulse can be compressed with the grating pair compressor after doing the dispersion management and spectral content filtering. The peak power of the compressed chirped pulse is about 93% of the transform-limited pulse. However, inserting the free space long pass filter inside the setup to get rid of the shorter wavelength spectral content can introduce long term spectral change. The long term change was caused by the long term drift of the filter rotation stage. The long term spectral change can lead to the slow change in pulse width after compression and instability of the system. Based on the design, the gain bandwidth of gain fibers and coatings of the elements inside the setup were carefully chosen to become a passively effective filter to inhibit a wavelength range shorter than 1030 nm to help to optimize the compression results. Figure 2.16(a) shows the spectra of the oscillator and the final output of the amplified 1- μm source. The wavelength range shorter than 1030 nm was well inhibited by the effective filter.

2.2.5 DESIGN OF THE FIBER POWER AMPLIFIER AND COMPRESSOR

The development of rod-type fiber amplifier makes it possible to amplify the average power of mode-locking fiber lasers to the hundreds Watt level which was only previously available in solid state configurations. We used the 85- μm core diameter aeroGAIN-ROD module (NKT Photonics) to be the rod-type fiber amplifier to amplify the

seed pulses. The parameters of this module are shown in Table 2.4. By well designing the structure of this kind of rod-type photonics crystal fiber, the output beam can keep the fundamental mode after the mode competition during the propagation inside the fiber. The Kerr self-cleaning effect in multimode fiber when the average power of the ultrafast pulses is amplified to a high level also helps to keep the fundamental mode of the beam. Figure 2.14 shows the output beam profile with a nice fundamental mode right after the rod-type fiber amplifier.

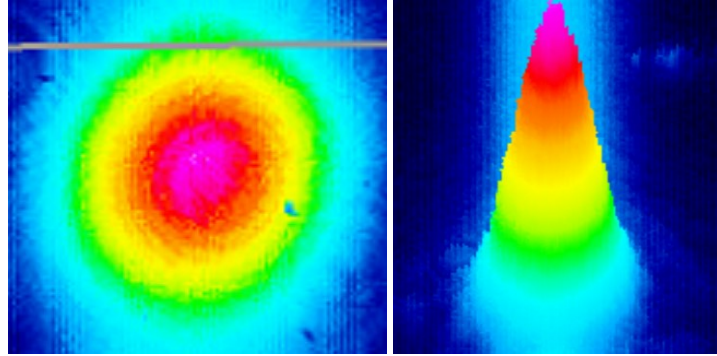


Figure 2. 14: Output beam profile after rod-type fiber amplifier.

Table 2.4: Parameters of the aeroGAIN-ROD module

Name	Value	Unit
Signal wavelength	1030-1040	nm
Signal core diameter	~85	μm
Mode field diameter ($1/e^2$ @1040 nm)	65 ± 5	μm
Pump cladding diameter	260 ± 15	μm
Pump cladding NA(FWHM@950 nm)	≥ 0.5	
Gain fiber length	804 ± 3	mm
Cladding absorption@915 nm	5 ± 0.5	dB
Cladding absorption@976 nm	~15(nominal)	dB
Typical optical efficiency	$\geq 60\%$	
Typical M^2	≤ 1.3	
End-cap dimensions(D \times L)	6×5	mm
End-cap coating R@ 1030 nm	$\leq 0.2\%$	
End-cap coating R@ 976 nm	$\leq 0.3\%$	
End-cap angle, input	≤ 0.5	$^\circ$
End-cap angle, output	2 ± 0.5	$^\circ$
Signal average power	≤ 100	W
Dimensions(W \times L \times H)	$35 \times 817 \times 35.2$	mm
Recommended water flow	> 2	L/min
Recommended water temperature	~25	$^\circ\text{C}$
Operating temperature	20-30	$^\circ\text{C}$

The schematic construction of the rod-type fiber amplifier and compressor is shown in Figure 2.15. The 976-nm pump beam was made to reverse pump the rod-type gain fiber module, where the pump was coupled into the module via a dichroic mirror. The output beam of the rod-type gain fiber module was collimated by the telescope with about 5 mm beam diameter to avoid thermal effects on the surface of these free space optical components. The 800 ps 1 MHz 1 μm pulses were well compressed to 245 fs by the reflection grating pair compressor (Fraunhofer grating pair). We were able to achieve an average output power of more than 90 W at 1 MHz by setting the working temperature of the pump diode at 38 °C. Actually, we operate the system at 55 W output power with 25 °C pump diode working temperature for long-term operation, and optimized the pulse compression for this operating point. The B-integral for the amplifier chain is conservatively estimated to be 4 radians at 55 W output power and 6 radians at 90 W output power. The efficiency of the reflective grating compressor was 95%. After careful optimization of the grating spacing and incidence angle (1480 groves/mm, 48° incident angle, 0.8m normal distance), the final output power of 55 W was compressed to 245 fs.

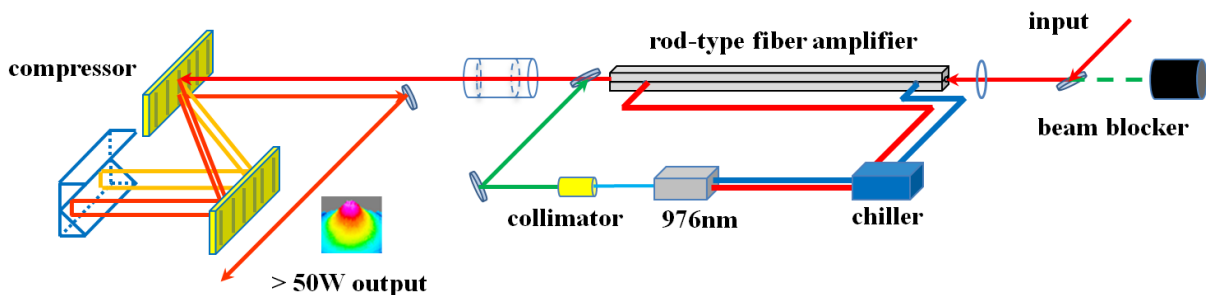


Figure 2. 15: Schematic construction of the rod-type fiber amplifier and compressor.

Figure 2.16(a) shows the spectra of the oscillator and the final output of the amplified 1- μm source. Figure 2.16(b) shows the autocorrelation trace of the compressed pulse. Figure 2.17 shows the calculated intensity autocorrelation trace based on the amplified pulse spectrum. The width of the autocorrelation trace was 345 fs, corresponding to a Gaussian pulse with a full width at half-maximum (FWHM) of 245 fs. Based on the spectrum of the compressed output, the calculated transform-limited pulse width is 190 fs. We estimate the peak power to be 224 MW assuming a Gaussian pulse shape. The small pedestal on the autocorrelation is due to small amounts of residual FOD in the system, accumulated nonlinear phase, and mode beating effects in the power amplifier.

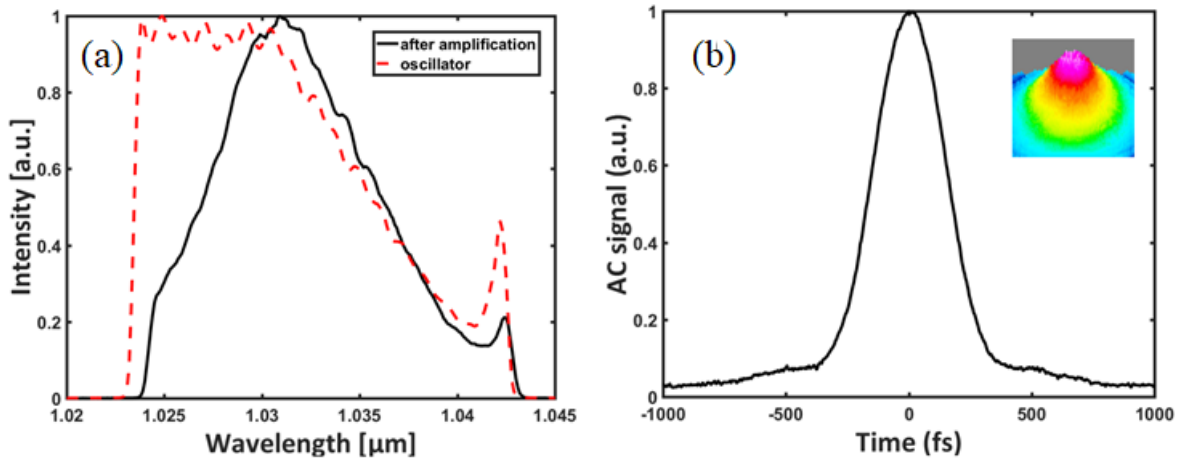


Figure 2. 16: Final output results of the 1- μm laser source.

The output spectrum of the amplified 1- μm laser is shown in (a). The compressed auto-correlation trace with duration of 250×1.4 fs is shown in (b). Inset picture of (b) is the beam profile token from the WinCamD.

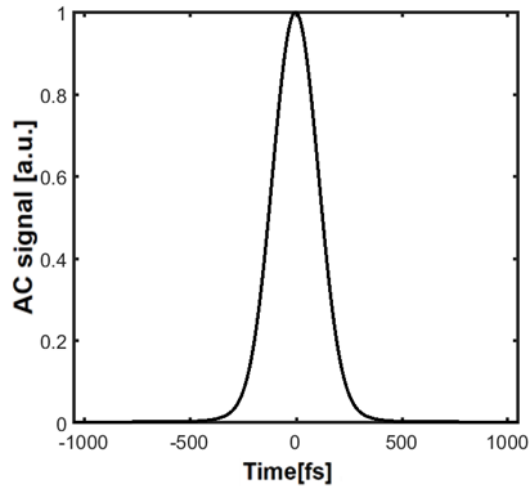


Figure 2. 17: Calculated 186×1.4 fs transform-limited intensity auto-correlation trace.

The duration of the calculated transform-limited auto-correlation trace is 190×1.4 fs.

2.3 SCHEMATIC LAYOUT OF THE SETUP



Figure 2. 18: Pictures of the home-build high power 1-MHz 1- μm laser source.

Figure 2.18 shows the pictures of the compact stable 1 μm all-fiber laser source. Figure 2.19 shows the specific schematic construction of the system. The setup was well sealed by optical enclosures to avoid the environmental influence and air disturbance. There was a water cooling system to stabilize the temperature of the setup, which was derived by a chiller working at 25 degree. We also inserted an oscilloscope into the setup to monitor the mode-locking state of the oscillator and an auto-correlator to monitor the profile of the output pulses.

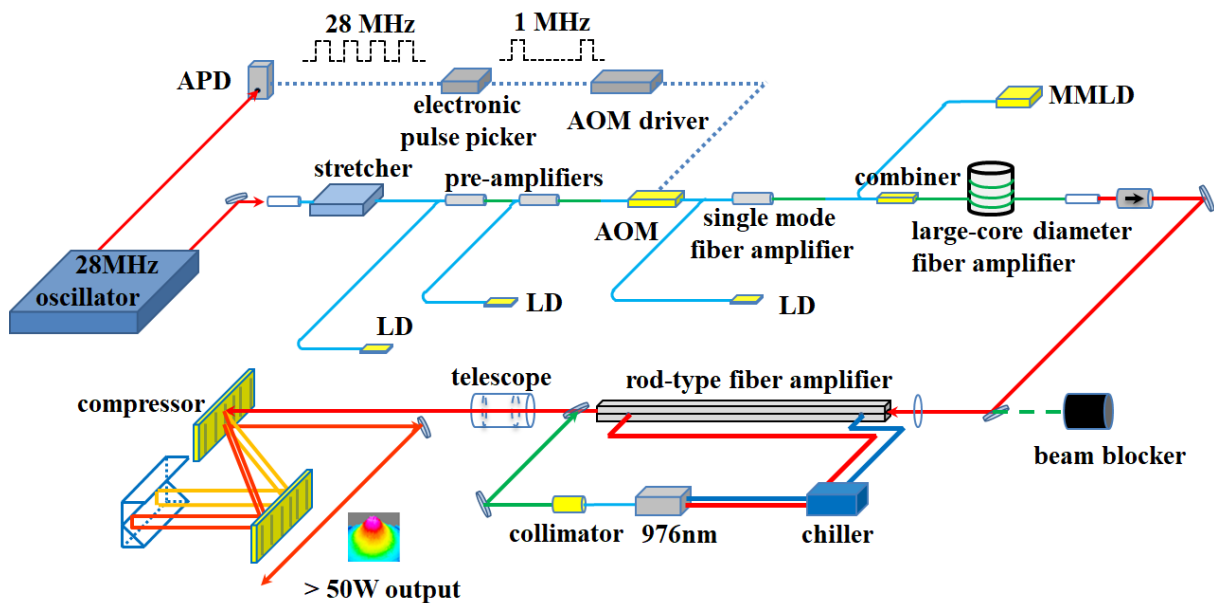


Figure 2. 19: Schematic construction of the 1- μm laser source. MMLD: multi-mode laser diode; LD: laser diode; AOM acoustic-optic modulator; APD: avalanche photon detector.

2.4 JOULE-CLASS 500 HZ CRYOGENIC Yb:YAG CHIRPED PULSE AMPLIFIER BASED ON ALL-FIBER FRONT-END

Though it is very easy for the fiber amplifier to amplify the pulse energy to μJ -level with the method of CPA, solid-state amplification is still a proper way to amplify pulse energy of the seed pulses to even joule level for high pulse energy applications. As a stable, compact front-end source, the stretched seed pulses with nice beam profile from the fiber front-end mentioned above can be used as the seed pulses for the subsequent solid-state amplifiers to achieve super high pulse energy at 500 Hz repetition rate. With the ~ 3 -ns fiber front-end introduced in section 2.2.2, we amplified the seed pulse to the J-level using three cascaded stages of solid-state amplifiers, which are the Yb:KYW dual-crystal regenerative amplifier shown in Fig 2.22, the 12-pass cryogenic Yb:YAG

composite-thin-disk amplifier shown in Figure 2.23(a) and the Joule-class 500-Hz 16-pass cryogenic Yb:YAG composite-thin-disk amplifier shown in Figure 2.23(b).

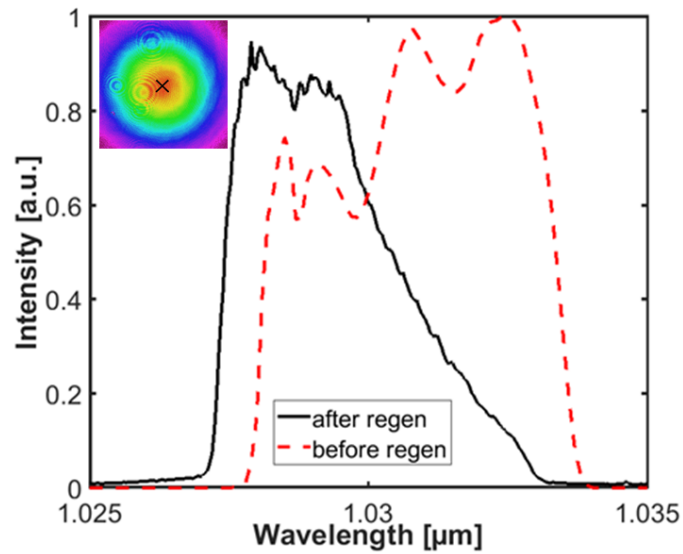


Figure 2. 20: Spectra of the seed pulse (red dashed curve) and amplified pulse after regenerative amplifier (black curve). The inset picture is the beam profile after the amplifier.

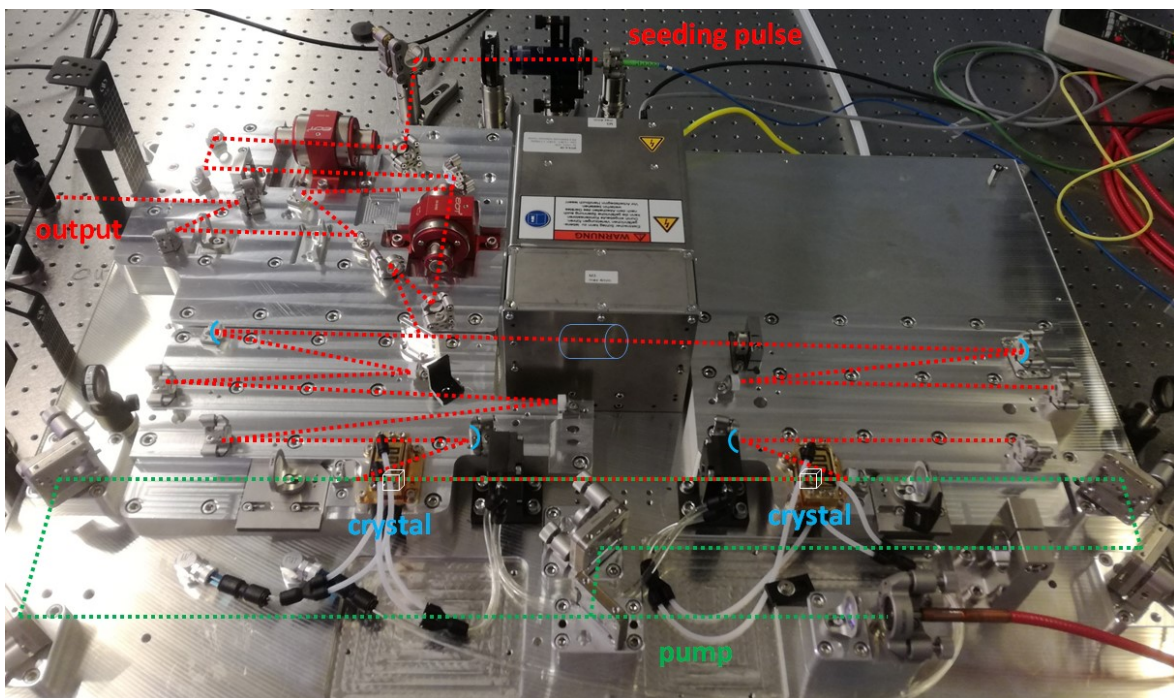


Figure 2. 21: Picture of mJ-level regenerative amplifier.

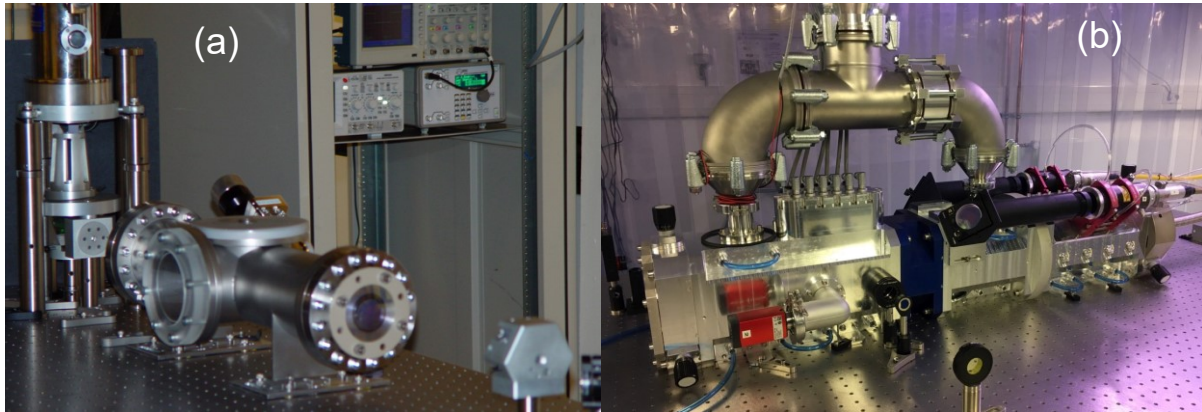


Figure 2. 22: (a) Picture of the 12-pass cryogenic Yb:YAG composite-thin-disk amplifier, (b) Picture of the Joule-class 500-Hz 16-pass cryogenic Yb:YAG composite-thin-disk amplifier.

Working at 1 kHz repetition rate, the Yb:KYW regenerative amplifier can safely amplify the pulse energy of the seed pulse to ~ 5.5 mJ. As is shown in Figure 2.20, since there was severe spectral narrowing during the amplification process, the pulse duration for the amplified pulse changed to ~ 2 ns. The beam profile after the amplification of the regenerative amplifier is shown in the inset picture of Figure 2.20. After pre-amplification to the mJ-level the seed pulse is further amplified to about 100 mJ inside the 12-pass composite-thin-disk amplifier, the pulse energy of the 1- μm pulses are then further amplified to 1.2 J with ~ 300 ps pulse duration by the Joule-class 500-Hz 16-pass cryogenic Yb:YAG composite-thin-disk amplifier. The beam profile of the 1-J beam is shown in Figure 2.23

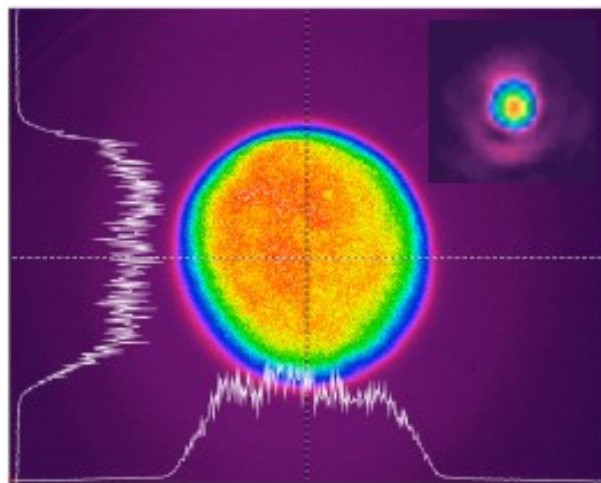


Figure 2. 23: The ~ 18 mm beam shows a supergaussian near-field profile, diffraction limited spot (plus some scatter) is in the inset picture of the far-field.

2.5 CONCLUSIONS

We demonstrate a $>55\text{-}\mu\text{J}$, 1-MHz, 245-fs, 1- μm fiber-based laser source with a peak power in excess of 200 MW and 55 W average power with diffraction limited beam quality. The repetition rate of the 1- μm pulses was decreased from 28 MHz to 1 MHz by using the optical pulse picker consisting of an AOM and electronic pulse picker. Through careful dispersion and gain management we avoid the accumulation of excess nonlinear phase and high order dispersion to allow clean pulse compression to within 30% of the transform limit at high peak power with minimal satellite pulses from the all fiber system. This fiber-based laser system is stable and compact. It is ideally suitable for applications that demand a highly reliable source of high-energy high-repetition rate pulses, such as OPCPA and high harmonic generation experiments.

CHAPTER 3: HIGH-POWER FEMTOSECOND 1- μM CIRCULARLY POLARIZED PRE-CHIRP MANAGED AMPLIFICATION SYSTEM

The CPA technique can help us to avoid detrimental nonlinear effects inside polarization maintaining fiber amplifiers and amplify the pulse energy of seed pulses to the required energy level satisfying applications in need for high pulse energy. One limitation of CPA is the grating size limitation, which can be also considered as the final limitation [112-116]. The increased distance of the grating stretcher and compressor can make the systematic compactness worse and increase the instability of the system after power amplification over 100-W. Furthermore, the pulse duration of compressed linearly polarized pulse is typically limited to values around 200 fs due to the gain narrowing effect and residual dispersion mismatch. Further reduction in pulse duration needs an external nonlinear pulse-compression stage applying the method of SPM. The nonlinear compression stage can increase the system complexity, deteriorate the long term stability, and reduce the output average power [117-119].

PCMA is the nonlinear fiber amplification technique developed in recent years [120,121]. When the amplified pulse peak power is below the critical power of self-focusing effect [122], the PCMA can perfectly avoid these potential issues of CPA listed above. Seed pulses are nonlinearly amplified during the amplification process due to the SPM effects, so that the amplified spectrum can be substantially broadened. The SPM effect can be enhanced by proper negative pre-chirp on the seed pulses. The negative pre-chirp of seed pulses can first be compensated by the normal GVD of the 1- μm fiber

amplifier to zero and then broadened by the normal GVD in the rest part of the fiber amplifier. Therefore, only several millimeters separation distance can be needed for grating pair compressor to compress amplified pulses. There is strong SPM effect at the zero GDD point inside the fiber amplifier leading to the broadband amplified spectrum and extreme short pulse duration after compression. However, based on the Kerr effect, after amplifying the peak power of seed pulses over the critical power threshold of self-focusing effect, the amplified pulse can ionize the gain material leading to damage the fiber amplifier. Shown in equation 3.0.1, the critical peak power for self-focusing effect grows quadratically with wavelength and decreases linearly with the linear and nonlinear refractive coefficients n_0, n_2 .

$$P_{\text{crit}} = \alpha \frac{\lambda^2}{4\pi n_0 n_2} \quad (3.0.1)$$

α depends on the spatial distribution of the beam and equals 1.9 for Gaussian beam. The nonlinear refractive coefficient n_2 is equal to $\approx 2.6 \times 10^{-16} \text{ cm}^2/\text{W}$. The calculated critical peak power for self-focusing effect is $\approx 4 \text{ MW}$, which means the maximum pulse energy should be lower than $4 \mu\text{J}$ at 1 ps pulse duration in fiber (fused silica) to avoid generating the self-focusing effect.

The newly invented isotropic Yb-doped rod-type PCF can be kept straight in the metal container to avoid polarization rotation inside the fiber caused by external tension and other environmental impacts. Therefore, the Yb-doped rod-type PCFs can be treated as PM fibers. Both of the PM circular polarization amplification and the PM linear polarization amplification can also be applied inside rod-type fiber amplifiers. Based on equations 2.1.1 and 2.1.2, the peak power of the circularly polarized pulse can be amplified to about 1.5 times higher than the linearly polarized pulse for accumulating the same nonlinear phase. The critical power threshold for self-focusing effect of circularly polarized pulse is also 1.5 times higher than the linearly polarized pulse. The method of circularly polarized pulses amplification provides a sufficient way to avoid the self-focusing effect when the peak power of operating laser pulse is near the critical power of self-focusing effect. Since the spectrum can be broadened by the SPM effect and the amplified pulse can be compressed to tens-femtoseconds level by the compressor, the compactness and stability of the system can also be extremely improved.

3.1 SYSTEM LAYOUT OF THE 100-W 1- μM LASER SYSTEM

The 100-W, 1- μm system consists of two stages, the pre-CPA stage and the CP-PCMA stage. The Pre-CPA stage was mainly used to scale up the pulse energy of seed pulses for the subsequent rod-type fiber amplifier. The CP-PCMA stage was used to amplify average power of circularly polarized seed beam above 100 W without generating the self-focusing effect. Seed pulses were generated from the 24-MHz home-made 1- μm oscillator shown in Figure. 3.1. The seed pulse was stretched by the all-fiber stretcher consisted of negative TOD stretcher fiber and PMSMF from 2 ps to ≈ 30 ps. The average power of stretched pulses was amplified to ≈ 5 W by the PMSMF signal amplifier and the PM large-core diameter fiber power amplifier. The transmission grating pair (1000 line/mm) after the large core diameter fiber amplifier worked as the pre-chirper to pre-chirp the near transform-limited seed pulse. Therefore, the SPM effect inside the rod-type fiber amplifier can be enhanced. There was a grating pair compressor (1000 line/mm) used to compensate the residual dispersion of the amplified seed pulses after the nonlinear amplification stage.

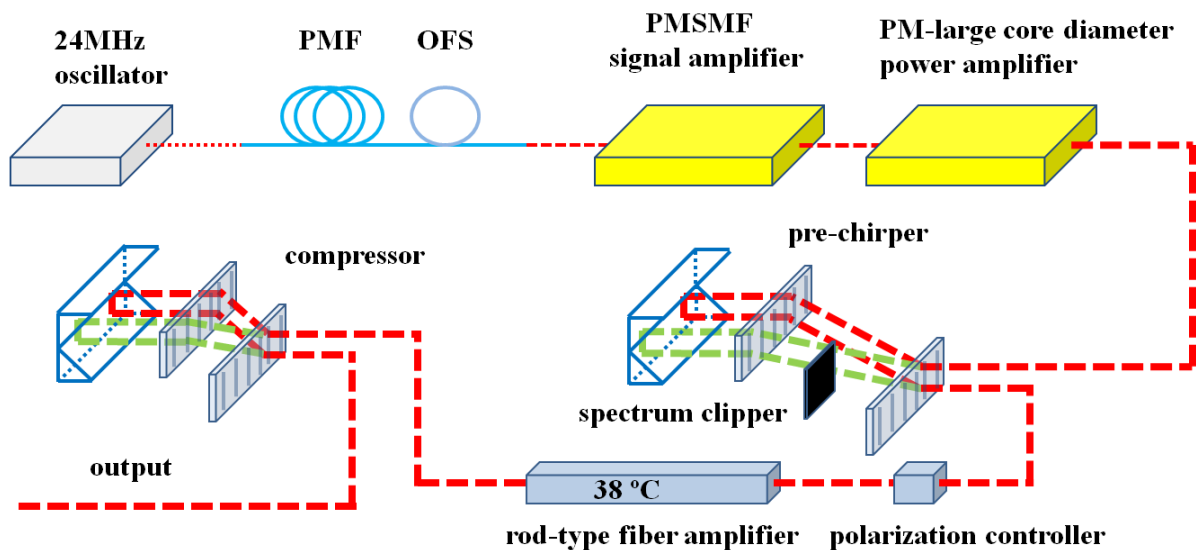


Figure 3. 1: System layout of the home-built 100-W 1- μm laser source. PMF: polarization maintaining fiber; OFS: OFS stretcher-fiber; PMSMF: polarization maintaining single-mode fiber.

3.2 PRE-CPA STAGE FOR CP-PCMA

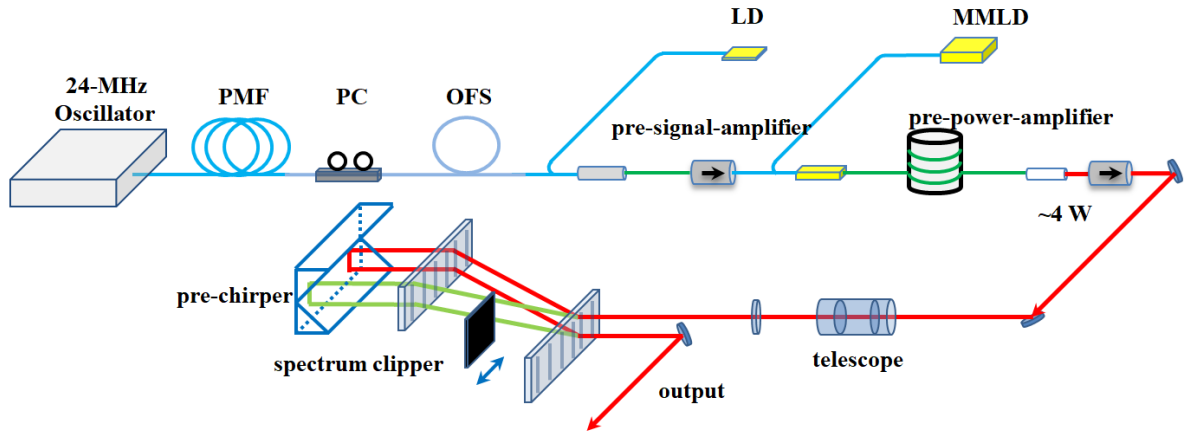


Figure 3. 2: Schematic construction of the pre-CPA stage for CP-PCMA.

PMF: polarization maintaining fiber; PC: polarization controller; OFS: OFS stretcher-fiber; LD: laser diode.

It is necessary to generate watt-level seed pulses with near transform-limited pulse duration for testing the performance of CP-PCMA in the rod-type fiber amplifier. Therefore, a Watt level pre-CPA stage was built to amplify 1- μm seed pulses. The CPA can help us to avoid generating nonlinear effects inside pre-amplifiers. The pulse duration of amplified seed pulses can be compressed to near transform-limited by the grating pair pre-chirper after doing the dispersion management of the pre-CPA stage. The pre-chirper can be used to provide pre-chirp to compressed seed pulses based on the well-compensation separation distance of the grating pair.

The schematic construction of the pre-CPA stage is shown in Figure 3.2. Seed pulses from the 24-MHz oscillator were stretched to about 30 ps by the all-fiber stretcher consisted of 45-m PMSMF and 3.5-m negative TOD stretcher fiber. The polarization controller mounting was used to adjust the polarization rotation inside the non-PM stretcher fiber. Therefore, the polarization dispersion cannot be generated in cascaded fiber amplifiers optimizing the polarization extinction ratio of the output beam. There were two stages of pre-amplifiers to amplify stretched seed pulses, the pre-signal amplifier and the pre-power amplifier. There was $\approx 50\text{-cm}$ Yb-doped polarization maintaining gain fiber (Yb-401PM) used to build the signal amplifier to amplify 24-MHz seeding pulses from $\approx 1\text{ mW}$ to $\approx 60\text{ mW}$. $\approx 1.3\text{-m}$ 12- μm core diameter Yb-doped PM double-cladding fiber (LIEKKI Yb1200-12/125) was used to build the pre-power amplifier to scale up the average power of seed pulses from 60 mW to about 5 W. The amplified seed beam was collimated by the telescope with 3-mm beam diameter. The

pulse duration of pre-amplified seed pulse was compressed to near transform-limited by the grating pair pre-chirper together with a spectral clipper.

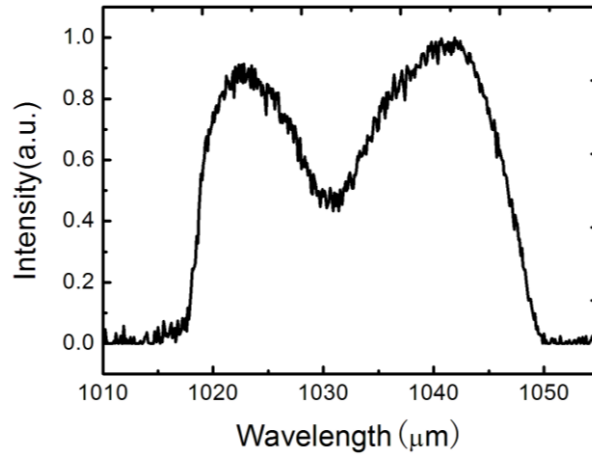


Figure 3. 3: Spectrum of the seed pulse output from the 24-MHz oscillator.

The output spectrum of the 24-MHz oscillator is shown in Figure 3.3. Getting rid of the wavelength range below 1030 nm can help us to compress the pulse duration of the amplified pulse to near transform-limited with clean pulse profile based on our calculation in section 2.2.4. Shown in Figure 3.2, a spectral clipper was inserted into the grating pair to get rid of the spectral content below 1030 nm. The clipped spectrum is shown in Figure 3.4(a). The average power loss caused by the spectral clipper was $\approx 10\%$. The efficiency of the transmission grating pair (Lightsmyth, 1000 line/mm) pre-chirper was about 80%. The final output power after the compressor was ≈ 3.6 W. Figure 3.4(b) shows the measured intensity auto-correlation trace (red curve) and the calculated transform-limited intensity auto-correlation trace (black curve) based on the spectrum shown in Figure 3.4(a). The measured pulse width of the intensity auto-correlation trace was 218×1.4 fs with Gaussian assumption, which is 1.09 times longer than the calculated transform-limited pulse width 200 fs. Therefore, the 1- μm pre-chirped pulse can be used as seed pulse for the further CP-PCMA experiments after using the pre-chirper to pre-chirp this near transform-limited 1- μm seed pulse. We can make the seed pulse negative pre-chirped or positive pre-chirped to realize the method of PCMA in further amplification by varying the separation distance of the grating pair pre-chirper from the zero GDD dispersion point. The polarization of the seed pulse was rotated by the free-space polarization controller from linear polarization to circular polarization satisfying the CP-PCMA system.

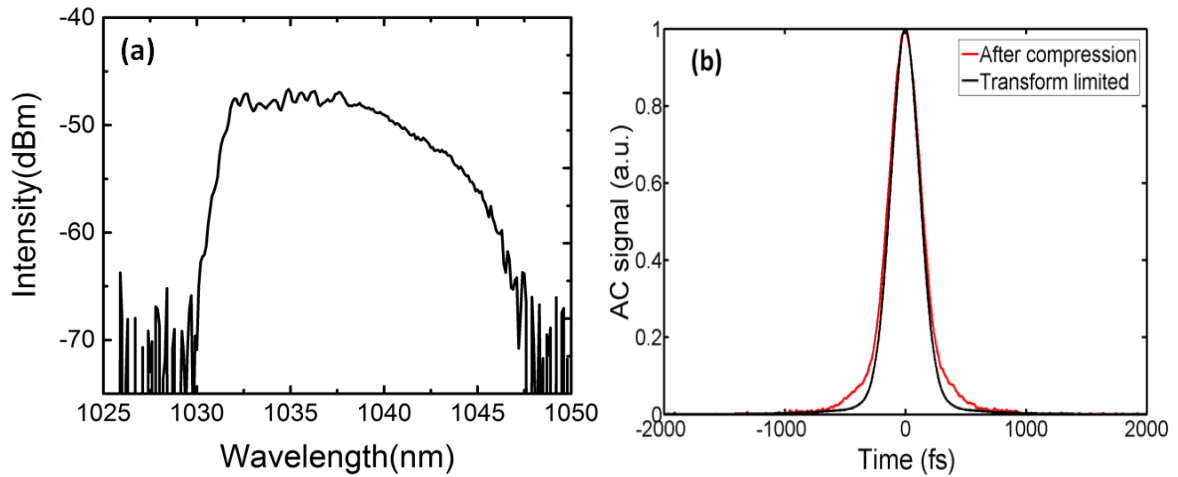


Figure 3. 4: (a) Spectrum of the clipped amplified seed pulse; (b) Calculated intensity auto-correlation trace and measured intensity auto-correlation trace. In (b), the measured duration of the intensity auto-correlation trace was 218×1.414 with Gaussian assumption (red curve) and the calculated intensity auto-correlation trace based on (a) with 283 fs pulse width.

$\approx -20000 \text{ fs}^2$ to $\approx -60000 \text{ fs}^2$ negative GDD was added to pre-chirp seed pulses to investigate the CP-PCMA process. We also did the investigation for the CP-PCMA system with $+30000 \text{ fs}^2$ positively pre-chirped seed pulses based on our formal results [121].

3.3 RESULTS AND ANALYSIS OF THE CP-PCMA SYSTEM

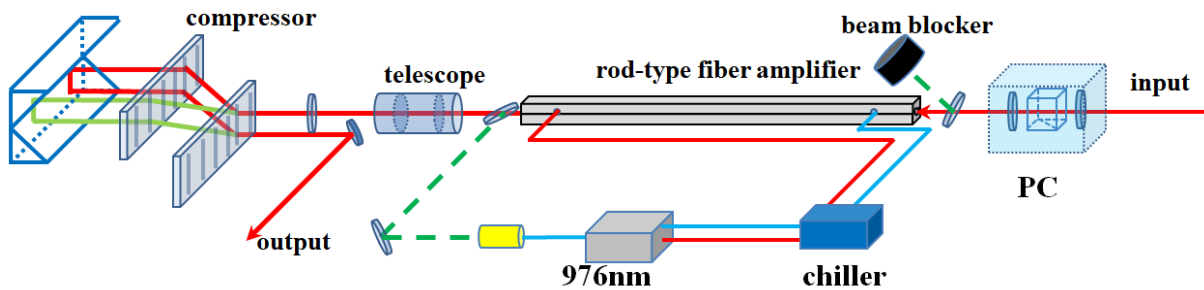
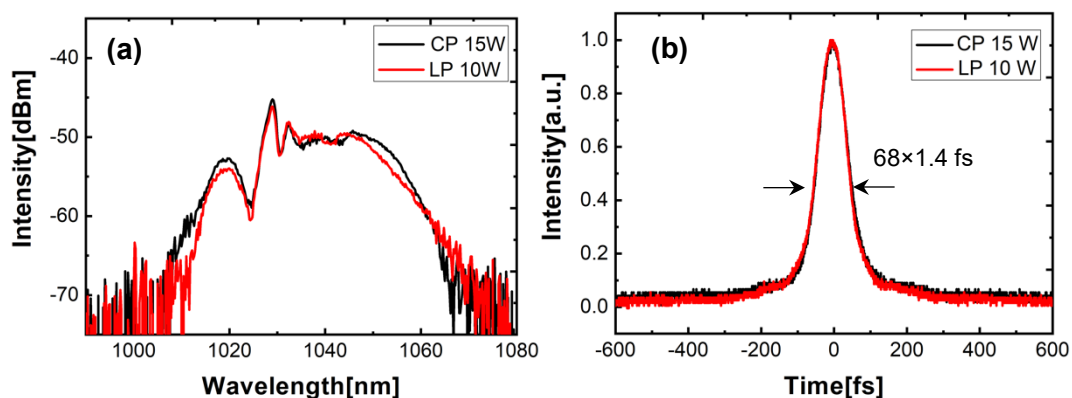


Figure 3. 5: Schematic layout of the CP-PCMA using the rod-type fiber amplifier. PC: polarization controller.

The CP-PCMA system consists of the free space polarization controller, the rod-type fiber amplifier and the transmission grating pair compressor is shown in Figure 3.5. The free-space polarization controller was a combination of a half waveplate, a polarization beam splitter and a quarter waveplate. The combination of the half waveplate and the PBS was used to improve the polarization extinction ratio to $>30 \text{ dB}$ avoiding impacts on

the the amplified spectrum generated by unwanted polarization. The polarization of the seed pulse was rotated by the quarter waveplate from linear polarization to circular polarization. The seed beam was coupled into the rod-type fiber amplifier after the free-space polarization controller. Average power of the seed beam can be amplified from watts level to ≈ 130 W. The rod-type fiber amplifier consisted of the aeroGAIN-ROD module (NKT), the chiller, and the 976-nm 500-W pump laser (LDM-500, laserline).

The pulse width of amplified negatively pre-chirped pulses before final compression was ≈ 1 ps. Therefore, the peak power of the amplified pulse should be below $4 \mu\text{J}$ for linearly polarized pulse and $6 \mu\text{J}$ for circularly polarized pulse to avoid the self-focusing effect. The transmission grating compressor consisted of the telescope, the transmission grating pair (1000 line/mm, lightsmyth) and the right angle prism pair. It was used to collimate the beam and compress the amplified pulses with about 80% compression efficiency. We managed to control the polarization of the seed pulses to do the CP-PCMA using the free-space polarization controller,. After amplifying the average power of circularly polarized beam 1.5 times higher than the linearly polarized beam, we managed to get the spectra and intensity auto-correlation trace after compression of the circularly polarized pulse and linearly polarized pulse. Figure 3.6 shows the spectra and intensity auto-correlation trace of the amplified negatively pre-chirped linearly polarized pulse and circularly polarized pulse. The amount of the negative per-chirp varied from -20000 fs^2 to -60000 fs^2 to achieve the best compression results.



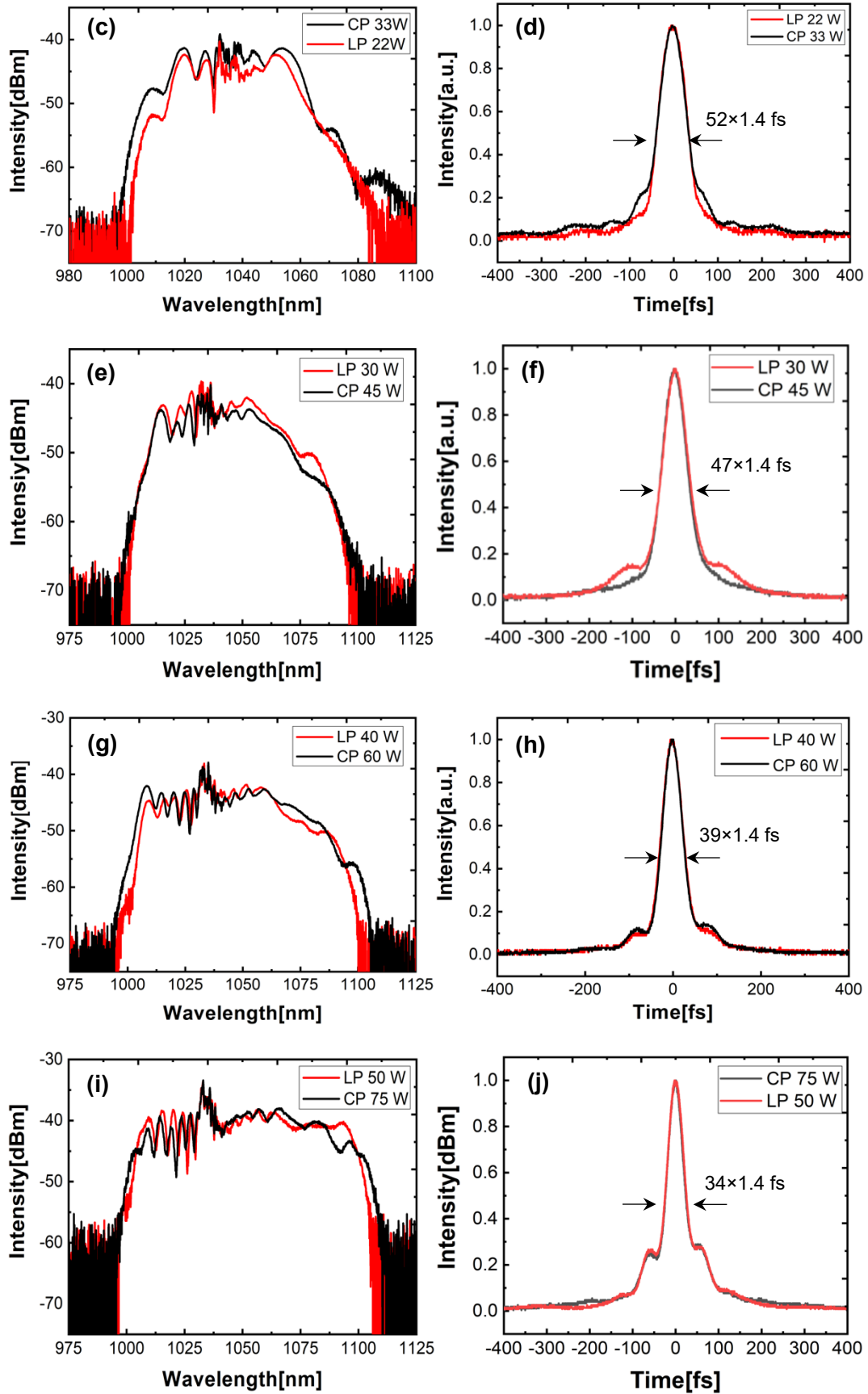


Figure 3. 6: Spectra and intensity auto-correlation trace of the amplified negatively pre-chirped seed pulses with linearly polarization and circularly polarization. The average power of the amplified circularly polarized pulses was about 1.5 times higher than the linearly polarized pulses.

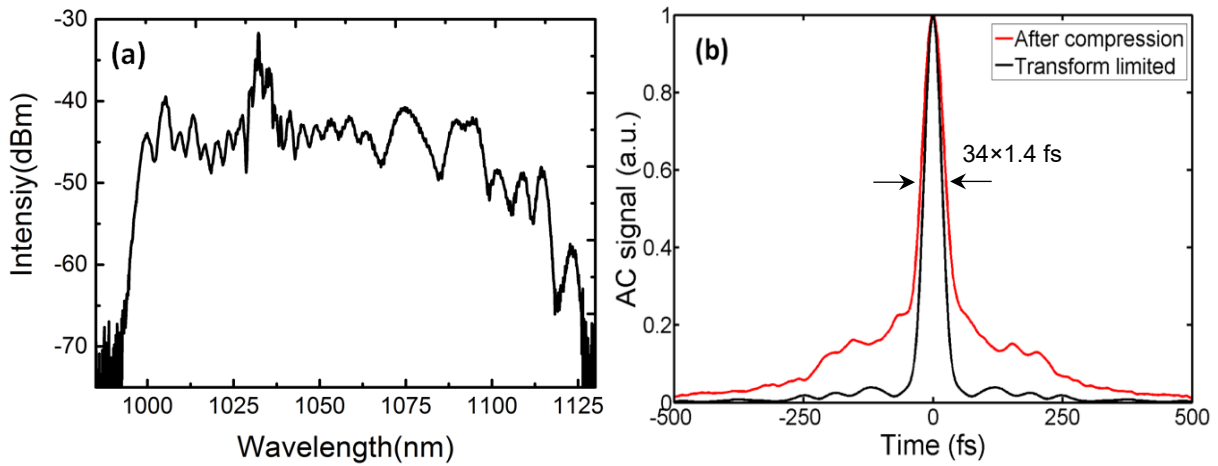


Figure 3. 7: Spectrum of the 100 W amplified negatively pre-chirped pulse and its intensity auto-correlation trace.

Shown in equation 2.2.1 and 2.2.2, the nonlinear phase should be the same when we amplify the average power of the circularly polarized pulses 1.5 times higher than the linearly polarized pulses since the nonlinear refraction coefficient of the linearly polarized pulse is 1.5 times higher than the circularly polarized pulse. We did power scaling experiments based on our theory to prove the prediction. Shown in Figure 3.6, we did the power scaling of the linearly polarized seed pulses to 10 W, 20 W, 30 W, 40 W, and 50 W and took the spectrum and auto-correlation trace of the amplified pulse. The spectrum and auto-correlation trace of the circularly polarized pulses with 1.5 times higher average power matched perfectly with linearly polarized pulses. There was strong self-phase modulation effect during the high power nonlinear amplification process, which broadened the spectrum and made the pulse duration of compressed pulses shorter. Based on our results, the amplified circularly polarized pulses accumulate the same nonlinear phase with 1.5 times higher average power compared with the amplified linearly polarized pulses. Therefore, the critical power of the self-focusing effect of the circularly polarized pulses was also 1.5 times higher than the linearly polarized pulses. Higher amplified power means more broaden spectrum and shorter compressed pulse duration in the PCMA. However, too much nonlinear phase can also cause the uncompressed pedestals shown in Figure 3.6(j). The residual nonlinear phase may probably be inhibited by changing the incidence angle of the transmission grating pair or add some TOD to seed pulses in the pre-chirper. We finally amplified circularly polarized seed pulses to ≈ 100 W after the compressor with $\approx 80\%$

compression efficiency. The measured pulse width of the uncompressed 130 W pulses was 1 ps. This means the pulse energy amplified circularly polarized pulse was about 5.5 μJ . It was 1.5 μJ higher than the critical power of the linearly polarized pulse and lower than the estimated 6- μJ of the circularly polarized pulse. The spectrum and auto-correlation trace of the 100-W amplified circularly polarized pulse were both shown in Fig 3.7. The bandwidth of the spectrum was broadened to about 100 nm. Pedestals were caused by the uncompensated residual nonlinear phase.

Further, there was the comparison experiment between 60-W amplified linearly polarized seed pulses and 60-W amplified circularly polarized seed pulses. Figure 3.8 shows the spectrum of the 40-W linearly polarized pulse (red curve), the 60-W circularly polarized pulse (black curve), and the 60-W linearly polarized pulse (blue curve) after rod-type fiber amplification. The spectrum of the 60-W linearly polarized pulse was much broader than the 60-W linearly polarized pulse. This was caused by that the 60-W linearly polarized pulses accumulated about 1.5 times more nonlinear phase than the 60-W circularly polarized pulses during the nonlinear amplification process via SPM effect.

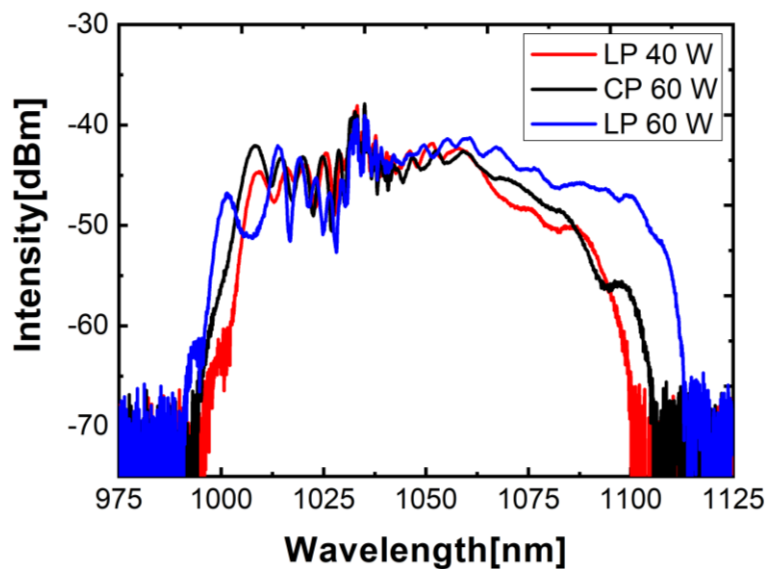


Figure 3. 8: Spectra of the 40 W linearly polarized pulse, 60 W circularly polarized pulse and 60W linearly polarized pulse.

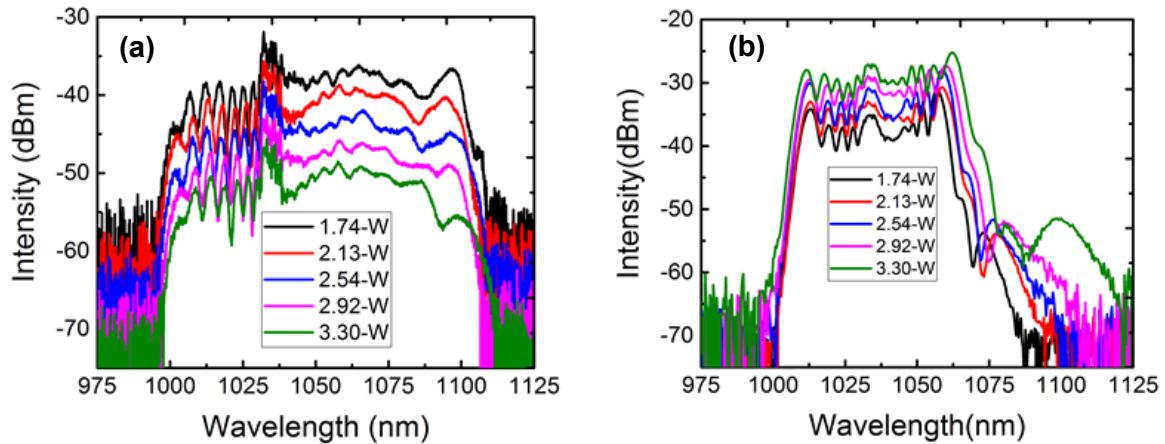


Figure 3. 9: (a) Spectra of the negatively pre-chirped 75 W circularly polarized pulse with different input power; (b) Spectra of the positively pre-chirped 75 W circularly polarized pulse with different input power.

Further investigation was done on spectral variation of the negatively pre-chirped seed pulse and the positively pre-chirped seed pulse after being amplified in the rod-type fiber amplifier with different input power. Figure 3.9 (a) shows the spectra of the -30000fs^2 negatively pre-chirped amplified seed pulse with input power scaling from 1.7 W to 3.3 W. Figure 3.9 (b) shows the spectra of the $+30000\text{fs}^2$ positively pre-chirped amplified seed pulse with input power scaling from 1.7 W to 3.3 W. The GVD of the rod type fiber provides normal dispersion to the 1- μm seed pulse. Therefore, negatively pre-chirped seed pulses were compressed and positively pre-chirped seed pulses were stretched during the propagation during the propagation of seed pulses in rod-type fiber. The peak power of negatively pre-chirped pulses was higher than positively pre-chirped pulses during the amplification process with the same input power. Therefore, negatively pre-chirped pulses accumulates more nonlinear phase than the positively pre-chirped pulse. Further, the spectrum of negatively pre-chirped amplified pulses was much broader than positively pre-chirped amplified pulse due to the SPM effect after being amplified to the same average power level with the same input power.

Positively pre-chirped pulses with higher input average power after amplification have broader spectrum due to the higher pulse peak power at the beginning of the amplification process accumulating more nonlinear phase. The spectrum of the negatively pre-chirped amplified pulse didn't vary a lot compared with the positively pre-chirped pulse for the same circumstance. The nonlinear phase difference of negatively pre-chirped pulses caused by different input power was negligible compared with total amounts of the accumulated nonlinear phase during the amplification process.

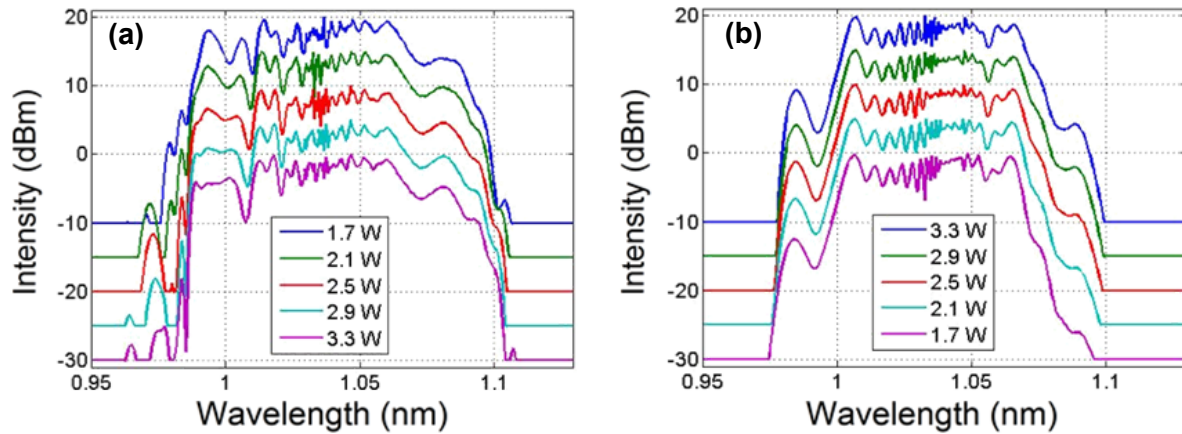


Figure 3. 10: (a) Calculated spectra of the negatively pre-chirped 95 W circularly polarized pulse with different input power; (b) Calculated spectra of the positively pre-chirped 95 W circularly polarized pulse with different input power.

We did the simulation for amplifying the average power of the seed beam to ≈ 95 W after the rod-type fiber amplifier, which means ≈ 75 W output power considering about the 80% compression efficiency. Figure 3.10 (a) shows the spectral variation of the amplified negatively pre-chirped (-30000fs^2) pulse with different input power. Figure 3.10 (b) shows the spectral variation of the amplified positively pre-chirped ($+30000\text{fs}^2$) pulse with different input power. The spectrum bandwidth of the negatively pre-chirped pulse is broader than the positively pre-chirped pulse after amplifying the seed beam to about 95 W. The spectrum bandwidth of the negatively pre-chirped pulse after amplification doesn't vary significantly with different input power. But there was a significantly spectral broadening for the positively pre-chirped pulse with different input power. The calculation results matched with our experimental results and proved our conclusion.

We further calculated the compression results for the 95-W negatively pre-chirped pulse and positively pre-chirped pulse with the grating pair (31.3° incidence angle, 1000 line/mm) compressor shown in Figure 3.11. Negatively pre-chirped pulses can be compressed shorter due to stronger SPM effect. The accumulated nonlinear phase for the negatively pre-chirped pulse can make the spectrum broader and also compensate the high order dispersion during the amplification process compared with positively pre-chirped. Therefore, the negatively pre-chirped pulse with stronger SPM effect can have lower pedestals and shorter compressed pulse duration than the positively pre-chirped pulse. There is a conclusion that, it is easier to get a better compressed pulse with the negatively pre-chirped seed pulses with the same input parameters. Figure 3.12(a) shows the calculated amplified output power and the corresponding pump

power along the rod-type fiber during the amplification process. Figure 3. 12(b) shows the gain curve of the rod-type fiber amplifier with reversed pumping.

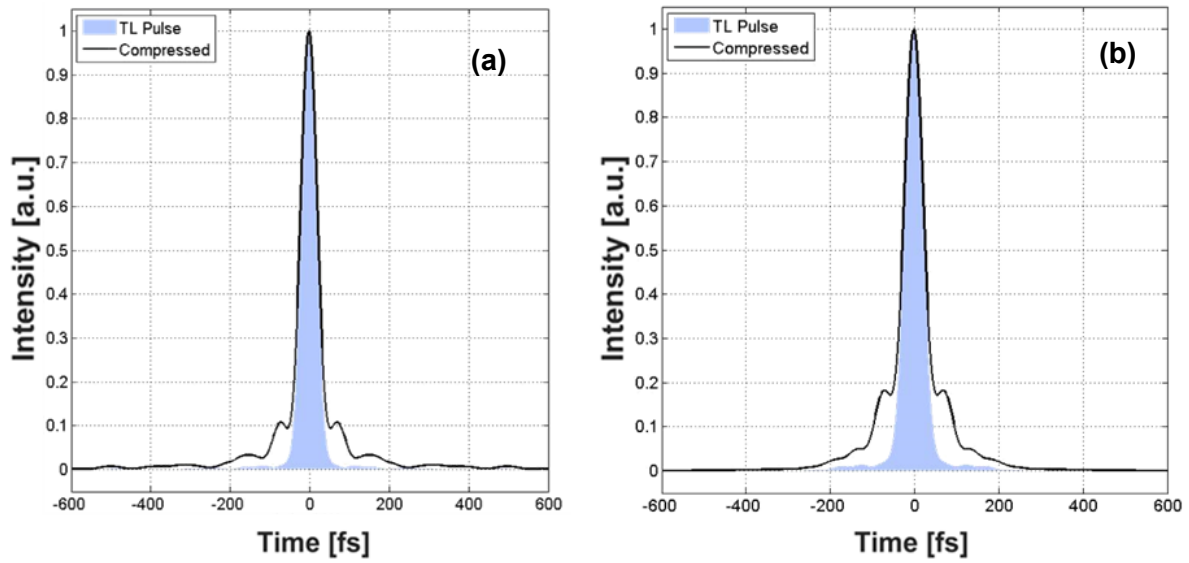


Figure 3. 11: (a) Calculated auto-correlation trace of the compressed negatively pre-chirped pulse; (b) Calculated auto-correlation trace of the compressed positively pre-chirped pulse.

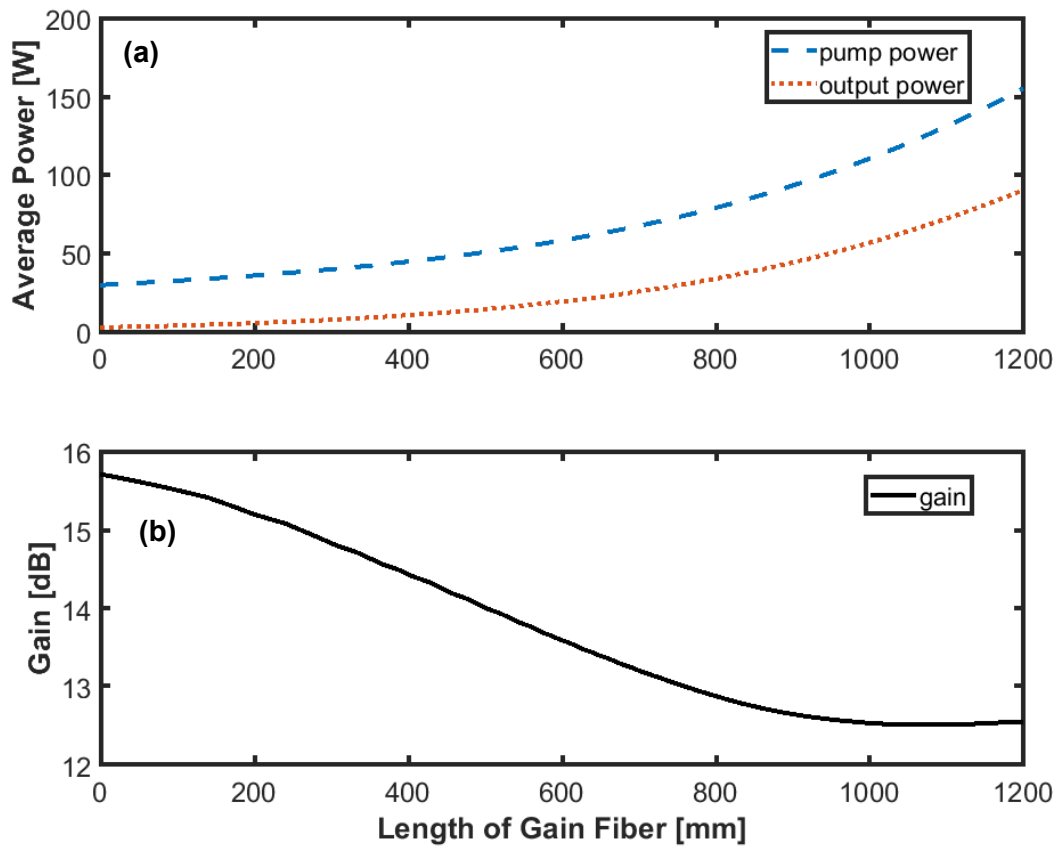


Figure 3. 12: (a) Calculated amplified output power (red dashed curve) and related pump power (blue dashed curve) during the process of the amplification; (b) Gain curve of the rod-type fiber amplifier.

3.4 SCHEMATIC CONSTRUCTION OF THE CP-PCMA SYSTEM

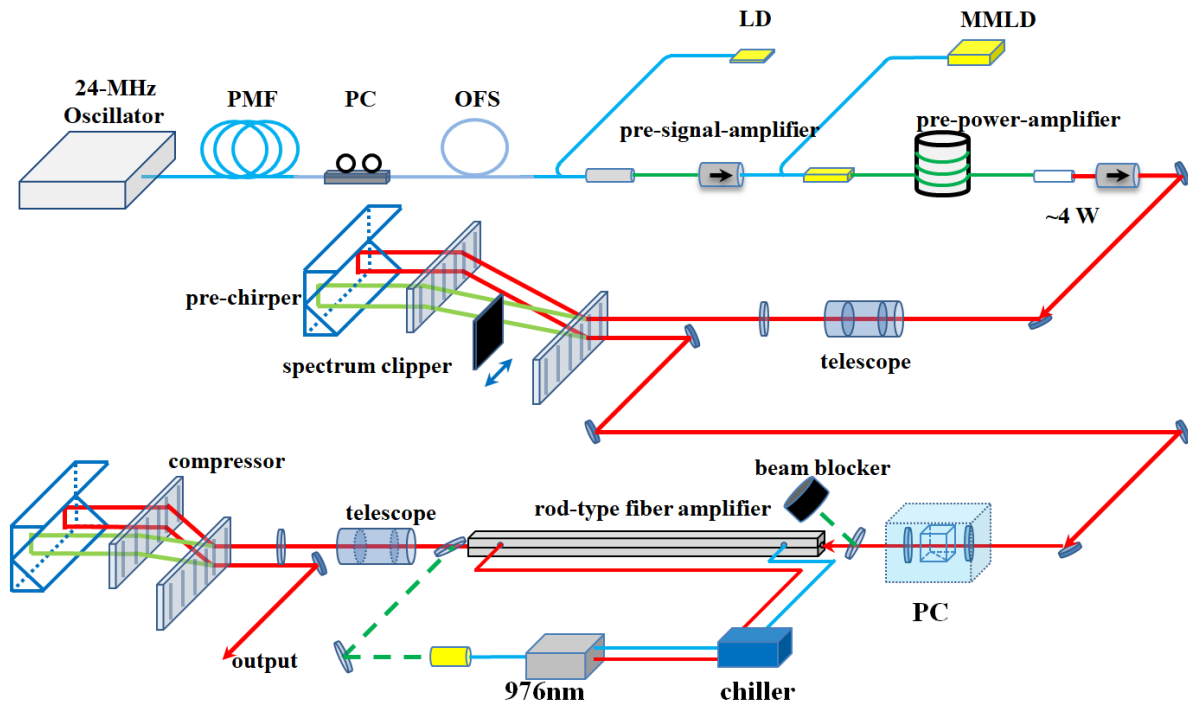


Figure 3. 13: Schematic construction of the 100-W 1- μm CP-PCMA system.

The schematic construction of the 100-W 1- μm CP-PCMA experimental setup is shown in Figure 3.13. The whole system can be separated into the oscillator, fiber stretcher, pre-signal amplifier, pre-power amplifier, pre-chirper, polarization controller, rod-type fiber amplifier and grating pair compressor. Seed pulses were generated from the 24-MHz 1- μm oscillator, and stretched to ~ 30 ps by the all fiber stretcher. Stretched linearly polarized seed pulses were amplified by the PM single-mode pre-signal-amplifier and the PM large core diameter ytterbium doped double cladding pre-power-amplifier to maximum 5 W. The free-space polarization controller helped to change the polarization of the seed beam from linear polarization to circular polarization. The seed beam was finally amplified in the rod-type fiber amplifier, which is pumped by 976 nm multimode pump diode working at 38 °C. The chiller for controlling the working temperature of the pump diode is from Termotek, which can set the working temperature of the chiller at 38 degree. The amplified seed beam was collimated by the telescope and compressed by the grating pair compressor (1000 line/mm) with 31.3° incidence angle. The final output average power was ≈ 100 W after compression. The efficiency of the compressor was ≈ 80 %. Figure 3.14 shows the picture of the 100-W, 1- μm CP-PCMA system.

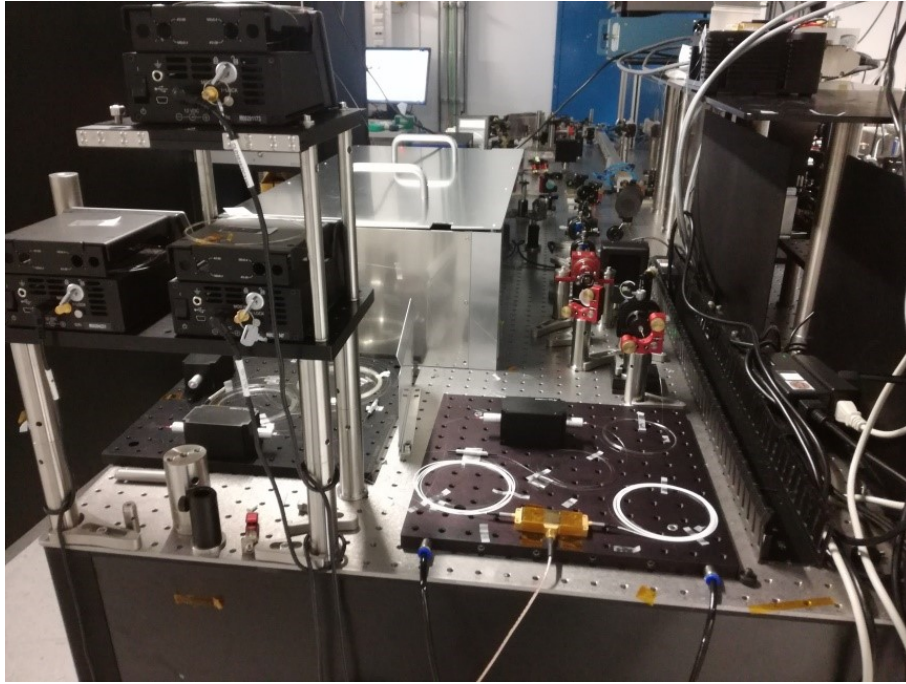


Figure 3. 14: Picture of the home-build 100-W experimental setup.

3.5 CONCLUSIONS

We demonstrated a 100-W, 24-MHz, 40-fs, 1- μm CP-PCMA high power fiber laser system. There was a pre-CPA stage with the home-made fiber stretcher, which was designed to generate the pre-chirped Watt level seed beam for the final rod-type fiber amplifier to do the CP-PCMA. The negatively pre-chirped seed beam was finally amplified to 130 W before compression. After compressing the amplified seed pulse with the grating pair compressor, the final output power of the 24-MHz, 1- μm beam was 100 W with $\approx 80\%$ compression efficiency. The pulse duration of the amplified circularly polarized seed pulse was 34 fs.

The critical power of the self-focusing effect of the circularly polarized pulses is 1.5 times higher than the linearly polarized pulses with the method of circularly polarized amplification. It can help us to avoid the damage of gain fiber when we try to run the system on the edge of self-focusing effect. Furthermore, the method of CP-PCMA can help to avoid further nonlinear compression modules to achieve few-cycle pulse duration. Therefore, the insertion loss of the nonlinear compression module can be avoided making the system more compact and stable.

CHAPTER 4: 1-MHz, 1- μ J, PASSIVELY CEP-STABLE, FEMTOSECOND 2.1- μ M OPA SYSTEM

In recent years, demands for high-repetition-rate, few-cycle, CEP-stabilized, high-power laser sources rapidly increased and experienced technological advancements due to its particular importance in strong-field physics. High-repetition-rate (MHz-level) pulses with few-cycle μ J-level pulse energy can significantly improve statistics in strong-field applications with high photon flux, such as improving the SNR in XUV-imaging via increased photon flux from high harmonic generation, improving the SNR and getting high flux in field-driven electron emission on nanostructures, reducing the processing time in imaging, and avoiding space charge effects in photoelectron spectroscopy [26-39]. It isn't difficult for low repetition rate ultrafast sources with low average power generating high intense and ultrashort pulses utilizing the OPA/OPCPA. Newly invented nonlinear crystals with low residual absorption and energy storage have allowed for high output average power from OPA/OPCPA systems. Therefore, high-repetition-rate, high-average-power OPA/OPCPA systems become possible to be realized to meet strong-field experiments. Great efforts have been done to increase the repetition rate of OPA/OPCPA systems to higher repetition-rate level [123-132]. In refs. [130,132] the repetition rate of 800 nm few-cycle μ J-level OPCPA laser systems pumped by the thin-disk laser amplifier or the fiber chirped amplifier were increased into the range from 500 kHz to 1 MHz. In ref. [123] a 100- μ J, 2- μ m OPCPA system pumped by an Innoslab amplifier at 1- μ m laser was demonstrated with a repetition rate of 100 kHz. Previously, a 3.2- μ m laser system producing 9-cycle pulses with 1.2- μ J pulse energy at a repetition

rate of 100 kHz was demonstrated [129]. Nevertheless, there is still a lack of high-repetition-rate, μ J-OPA/OPCPA, MIR laser systems with more than 100 kHz repetition rate.

Besides these benefits mentioned above, the broadband OPA/OPCPA system can also provide a way to produce ultra-short pulses at different wavelength range to satisfy different requirements. We report on a fiber-amplifier-pumped, femtosecond, 1-MHz, 2.1- μ m source generating 1- μ J pulses with excellent near-field beam profile. The system was consisted of three cascaded stages, chirped pulse DFG stage, signal amplifier stage and power amplifier stage. The chirped-pulse DFG, which is a well-established architecture for generating the passively CEP-stabilized pulses, was used for passively CEP-stable MIR (2.1 μ m) pulse generation by mixing the 1- μ m seed beam and 690-nm pump beam inside the nonlinear crystal. The broadband 690-nm pump beam was generated during the process of dispersive wave generation. With infinite 1- μ m photons, the 690-nm pump pulse can transfer its broad bandwidth to the generated 2.1- μ m pulse during the chirped-pulse DFG process. Further, we demonstrated dispersion-managed mid-infrared OPA stages. These OPA stages can roughly compress amplified pulses during the amplification process to generate 1-MHz, 1- μ J, 94.5-fs, 2.1- μ m pulses. Based on our calculation, amplified 2.1- μ m pulses can be compressed to near the calculated transform-limited pulse duration \approx 30 fs with \approx 1.5-mm thick silicon window.

4.1 SYSTEM LAYOUT OF THE 2.1- μ M OPA SYSTEM

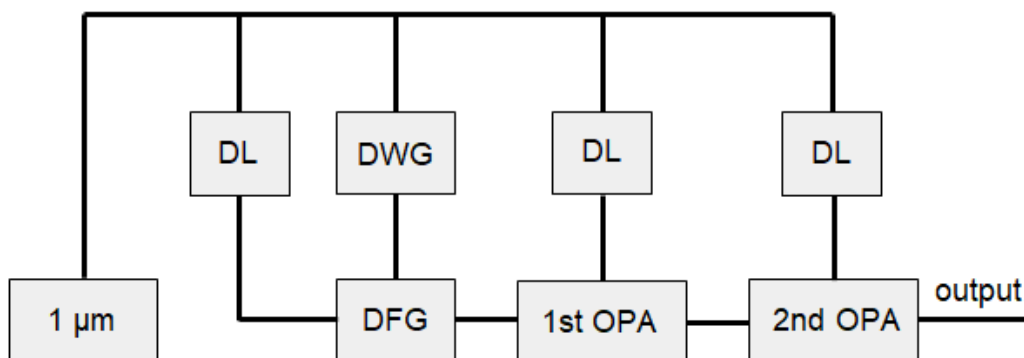


Figure 4. 1: System layout of the 2- μ m OPA system.

DWG: dispersive wave generation; DL delay line; DFG: difference frequency generation; OPA: optical parametric amplifier.

Figure 4.1 shows the system layout of the 1-MHz, 2.1- μ m system. The broadband 1-MHz, 2.1- μ m pulse was generated in the chirped-pulse DFG stage. There were the 690-

nm pump beam generated from dispersive wave generation and the 1- μ m signal beam mixing inside the nonlinear crystal to generate the 2.1- μ m idler beam. The average power of the generated 2.1- μ m beam was amplified in the 1st OPA stage from μ W level to mW level. The mW-level 2.1- μ m beam was finally amplified in the 2nd OPA stage to W level. Because the 2.1- μ m system was designed to be dispersion managed, the pulse duration of generated 2.1- μ m pulses can be roughly compressed during the parametric amplification process.

4.2 BROADBAND PASSIVELY CEP-STABLE 2.1- μ M GENERATION

As a well-established architecture, DFG enables us to fulfil requirements for generating few-cycle, passively CEP-stable, mid-infrared pulses. Amplifying generated MIR pulses in further cascaded OPA stages, we can achieve few-cycle, high-power, passively CEP-stable, MIR pulses. Methods of dispersive wave generation, chirped-pulse DFG and dispersion-managed OPA for generating the 1-MHz, high-power, few-cycle, passively CEP-stable 2- μ m laser source will be illustrated in following sections.

4.2.1 DISPERSIVE WAVE GENERATION

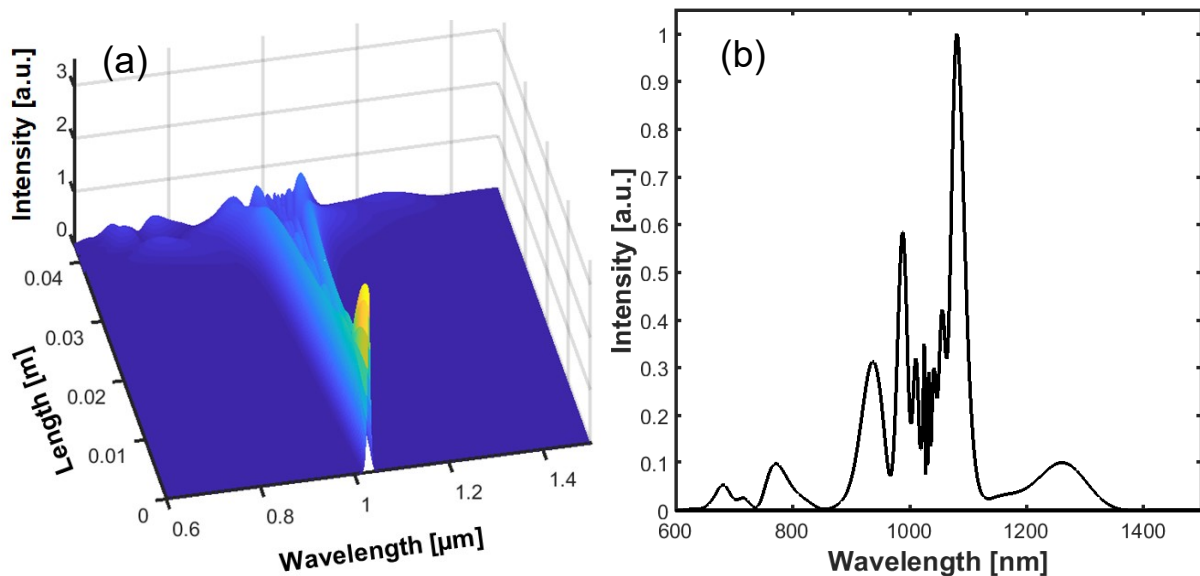


Figure 4. 2: (a) 3D Spectral evolution inside the photonic crystal fiber HNF 945; (b) The output spectrum after the 1- μ m pulse propagating through 4.3 cm distance inside the HNF 945. Calculation results for injecting 6-nJ, 250-fs, 1030-nm pulse into the HNF 945.

Aiming to generate few-cycle 2.1- μ m pulses with broadband spectrum, there has to be the phase matched pump pulse with broadband spectrum for the DFG stage. The

method of dispersive wave generation provides a sufficient way to generate the broadband pump pulse.

With the well-developed high nonlinearity PCF, ultra-broadband supercontinuum laser at infrared and visible region can be generated by using high power ultrafast laser and high nonlinearity PCF. Injecting ultrafast pulses into the PCF with sufficient peak power, there will also be the dispersive wave generation occurring in the normal GVD region of PCF after propagating enough distance during the process of supercontinuum generation [133-137]. We calculated spectral evolution of dispersive wave generation assuming a 6-nJ, 250-fs, 1030-nm pulse propagating through the 3.2-μm core diameter PCF (HNF 945, NKT) with zero GVD point at 945 nm. Caused by higher-order dispersion of PCF, the energy of generated soliton can be transferred to a narrow-band resonance in normal GVD regime of PCF, and the associated development of a low amplitude temporal pedestal [133]. The position of this resonance can be obtained from a phase-matching argument involving the soliton linear and nonlinear phase and the linear phase of a continuous wave at a different frequency.

For a generated soliton with peak power P_s at frequency ω_s , a dispersive wave is generated at frequency ω_{DW} , which works under the equation 4.2.1 with $v_{g,s}$ and the soliton group velocity at ω_s . The third term on left side of the equation explains the influence of nonlinearity and pulse peak power. Constant f_R represents the fractional contribution of instantaneous Raman response to nonlinear refractive index.

$$\beta(\omega_s) - \omega_s/v_{g,s} + (1 - f_R)\gamma P_s = \beta(\omega_{DW}) - \omega_{DW}/v_{g,s} \quad (4.2.1)$$

The generated broadband dispersive wave pulses were used to be pump pulses for chirped-pulse DFG mixing with 1-μm signal pulses to generate the broadband 2.1-μm pulses for subsequent OPA stages. In order to generate the 2.1-μm idler pulses, we need to generate the dispersive wave at 690 nm considering phase matching wavelength of the chirped-pulse DFG. Based on our calculation, if pulse energy of the input 1-μm pulse is about 6-nJ with 250-fs pulse duration, the dispersive wave at 690 nm was generated after propagating through 4.3-cm PCF (HNF 945). The 3D spectral evolution of dispersive wave generation process is shown in Figure 4.3(a). The spectrum of inputting 1-μm pulse can be broadened by SPM and Raman effects during the propagation. After accumulating enough linear and nonlinear phase, the energy of generated soliton can be transferred to the 690-nm dispersive wave, which is in the normal GVD region of PCF.

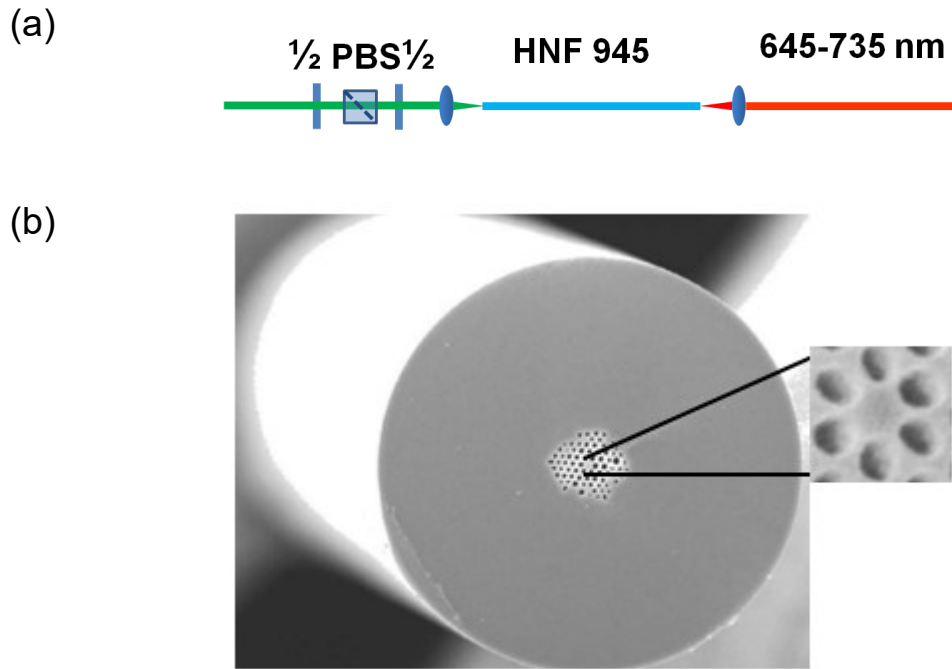


Figure 4. 3: (a) Schematic construction of the dispersive wave generation; (b) Photonic crystal fiber structure [133].

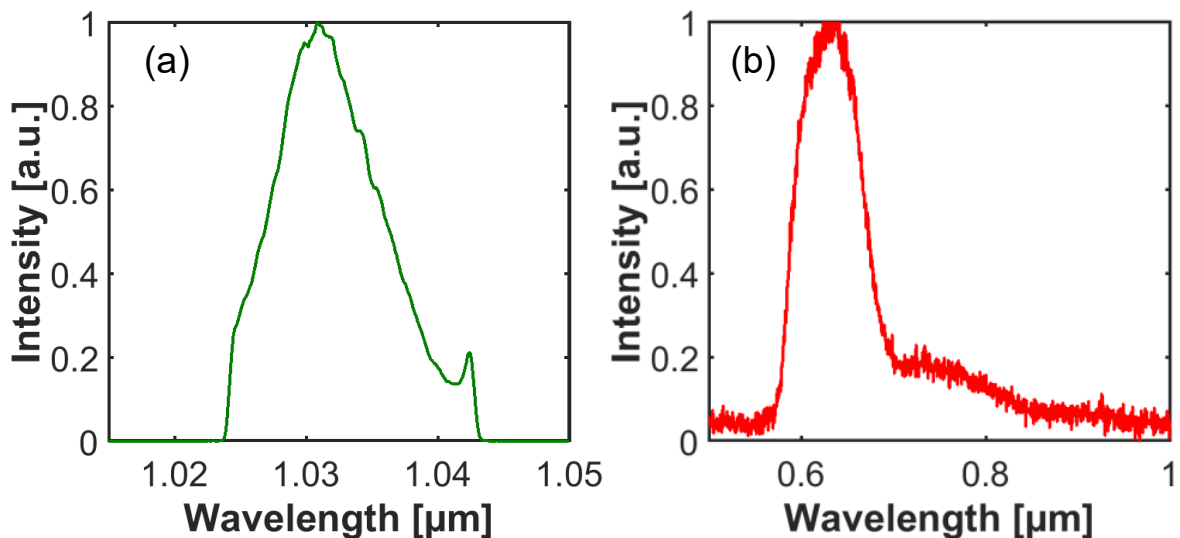


Figure 4. 4: (a) Spectrum of the 1- μ m pulse; (b) Spectrum of the generated dispersive wave.

Based on our calculation, we built the experimental setup shown in Figure 4.3 (a) to generate the 690-nm dispersive wave. The combination of half waveplates and PBS was used to modify input power and make sure that the polarization of 1- μ m input beam was parallel with the optical axis of PCF to avoid the polarization rotation inside the PCF. An 8.5-mm focal length B-coated lens was used to focus the 5-mm diameter beam into the 3.2- μ m core diameter fiber. The output beam from the fiber was collimated by a 1.5-mm

focal length B-coated lens. The output power of the linearly polarized 690-nm dispersive wave was ≈ 1 mW. Figure 4.4 shows spectra of the 1- μ m pulse and the generated 690-nm dispersive wave. The positively chirped 690-nm dispersive wave can be used to do interaction with the 1- μ m beam inside the nonlinear crystal for further chirped-pulse DFG stage.

4.2.2 THE CHIRPED PULSE DIFFERENCE FREQUENCY GENERATION

The frequency conversion process supported by second-order nonlinear coefficient $\chi^{(2)}$ is a three-wave interaction, which satisfies phase matching condition $n_3\omega_3 = n_1\omega_1 + n_2\omega_2$ [18,19]. As is shown in Fig 4.6 (a), these two input waves at frequencies ω_1 and ω_2 interact to drive a new higher-frequency output wave during the process of SFG. As is shown in Fig 4.6 (a), input waves at frequency ω_3 and ω_1 interact to drive a new frequency at ω_2 during the process of DFG. During the process of OPA / OPCPA, signal pulses and idler pulses can be amplified by pump pulses via nonlinear frequency conversion inside nonlinear crystal. These processes can be used to generate tunable femtosecond radiation in mid-infrared region. Under the slowly varying amplitude approximation and neglecting the effects such as diffraction, group-velocity mismatch, and GVD, the DFG in a lossless nonlinear crystal can be modeled by the following coupled amplitude steady-state equations (4.2.2-4.2.4).

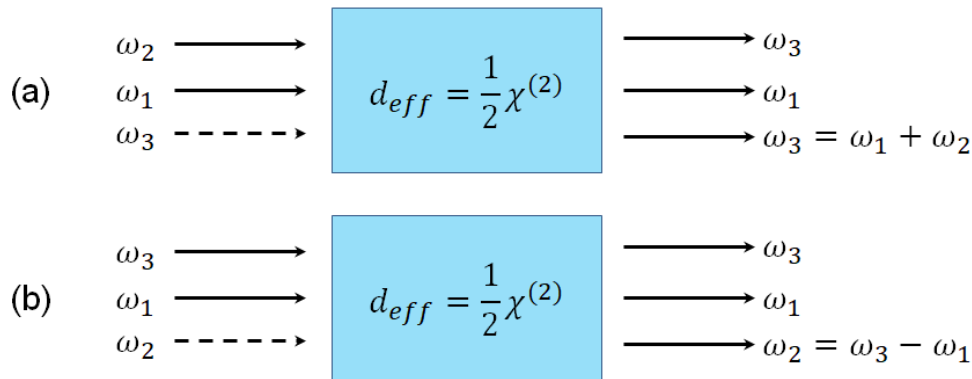


Figure 4. 5: (a) Sum frequency generation and (b) difference frequency generation.

$$\frac{d\hat{E}(\omega_1)}{dz} = -i\kappa_1\hat{E}(\omega_3)\hat{E}^*(\omega_2)e^{i\Delta kz} \quad (4.2.2)$$

$$\frac{d\hat{E}(\omega_2)}{dz} = -i\kappa_2\hat{E}(\omega_3)\hat{E}^*(\omega_1)e^{i\Delta kz} \quad (4.2.3)$$

$$\frac{d\hat{E}(\omega_3)}{dz} = -i\kappa_3\hat{E}(\omega_2)\hat{E}(\omega_1)e^{-i\Delta kz} \quad (4.2.4)$$

Here, $\kappa_i = \frac{\omega_i d_{\text{eff}}}{n_i c_0}$ and d_{eff} is the effective nonlinearity. $\Delta k = k_3 - k_1 - k_2$ represents the wave-vector mismatch, which is a scalar for the collinear arrangement of the three optical waves. Nonlinear frequency conversion becomes more efficient when the phase-matching condition is satisfied, which is $\Delta k = 0$. The most efficient way to achieve phase-matching is to utilize a birefringent nonlinear crystal, set the polarizations of the optical waves based on the relationships shown in Table 4.1 and satisfy the acceptance angle and the acceptance crystal length of the nonlinear crystal. The refractive index of the corresponding e-wave can be adjusted by tuning the incident angle of the optical beams and the crystal. If the pump beam is undepleted and only the pump beam and signal beam exist at the input, equations 4.2.2-4.2.4 can be solved analytically to the following expression equation 4.2.5, where l is the crystal thickness.

$$I(\omega_2, l) = \frac{2\kappa_2^2 n_2}{n_1 n_3 c_0 \epsilon_0} \cdot l^2 I(\omega_3) I(\omega_1) \left\{ \frac{\sin \Delta k l / 2}{\Delta k l / 2} \right\}^2 \quad (4.2.5)$$

Table 4.1: Phase matching conditions

	Positive uniaxial ($n_e > n_o$)	Negative uniaxial ($n_e < n_o$)
Type I	$n_3^o \omega_3 = n_1^e \omega_1 + n_2^e \omega_2$	$n_3^e \omega_3 = n_1^o \omega_1 + n_2^o \omega_2$
Type II	$n_3^o \omega_3 = n_1^o \omega_1 + n_2^e \omega_2$	$n_3^e \omega_3 = n_1^e \omega_1 + n_2^o \omega_2$

Based on experimental results of dispersive wave generation, incidence pulses of DFG were positively chirped making the DFG process a chirped pulse DFG process. Figure 4.6 shows the schematic construction of chirped-pulse DFG stage. ≈ 1.05 -W 1-μm beam was used as the signal beam. ≈ 1 -mW 690-nm beam was used as the pump beam. The delay line was used to achieve temporal overlap of signal pulse and pump pulse. Beam diameter of these two beams was set to ≈ 0.8 mm before being focused into the nonlinear crystal. Aiming to get enough power intensity to guarantee the nonlinear conversion efficiency, both of these two beams were tightly focused by a 35-mm thick fused silica lens to 60-μm beam diameter. The field intensity of the 690-nm pump beam was $\approx 1.1 \times 10^5$ W/cm². The field intensity of the 1-μm signal beam was $\approx 7.08 \times 10^{10}$ W/cm².

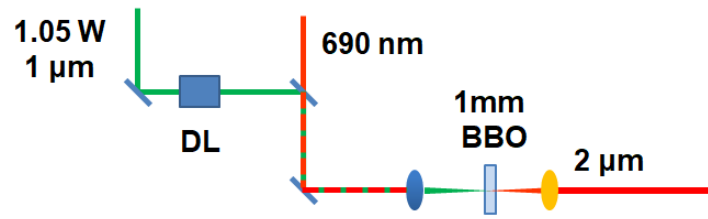


Figure 4. 6: Schematic construction of the chirped pulse difference frequency generation.

Before starting to build the chirped-pulse DFG stage, it is necessary to choose crystal with suitable crystal length and cut angle. The crystal length l is inversely proportional to the phase matching bandwidth $\Delta\lambda$. Therefore, we need to use thin nonlinear crystal to generate broadband idler pulses. Further, the phase matching angle of our chirped pulse DFG stage was $\approx 20^\circ$ based on our calculation.

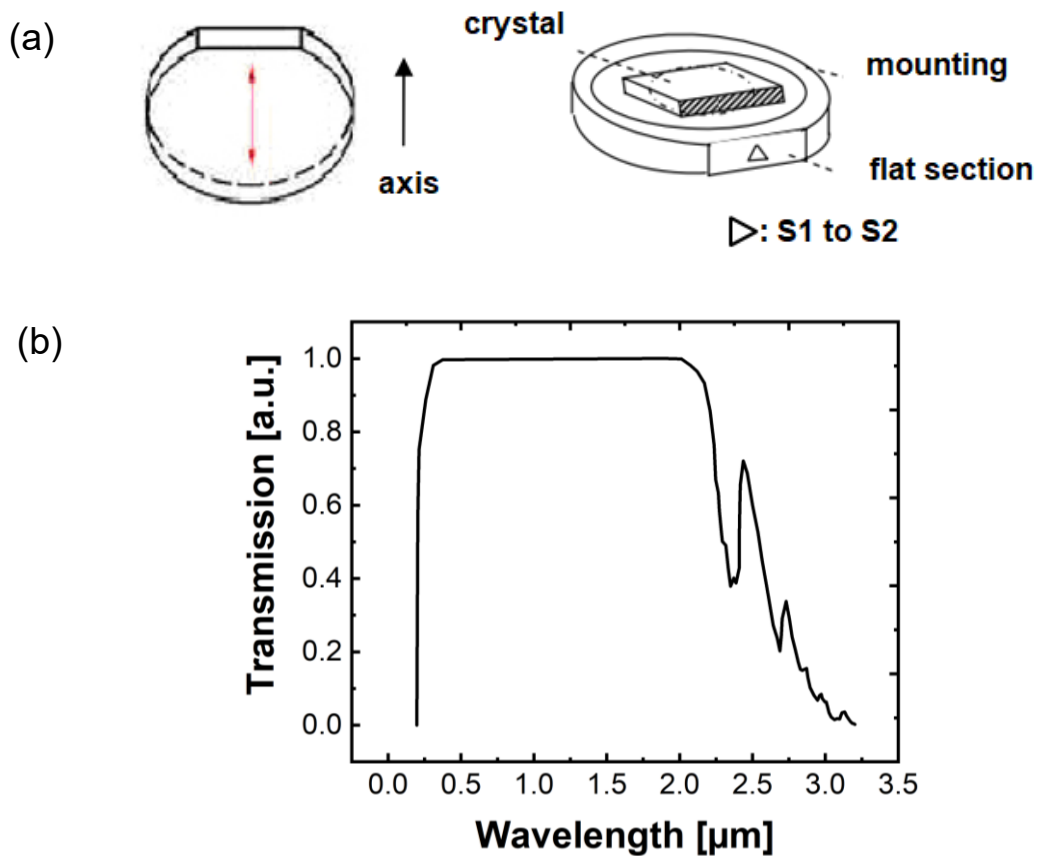


Figure 4. 7: (a) Schematic structure of the 1-mm type I BBO crystal; (b) Transmission spectrum of a 1-cm thick BBO crystal [144].

Shown in Fig 4.7 (a), we use type I BBO crystal (CASTECH, AR-coated at 700/1030nm for S1 and 2000nm for S2) to be nonlinear crystal with $\approx 20^\circ$ cut angle, which is exactly the phase matching angle for DFG process. Figure 4.7(b) shows transmission spectrum of the 1-cm thick BBO crystal. Because of the transmission limitation of material,

spectral range of generated 2- μ m spectrum should not be broader than 2.5 μ m to avoid high transmission loss.

Applying pump pulses and signal pulses with spectra shown in Figure 4.4, a broadband, 1-MHz, passively CEP-stable, 2- μ m beam was generated during the chirped-pulse DFG process. The physical mechanism of DFG process for generating passively CEP-stable pulse can be understood by considering that idler pulses were generated by interaction between pump pulses and signal pulses carrying the same CEP. In this nonlinear process, phases of these two pulses add up with opposite signs leading to CEP cancellation and generation of passively CEP-stable idler pulses based on $\nu_p - \nu_s = (n_p - n_s) \times f_R + (f_{\text{CEO}} - f_{\text{CEO}})$. Positively chirped pump pulses of chirped-pulse DFG stage were generated during the dispersive wave generation process inside 4-cm 3.2- μ m core diameter PCF (HNF 945).

A 1-mm thick type I BBO crystal was used for chirped-pulse DFG process. Besides fulfilling phase-matching condition, these two incidence beams should have perfect temporal and spatial overlap. For realizing mid-infrared laser generation, there is an efficient way using SFG with a thicker nonlinear crystal to check whether there are temporal and spatial overlaps for signal pulse and pump pulse or not. Compared with DFG process, the generated beam during SFG process is in visible wavelength region. We can easily find the generated beam by carefully measuring and adjusting temporal delay of the chirped-pulse DFG stage. Therefore, it is clear that both of these two input beams have temporal and spatial overlap inside the crystal after finding the phenomenon of SFG. There was still temporal and spatial overlap of pump pulse and signal pulse inside the nonlinear crystal after changing the thick nonlinear crystal back to the thin nonlinear crystal at the same position.

The next step for building chirped-pulse DFG stage is to fulfil the phase matching condition of the chosen nonlinear crystal. Polarization directions of the 1- μ m signal (ordinary) and the 690-nm pump beam (extraordinary) were set to fulfil the type I phase matching condition. The cut angle of the 1-mm thick BBO crystal (20.5°) was same with the calculated phase matching angle. Both of 690-nm pump beam and 1- μ m signal beam were collinearly focused into the BBO crystal by 35-mm focal length lens with normal incidence angle. With sufficient power of the 1- μ m beam, we observed the photon conversion efficiency from 690 nm to 2.1 μ m of 1 %. The spectrum of generated 2.1- μ m signal pulses with Gaussian profile is shown in Figure 4.8 (a), which matches

well with the calculated spectrum shown in Figure 4.8 (b). The spectral bandwidth of Figure 4.8 (a) was ≈ 300 nm. Output average power of generated passively CEP-stable, 2.1- μ m pulses (idler) during the process of DFG was ≈ 3 μ W. Based on calculation, the pulse duration of the generated 690-nm dispersive wave is ≈ 80 fs. The calculated transform-limited pulse duration of 690-nm pulse is ≈ 15 fs. The calculated pulse duration of generated positively chirped 2.1- μ m pulse is ≈ 192 fs. The transform-limited pulse duration of corresponding 2.1- μ m spectrum is ≈ 20 fs.

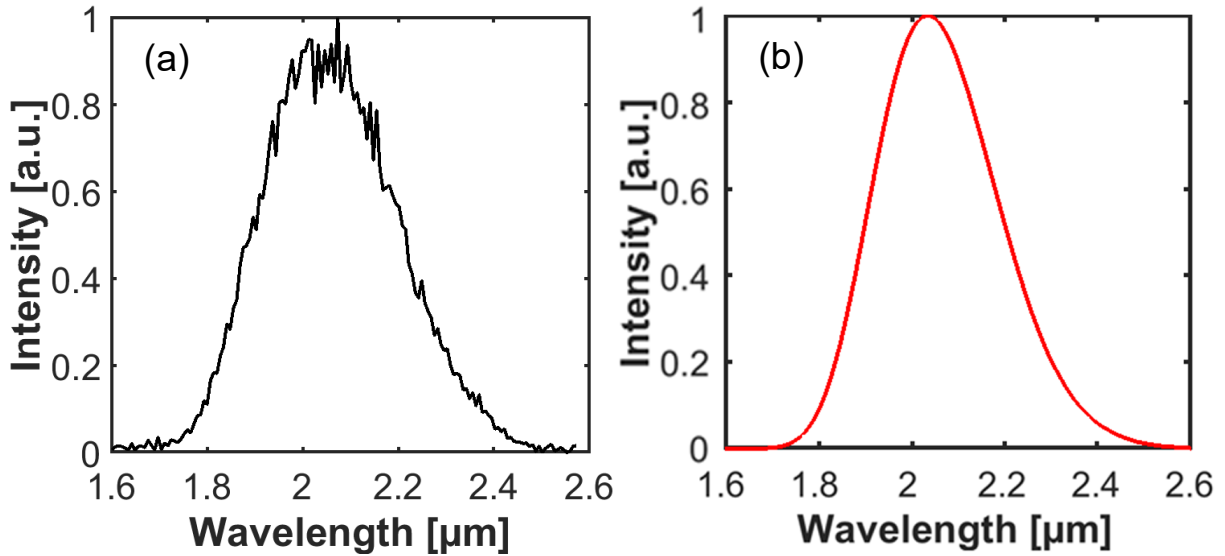


Figure 4. 8: (a) The spectrum of the generated broadband 2- μ m pulse during the chirped pulse DFG in the 1-mm thick BBO crystal; (b) Numerically calculated spectrum of the chirped pulse DFG in the 1-mm thick BBO crystal.

4.3 HIGH REPETITION RATE, μ J]-LEVEL, FEMTOSECOND, 2.1- μ M OPA SYSTEM

Obviously, the generated 2.1- μ m beam with only 3- μ W average power cannot be used as the ultrafast laser source for further strong-field experiments. Compared with other amplification methods, OPA/OPCPA provides highest gain to amplify weak signal lasers in broad wavelength range using different kinds of nonlinear crystals. The lack of energy storage and the low residual absorption of well-developed nonlinear crystals has been applied for high average output power scaling in OPA/OPCPA systems. Great efforts have been down to build high repetition rate, high average power, ultrafast sources applying the method of OPA/OPCPA for strong-field experimental applications. Based on 1-MHz, 1- μ m fiber laser, we demonstrated the 1-MHz, 1-W, few-cycle, passively CEP-stable, 2- μ m OPA system applying ≈ 23 -W 1- μ m pump power. Multi- μ J, few-cycle, 2- μ m pulses can be obtained with full 1- μ m pump power for further experiments.

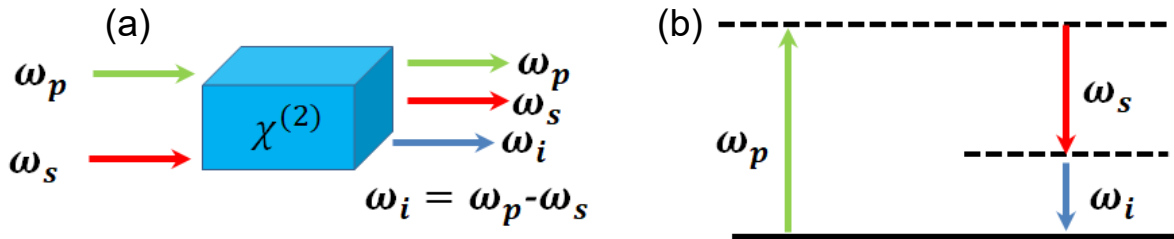


Figure 4. 9: Principle scheme of the OPA process.

The principle of OPA is illustrated in Figure 4.9 (a). After choosing the suitable nonlinear crystal, the energy is transferred from higher frequency beam (pump beam, at frequency ω_p) to lower frequency beam (signal beam at frequency ω_s and idler beam at frequency ω_i). The idler beam is generated by interaction between pump beam and signal beam inside nonlinear crystal. Shown in Figure 4.9 (b), the OPA process can be given in a corpuscular interpretation, which shows that a photon at frequency ω_p is absorbed by a virtual level of the material and a photon at frequency ω_s stimulates the emission of two photons at frequency ω_s and ω_i . The phase matching condition should also be fulfilled based on the phased matching condition discussed in section 4.2.2.

$$\Delta f = -\frac{2\sqrt{\ln 2}}{\pi} \sqrt{\frac{\Gamma}{L} \frac{1}{|v_i - v_s|}} \quad (4.3.1)$$

When group velocities of signal beam and idler beam are not the same, the FWHM parametric gain bandwidth can be described as equation 4.3.1. L is the length of the nonlinear crystal. v_i and v_s are group velocities of the idler pulse and signal pulse. $\Gamma^2 = (2d_{\text{eff}}^2 \omega_i \omega_s / c^3 \epsilon_0 n_i n_p n_s) I_p$, I_p is the pump intensity and d_{eff} is the effective nonlinear optical coefficient. If v_i is equal to v_s , the equation 4.3.1 changes into equation 4.3.2. The gain bandwidth is limited by group velocity dispersions of signal and idler pulse. Therefore, in order to achieve broadband phase matching gain bandwidth, making velocities of signal pulse and idler pulse almost the same and minimizing group velocity dispersions of the signal pulse and idler pulse are the best ways to obtain broadband gain bandwidth.

$$\Delta f = -\frac{2(\ln 2)^{1/4}}{\pi} \left(\frac{\Gamma}{L}\right)^{1/4} \frac{1}{\left| \frac{\partial^2 \omega_s}{\partial k_s^2} + \frac{\partial^2 \omega_i}{\partial k_i^2} \right|}} \quad (4.3.2)$$

Figure 4.10 shows the geometry of non-collinear interaction [125]. To obtain broadband phase matching, conditions $\partial k_i / \partial \omega_i = \cos \Omega (\partial k_s / \partial \omega_s)$ or $v_s = v_i \cos \Omega$

should be satisfied. These allow us to determine signal-idler angle Ω for broadband phase matching. From practical points of view, it is also useful to determine pump-signal angle α shown in equation 4.3.3.

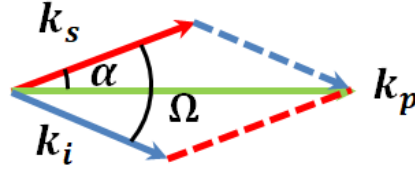


Figure 4. 10: Schematic construction of the non-collinear interaction geometry.

$$\alpha = \arcsin \left[1 - \frac{v_s^2}{v_i^2} / 1 + \frac{2v_s n_s \lambda_i}{v_i n_i \lambda_s} + \left(\frac{n_s \lambda_i}{n_i \lambda_s} \right)^2 \right] \quad (4.3.3)$$

4.3.1 SCHEMATIC CONSTRUCTION OF THE DISPERSION MANAGED 2.1- μ M OPA SYSTEM

Figure 4.11 shows the schematic construction of the 1-MHz, μ J level, 2.1- μ m OPA system consisted of 1st stage OPA as signal amplifier and 2nd stage OPA as power amplifier. Both of these two OPA stages were designed to be dispersion managed. Table 4.2 shows GVD and TOD of different materials at 2.1- μ m. Both of the MgO:PPLN crystal and the BBO crystal provide negative chirp to 2.1- μ m pulses during the amplification process to roughly compensate positively chirped 2.1- μ m pulses, which were generated from chirped-pulse DFG process. The MgO:PPLN is known to have one of the highest nonlinear coefficients, $d_{eff} = 14$ pm/V, and therefore suitable for high gain amplification, while the damage threshold is relatively low. Therefore, the MgO:PPLN crystal is an excellent choice for a high-gain OPA stage as small signal amplifier. We used BBO crystal as nonlinear crystal for the second OPA stage. The damage threshold of BBO crystal is much higher than that of MgO:PPLN crystal. BBO crystal can handle a much higher aperture size for energy and average-power scaling. Therefore, we used MgO:PPLN crystal as nonlinear crystal for signal amplifier and BBO crystal for power amplifier.

Table 4.2: Dispersion parameters of different materials

Name of material	GVD (fs^2/mm)	TOD (fs^3/mm)
MgO:PPLN	-72.54	881.509

BBO	-170.24	902
CaF2	-27.13	142.3
Silicon	766	838.5
Fused Silica	-123.1	571.1

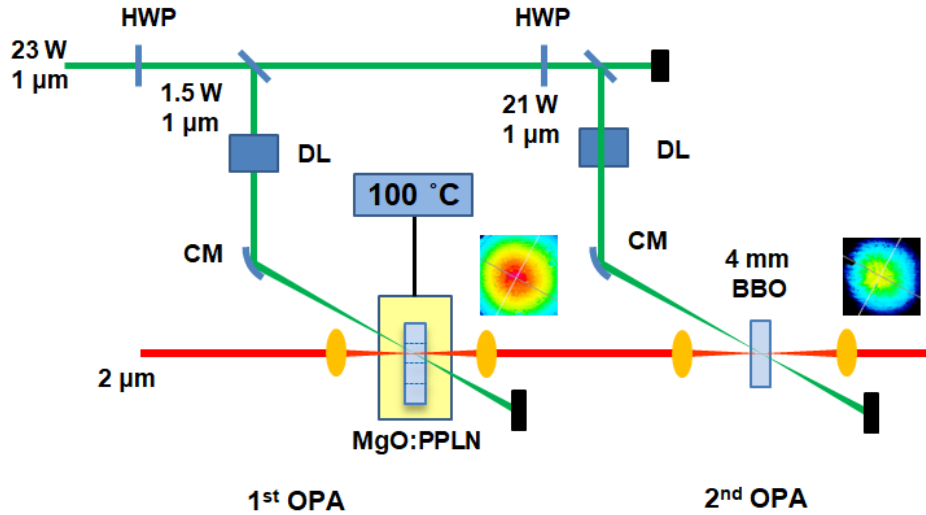


Figure 4. 11: Schematic construction of the dispersion managed 2- μ m OPA system.
DL: delay line; CM: curve mirror;

The 3-mm thick MgO:PPLN was used to build the signal amplifier to amplify 3- μ W, 1-MHz, 2.1- μ m signal beam. The beam diameter of 2.1- μ m signal beam was focused to about 100 μ m inside the crystal by a 250-mm focal length CaF2 lens. The beam diameter of 1- μ m pump beam was focused to 130 μ m inside the crystal by a 250-mm focal length curved silver mirror. The 2.1- μ m signal beam propagated through the MgO:PPLN crystal with normal incidence. Polarization directions of pump beam and signal beam were set to be parallel to z-axis of the MgO:PPLN crystal to satisfy the phase matching condition. Since signal beam and idler beam are in same wavelength region, the incidence angle difference between 1- μ m pump beam and 2.1- μ m signal beam was designed to be 1.9°, which can help us to separate the signal beam with the idler beam. Temporal overlap and spatial overlap were achieved with the help of a 12.5-GHz photodetector (EOT) and mid-infrared WinCamD (DataRay Inc.). Since the generated 2.1- μ m pulse from the DFG process was positively chirped and the pulse width of the 1- μ m pump pulse was only 245 fs, there were no more dispersive components added in the 1st OPA stage to chirp the 2.1- μ m signal laser, which helps us to avoid the bandwidth loss during the amplification process inside the MgO:PPLN crystal. About 1.5 W of the 1- μ m pump laser were used to amplify the 2.1- μ m signal laser to about 22 mW after the signal amplifier.

The pump to signal efficiency was about 1.57%. The field intensity was $\approx 2.26 \times 10^{10} \text{ W/cm}^2$ of the pump beam and $\approx 4.5 \times 10^4 \text{ W/cm}^2$ of the signal beam. A 4-mm thick BBO crystal was used to build the power amplifier to amplify the 2.1- μ m laser to the μ J level. Because this BBO crystal was cut for type I phase matching, polarization directions of the 2.1- μ m signal beam (ordinary) and the 1- μ m pump beam (extraordinary) were set to fulfil the phase matching condition. The 22-mW, 2.1- μ m signal beam diameter was mode matched to about 300 μ m inside the crystal by the 150-mm focal length CaF₂ lens and the 1- μ m pump laser beam diameter was mode matched to 350 μ m inside the crystal by a 500-mm focal length curved silver mirror. Also for separating the signal beam and the idler beam, the incidence angle difference of these two beams was 1.5°. About 21 W of the 1- μ m pump laser was used to amplify the 20 mW strong 2.1- μ m signal to about 1 W. The pump to signal efficiency was about 5%. The field intensity was $\approx 6.5 \times 10^8 \text{ W/cm}^2$ of the pump beam and $\approx 8.43 \times 10^5 \text{ W/cm}^2$ of the signal beam.

4.3.2 SIGNAL AMPLIFIER OF THE 2- μ M SIGNAL PULSES

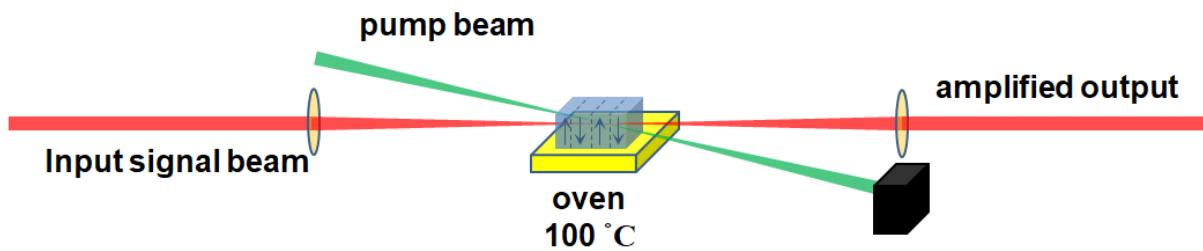


Figure 4. 12: Construction layout of the 1st OPA stage.

Figure 4.12 illustrates the construction layout of the 1st OPA stage. The signal beam has normal incidence angle. The pump beam has a 1.9 degree incidence angle difference with the signal beam. Therefore, the generated 2.1- μ m idler beam and 2.1- μ m signal beam can be spatially separated with each other after propagating for certain distance (10 cm or more). The residual pump was blocked by a beam dump. Before using the MgO:PPLN crystal to build signal amplifier, it needs to be confirmed that the poling period and the transmission window of the MgO:PPLN crystal are correct for phase matching condition and avoiding the transmission loss. Shown in Figure 4.13 (a), we can find the phase matching poling period for 2.1- μ m laser is in the range of 31-32 μ m. Shown in Figure 4.13 (b), MgO:PPLN crystal is transparent to 2- μ m laser. The damage threshold of the nonlinear crystal is another important parameter [138,139], which can

play an important role in high power amplification. We measured the damage threshold of MgO:PPLN crystal with our 1- μ m laser source, which was ≈ 2 - μ J, 250-fs pulses with 130- μ m beam diameter corresponding to $\approx 3 \times 10^{10}$ W/cm² field intensity at 100 °C.

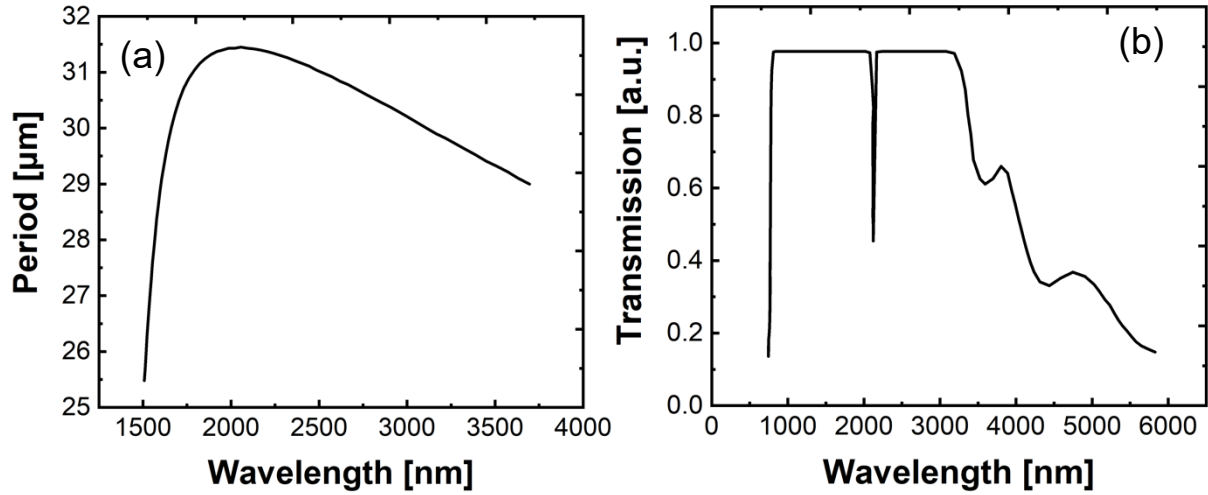


Figure 4. 13: (a) Phase matching poling period for 2.1- μ m laser inside the MgO:PPLN crystal working under 100 degree; (b) Transmission curve of the MgO:PPLN crystal [145].

Based on the calculation for achieving optimum frequency efficiency and maximum spectrum bandwidth after amplification [131], we kept the positive chirp of the 192-fs 2.1- μ m signal pulse generated from chirped-pulse DFG stage. Figure 4.14 shows spectra of the 2- μ m signal pulse (red curve), the 2- μ m amplified pulse (black curve) and the superfluorescence spectrum of the MgO:PPLN crystal after blocking the 2.1- μ m seed at 2-W pump power (blue dashed curve). Comparing these three curves, we can see significant bandwidth loss after 1st OPA stage. Based on the superfluorescence spectrum, the bandwidth loss was mainly caused by the gain bandwidth limitation of the 3-mm thick MgO:PPLN crystal. Those two spectral gaps of the superfluorescence spectrum led to spectral gaps of the amplified 2.1- μ m spectrum. This spectral construction can be caused by the phase mismatch inside of the MgO:PPLN crystal caused by different incident angles of pump beam and signal beam. The 3- μ W 2- μ m signal pulse was finally amplified to about 20 mW by the 1st stage OPA.

Figure 4.15 shows the ratio curve of 2- μ m signal beam average power versus 1- μ m pump average power. The pump power to signal power efficiency was about 1.57%. The critical power of damage threshold for MgO:PPLN crystal limited the maximum average power of amplified 2- μ m signal beam based on our experimental condition. Inset picture

of Figure 4.15 shows near-field beam profile of amplified 2- μ m signal beam, which shows that the amplified 2- μ m beam after 1st OPA stage has a perfect beam profile.

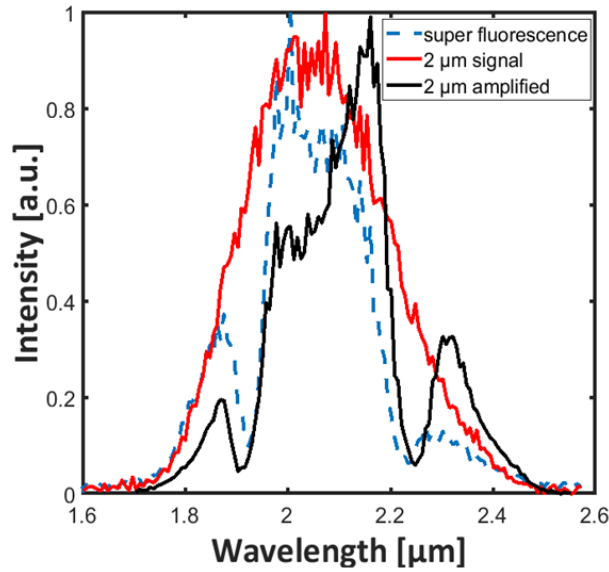


Figure 4. 14: Spectrum of the 2- μ m signal pulse (red curve) of the 1st stage OPA, spectrum of the 2- μ m amplified pulse after the 1st stage OPA (black curve), the superfluorescence spectrum of PPLN OPA after blocking the 2.1 μ m seed at 2 W pump power.

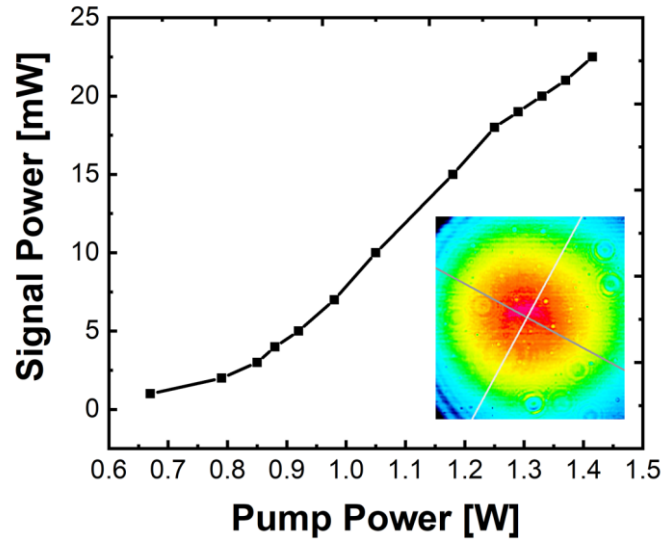


Figure 4. 15: Signal power versus pump power. Inset shows beam profile of the output signal beam.

4.3.3 POWER AMPLIFIER FOR THE 2- μ M SIGNAL PULSES

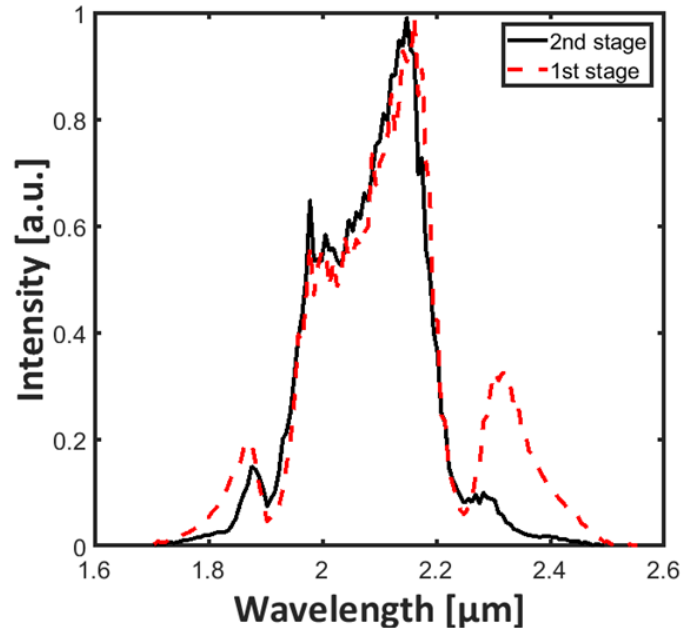


Figure 4. 16: Spectrum of the 2- μ m signal pulse (red dashed curve) of the 2nd stage OPA, spectrum of the 2- μ m amplified pulse after the 2nd stage OPA (black curve)

Figure 4.16 shows the spectra of amplified 2- μ m signal pulse after 2nd OPA stage (black curve) and signal pulse before 2nd OPA stage (red dashed curve). Based on the phase matching condition shown in table 4.1, polarization directions of the 2.1- μ m signal beam (ordinary) and the 1- μ m pump beam (extraordinary) were set to fulfil the phase matching condition. The phase matching angle of type I BBO crystal is 21.3°. The cut angle of our BBO crystal was 26°. Therefore, we tilted $\approx 5^\circ$ to match with phase matching angle. The thickness of type I BBO crystal was 4 mm. The bandwidth loss was caused by transmission loss of BBO crystal shown in Figure 4.7 (b) and phase matching bandwidth limitation for thicker nonlinear crystal.

Figure 4.17 shows the curve of 2.1- μ m signal beam average power versus 1- μ m pump power. After amplifying average power of 2.1- μ m signal beam to ≈ 1 W with 21-W pump power, the pump to signal conversion efficiency was $\approx 5\%$. Further amplification by increasing 1- μ m pump power can cause self-focusing effect leading to damages of BBO crystal. The pulse energy of amplified 2- μ m pulse can be scaled up to mult- μ J level by increasing the pump beam diameter and signal beam diameter inside the BBO crystal. Inset picture shows near-field beam profile of the final amplified 2- μ m beam.

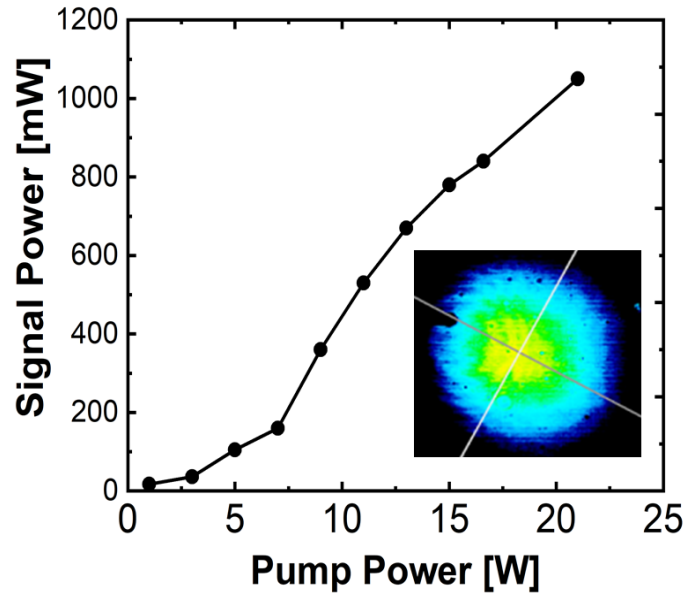


Figure 4. 17: Signal power versus pump power. Inset shows near-field beam profile of the output signal beam.

The GVD of Mg:PPLN crystal at 2.1 μ m is $-72.54 \text{ fs}^2/\text{mm}$, and its TOD is $881.509 \text{ fs}^3/\text{mm}$. The GVD of BBO crystal at 2.1 μ m is $-170.24 \text{ fs}^2/\text{mm}$, and its TOD is $902 \text{ fs}^3/\text{mm}$. Since the generated 2.1- μ m signal beam was positively chirped during the chirped pulse DFG process, the signal pulse was roughly compressed during the amplification process, which makes it a dispersion managed process. To further characterize the amplified, 2.1- μ m pulse, we built the interferometric auto-correlator shown in Figure 4.18 to measure the interferometric auto-correlation trace of the 2.1- μ m pulse. Combination of two pin holes and an alignment laser was used to help to align free-space optics of the interferometric auto-correlator. A short-pass filter was inserted after BBO crystal to get rid of noise signal caused by the residual fundamental frequency. Figure 4.19 shows measured interferometric auto-correlation (IAC) trace (red curve) of the final output 2.1- μ m pulse and the calculated IAC trace (blue curve) when fitting the IAC of a linearly chirped pulse with the measured 2- μ m spectrum shown in Figure 4.16 to the measured IAC. From this measurement and fitting, we can infer that the output pulse has a width of 94.5 fs with -1200 fs^2 GDD. The pulse can be compressed to near its transform limit of 24 fs when removing the chirp by propagation through a ≈ 1.5 mm thick Si window. Even without full compression, we generated 94.5-fs, 1- μ J, 1-MHz pulses with excellent beam profile shown in Figure 4.18, well-suited for many applications requiring for high-power, high-repetition-rate, few-cycle MIR pulses.

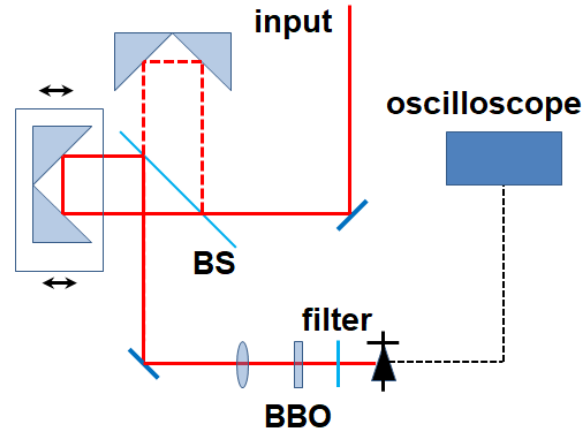


Figure 4. 18: Schematic construction of the home-built interferometric auto-correlator.

BS: beam splitter; BBO: beta barium borate;

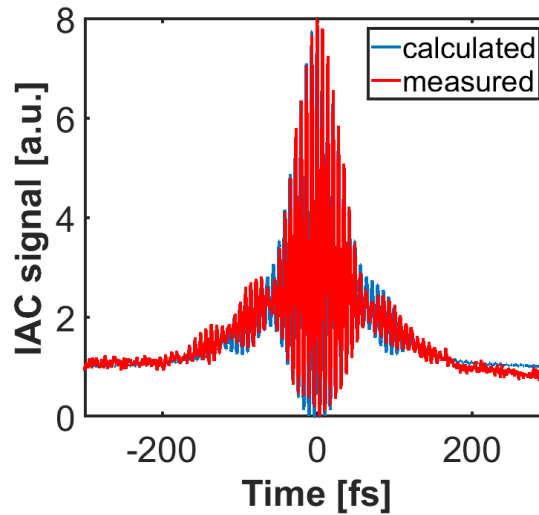


Figure 4. 19: The calculated transform-limited IAC trace (blue curve) based on the output spectrum and the measured IAC trace (red curve) of the output pulses without compression.

We did the calculation by adding different dispersion to fit the measured IAC trace to get further understanding about relationships between dispersion and IAC trace profile. Shown in Figure 4.20, we modified the added GDD from 0 fs^2 to -1800 fs^2 with the same $+10000 \text{ fs}^3$ TOD. As the GDD increased, pedestals of the calculated IAC trace grew up rapidly and got the perfect fitting when the GDD was -1200 fs^2 . Furthermore, Figure 4.21 shows the fitting results of adding (a) -1200 fs^2 , $+10000 \text{ fs}^3$ and (b) -1200 fs^2 , 0 fs^3 to the calculated IAC trace to fit the measured IAC trace. Calculated fitting results illustrate that (a) shows a better fitting results than (b). This result also indicates that changing TOD doesn't have significant influences on IAC trace.

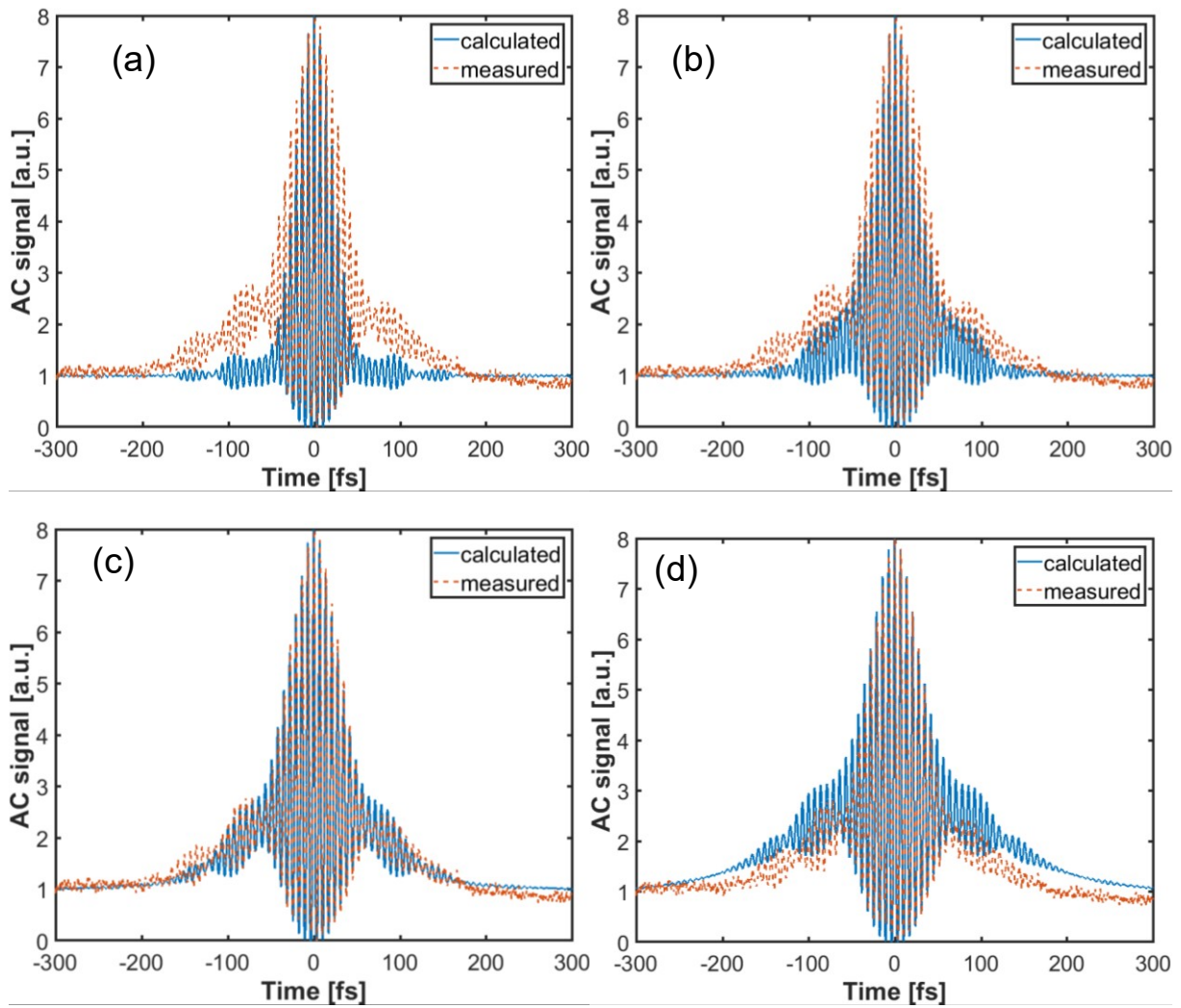


Figure 4. 20: Calculation results by adding GDD and 10000 fs^3 to fit the measured results, (a) 0 fs^2 , (b) -600 fs^2 , (c) -1200 fs^2 , (d) -1800 fs^2 .

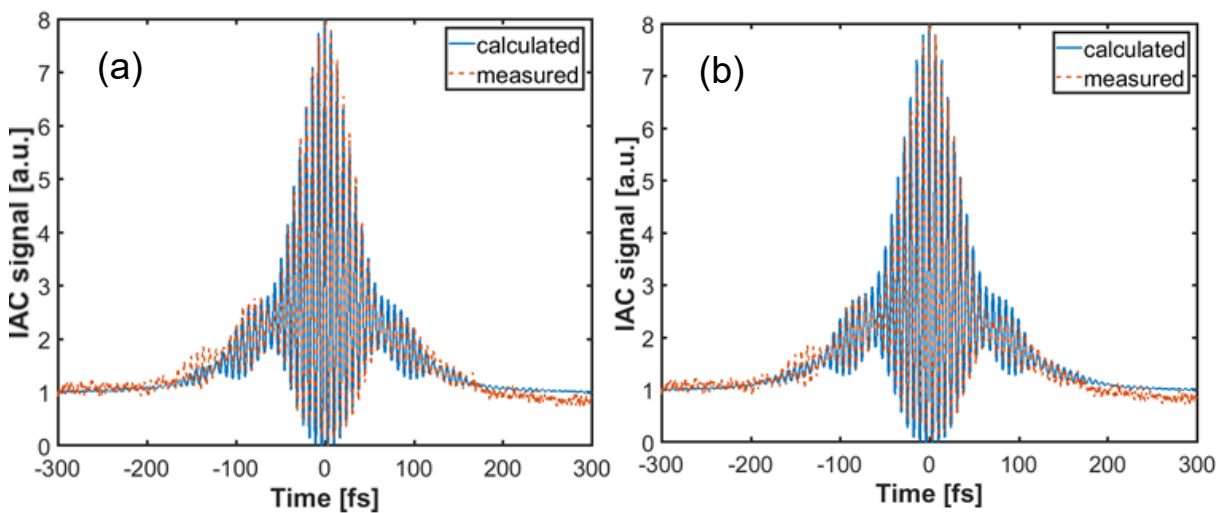


Figure 4. 21: Calculation results by (a) adding -1200 fs^2 GDD and 10000 fs^3 and (b) adding -1200 fs^2 GDD and 0 fs^3 to fit measured results.

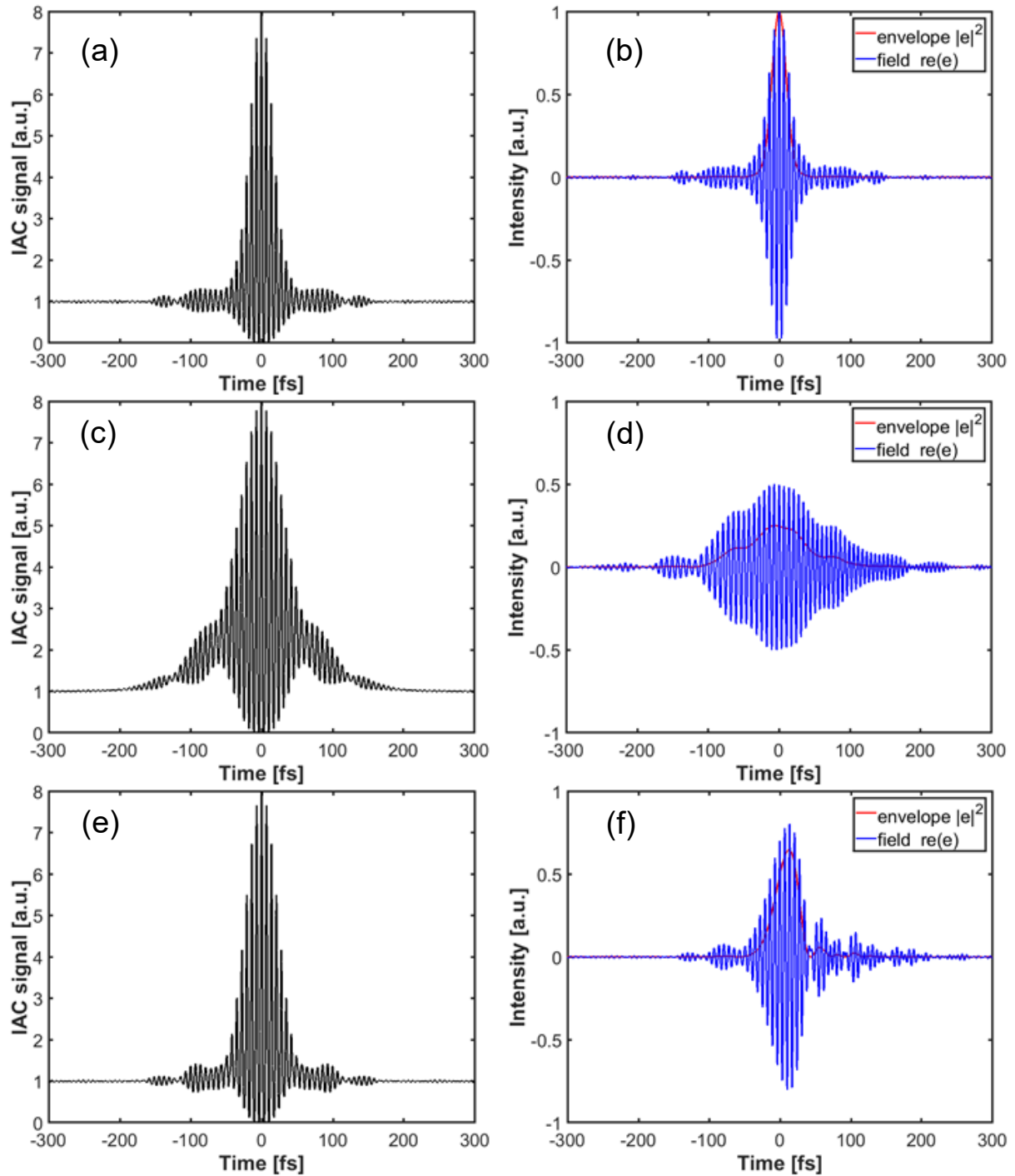


Figure 4. 22: Calculation results of (a), (b) transform-limited IAC trace and electronic field of the pulse; (c), (d) adding -1200 fs^2 and 0 fs^3 to the calculation; (e), (f) adding 0 fs^2 and 10000 fs^3 to the calculation.

Shown in Figure 4.22, the TOD mostly influences the symmetry of the pulse electronic field and the GDD significantly influenced the height of pedestals.

4.4 SCHEMATIC LAYOUT OF THE 2- μ M SYSTEM

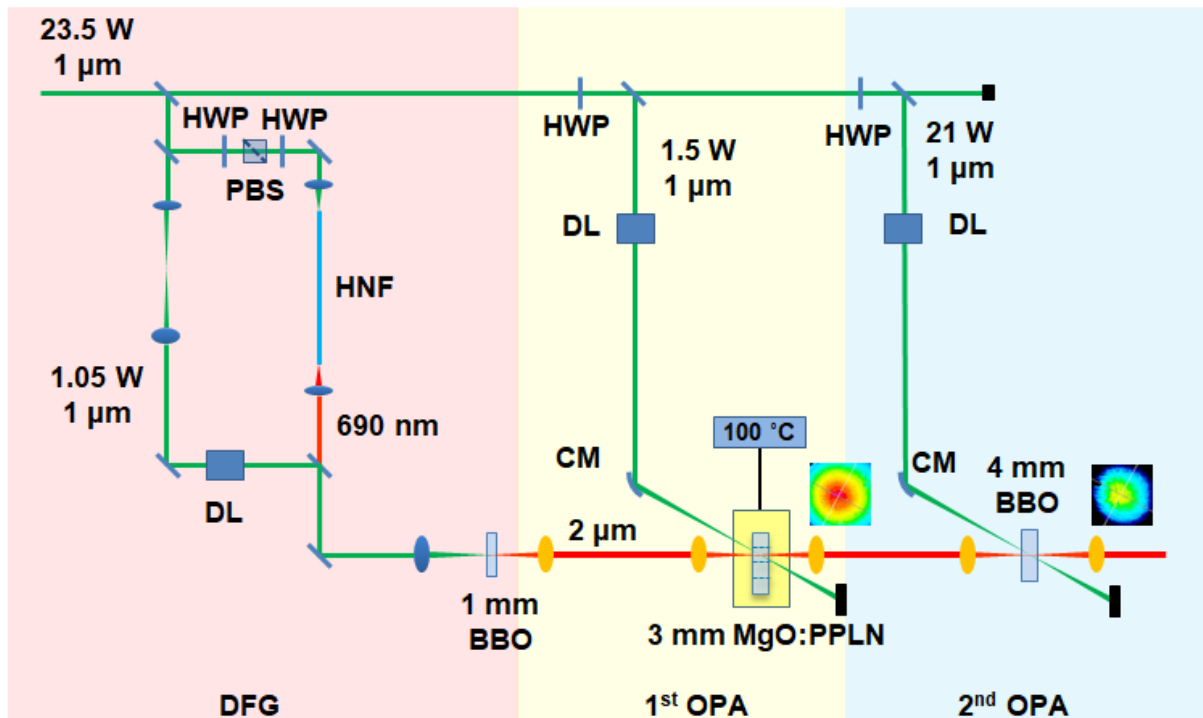


Figure 4. 23: Schematic Layout of the overall passively CEP-stable, 1-MHz, μ J-level, 2- μ m system.

Figure 4.23 shows the schematic construction of passively CEP-stable, 1-MHz, μ J-level, 2- μ m system. The signal pulse for dispersion managed OPA system was generated in chirped-pulse DFG stage. The 690-nm pump beam for chirped-pulse DFG stage was generated during the process of dispersive wave generation. The average power of generated 2- μ m signal beam was $\approx 3 \mu$ W. The 1st stage OPA was built as signal amplifier with a 3 mm thick MgO:PPLN crystal working at 100 °C. The 3- μ W signal beam was amplified to about 20 mW by the 1st OPA stage. The 2nd OPA stage was built as power amplifier with a 4 mm thick type I BBO crystal. The 20-mW signal beam was amplified to ≈ 1 W with about 21-W 1- μ m pump beam in the 2nd OPA stage. Further amplification can be achieved by increasing the pump beam diameter and signal beam diameter inside the nonlinear crystal helping us to inject more pump power, avoid damaging the nonlinear crystal and get higher amplified output power.

4.5 CONCLUSIONS

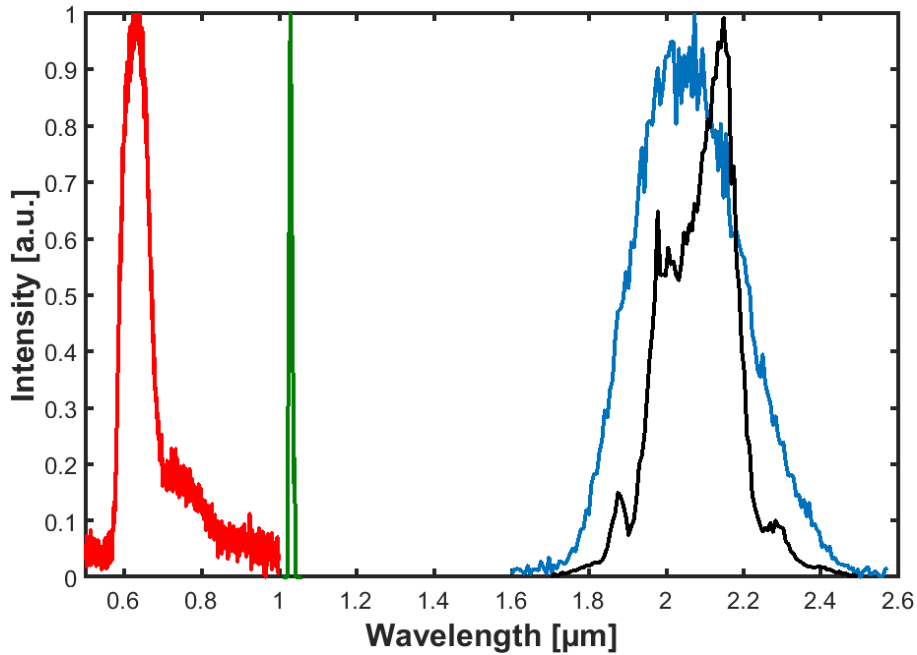


Figure 4. 24: Full wavelength range spectrum includes the 690 nm dispersive wave (red curve), 1035 nm pump laser (green curve), 2.1- μ m signal laser (blue curve) and 2.1- μ m output laser (black curve).

We demonstrate a μ J-level, 94.5-fs, 1-MHz, passively CEP-stable, 2.1- μ m dispersion managed OPA system. Compared with other amplification methods, OPA doesn't have problems in gain bandwidth limitation and small signal amplification. We realized nonlinear wavelength conversion from 700 nm to 2.1 μ m via DFG process. We finally amplified the generated 2.1- μ m pulse with the 1- μ m pump pulse. Spectra of amplified 2.1- μ m signal pulse after the 2nd OPA stage (black curve), generated 2.1- μ m signal pulses from chirped-pulse DFG (blue curve), 690-nm dispersive wave (red curve) and 1- μ m pump pulse from fiber front-end (green curve) is shown in Fig 4.24. Based on our calculation, we can compensate the GDD of the amplified 2- μ m pulse by using \approx 1.5-mm thick Si window to compress it to near transform-limited pulse duration in further experiments. Besides using this 2.1- μ m source to generate few-cycle 6- μ m pulses for further OPA experimental investigation, we also plan to use this 94.5-fs, 1-MHz, 1-W, passively CEP-stable, 2.1- μ m laser source to do further strong-field experiments, such as field-driven electron emission on nanostructures, solid-state HHG and light-matter interaction in graphene.

CHAPTER 5: CONCLUSION AND OUTLOOK

High power, high repetition rate, ultrafast sources have experienced rapid developments to satisfy applications for past decades. Applying the stretched pulse mode-locking scheme, we built the home-made stable fiber oscillator to generate a mode-locking seed beam. The repetition rate of the oscillator was set to be below 30 MHz to avoid satellites pulses generating in repetition rate decrease module, which was built with <10 ns raising time AOM. An efficient fiber stretcher was built to stretch pulses from ps-level to sub-ns-level to make sure there are no nonlinear effects generating inside fiber systems. A single-mode fiber amplifier was inserted into the stretcher to compensate for 10-dB insertion loss of all-fiber stretcher. Fiber pre-amplifiers were built to amplify stretched seed pulses to compensate insertion loss of the AOM module. Three stages of fiber signal-amplifiers were built to amplify the seed beam to the Watt level after the AOM module to make sure the seed beam can be amplified in the rod-type fiber amplifier. The rod-type fiber amplifier was used to amplify the seed beam from Watt level to about 100-W with perfect Gaussian beam profile. With the method of CPA, pulse duration of amplified pulses was compressed to about 250 fs. With the method of CP-PCMA, pulse duration of amplified seed have been compressed to about 40 fs.

Based on the 1-MHz, 250-fs, all-fiber, 1- μm source, we managed to demonstrate the 1-MHz, passively CEP-stable, μJ -level, 2- μm OPA system. Applying the method of dispersive wave generation, we managed to generate broadband dispersive wave centered at 690 nm to be the pump beam for chirped-pulse DFG. ≈ 1 -W, 1- μm beam was used as the signal beam during the chirped-pulse DFG process to make sure there was sufficient photon transaction from 690 nm to 2 μm . The average power of the generated

broadband, passively CEP-stable, 2- μm pulses was about 3 μW . The generated 2- μm was positively chirped during the chirped pulse DFG process. Based on our dispersion management, the next two stages of OPAs were designed to be dispersion managed OPA to roughly compensate for the dispersion of the 2- μm seed pulse. The seed beam was amplified to above 1 W at 94.5 fs with about 20-W 1- μm pump power. Further compression can be achieved by simply inserting the 1.2-mm silicon window. Furthermore, since there was about 25-W pump power left, we can also keep amplifying the seed beam to multi- μJ -level by making the beam diameter inside the nonlinear crystal larger and increasing the pump power. Further improvement of laser systems and further applications will be introduced in the following pages.

5.1 FURTHER IMPROVEMENT AND APPLICATIONS OF THE 1- μM SYSTEM

The development of large core diameter ytterbium-doped PCF makes it possible to use fiber amplifiers to amplify beams to high average output power. Based on the method of CP-PCMA and CPA, we demonstrated the 100-W, 40-fs, 24-MHz, 1- μm fiber laser system and the >55-W, 250-fs, 1-MHz, 1- μm all fiber laser system introduced in chapter 2 and chapter 3. Both of these two laser systems can be already used as laser sources for further strong-field experiments or mid-infrared generation.

Further amplification with the fiber amplifier can be done by applying DPA to optimize the rod-type fiber amplifier stage for the CP-PCMA system. We can divide a pulse by controlling its polarization with the divider designed based on PBS [140] or birefringent crystal [141-143] shown in Figure 5.1. Based on the same construction shown in Figure 5.1(a), [40] got the result of generating 1 kW amplified 1- μm beam by dividing the input pulse into 8 replicas and amplifying these 8 replicas in 8 rod-type fiber amplifier channels. The intensity for different replicas should be modified to achieve the same gain inside the gain fiber. Active control needs to be added into the DPA system to improve the recombining stability of the system. Applying the method of using the birefringent crystal shown in Figure 5.1 (b), all these split replicas by the birefringent crystal can be recombined passively after the amplification to avoid using the active feedback module and improve the system stability. By dividing the input pulse into 2, 4 or 8 replicas, the final output average power can be 2, 4 or 8 times higher than before.

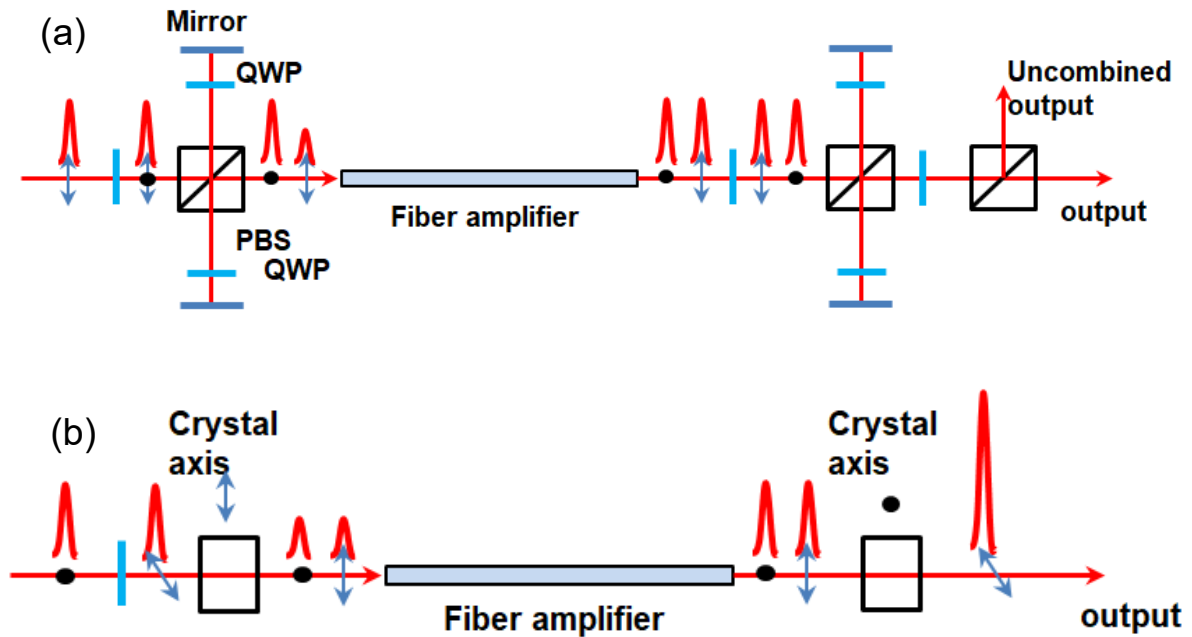


Figure 5. 1: Schematic construction of DPA with the method of dividing the seed pulses with (a) PBS and (b) birefringent crystal.

For the >55-W, 1- μm CPA system, the output average power can be amplified to >100 W when the working temperature of the pump diode is 38 degree. The working temperature of the 250-W multimode diode was 25 degrees when there was only >55 W output power. The 25 degree pump diode working temperature can't shift the center wavelength of the pump laser to its optimal wavelength for amplification leading to lower amplification efficiency. The optimal working temperature was 38 degree to shift the center wavelength of the pump laser to 976 nm to guarantee better amplification efficiency.

The pulse width of the compressed pulse from the 1- μm CPA system was 250 fs. It might be too long to achieve the designed experimental results for further strong-field experiments. Therefore, the nonlinear compression module will be necessary for scientists to achieve pulses with few-cycle pulse duration. The spectrum can be broadened by the SPM effect propagating through the hollow core fiber filled with a noble gas. This means the corresponding transform-limited pulse duration can be few-cycle level after being compressed by dispersion compensation elements. The amplified pulse can be compressed from 250 fs to single-cycle level with the method of nonlinear compression.

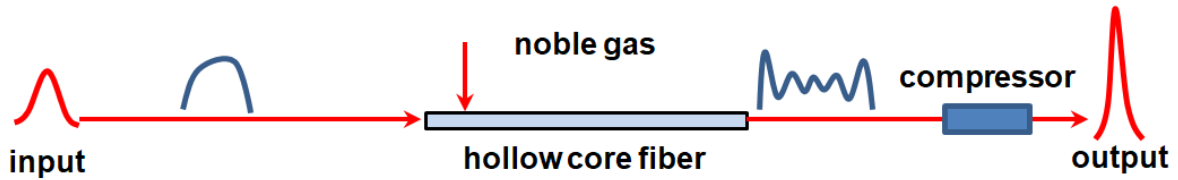


Figure 5. 2: Schematic construction of nonlinear compression with hollow core fiber.

These 1- μm sources can not only be used to generate the mid-infrared lasers via DFG and OPA/OPCPA but also be used as the source for HHG and microscopy experiments. The investigation results for doing HHG with high repetition rate and high power 1- μm sources were shown in Table 5.1. We can do the prediction that with our high power laser source we can generate the 23-25th harmonic (30-50 nm) with about 10^{13} photons/s level photon flux.

Table 5.1: Summary of the HHG laser sources

Pulse Parameters	HHG parameters
0.1-1 MHz, 30-100 μJ , 270 fs [11]	30-70 nm, 3×10^{11} photons/s (estimated)
50 kHz, 400 μJ , 800 fs [12]	24-50 nm, 0.3-3 nW, 6.8×10^7 - 6.1×10^8 photons/s
50 kHz, 200 μJ , 51 fs [12]	22-55 nm, 1-10 nW, 2.3×10^8 - 2.3×10^9 photons/s
20.8 MHz, 1 μJ , 35 fs [13]	60-90 nm, 1 nW in the 15th harmonic order
0.6 MHz, 130-150 μJ , 30 fs [14]	30-50 nm, 143 μW , 3×10^{13} photons/s for 25th harmonic (41nm)
10.7 MHz, 7 μJ , 31 fs [15]	35-55 nm, 51 μW , 10^{13} photons/s for 23th harmonic (45 nm)

5.2 FURTHER IMPROVEMENT AND APPLICATIONS OF THE 2.1- μM SYSTEM

Introduced in chapter 4, we demonstrated the 1-MHz, μJ -level, passively CEP-stable, 94.5-fs, 2.1- μm system applying methods of dispersive wave generation, chirped-pulse DFG and dispersion managed OPA. This μJ -level, 2.1- μm pulse can be further compressed to near its transform-limited pulse duration (≈ 24 fs) by simply inserting a 1.5-mm thick silicon window. Further optimization in amplifying the 2.1- μm pulse to multi- μJ can be done by increasing the pump power and enlarging the beam diameter inside the nonlinear crystal. We will have the sub 30-fs, multi- μJ , passively CEP-stable, 1-MHz, 2.1- μm beam for further experiments after achieving these improvements.

As is shown in Figure 5.3, this <30-fs, passively CEP-stable, 1-MHz, 2.1- μm OPA source can be used as the laser source for further studying the antiresonance-like

behaviour carrier-envelope-phase-sensitive optical-field electron emission, which is generated from plasmonic nanoantennas [35]. $\approx 5\text{-mW}$, $2.1\text{-}\mu\text{m}$ beam can be split from the output beam to fulfil the requirements of the field-driven electron emission experiments with >30 enhancement index. The rest of the total output power can be used to do longer wavelength MIR generation.

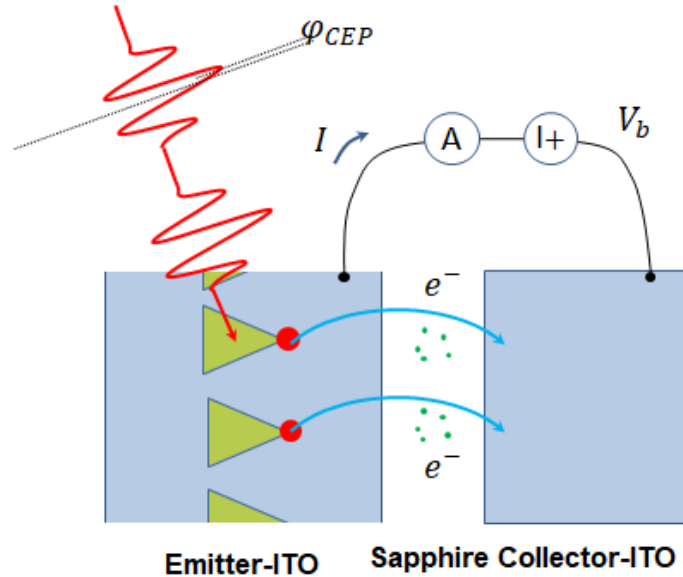


Figure 5. 3: Schematic illustration showing optical excitation and charge extraction from the nanoantenna array in the experimental setup.

The ponderomotive potential scales with the wavelength squared and the Keldysh parameter becomes smaller for longer wavelength at the same laser intensity. Further experiments should be done to generate few-cycle, passively CEP-stable, mid-infrared pulses in the longer wavelength range around $6\ \mu\text{m}$. Figure 5.4 shows the schematic construction of the passively-CEP stable, few-cycle, $6\text{-}\mu\text{m}$ generation. The $2.5\text{-}3\text{-}\mu\text{m}$ signal beam can be generated from the white light generation inside the high nonlinearity fiber at $2.1\ \mu\text{m}$ [10]. nJ-level, 1-MHz, passively CEP-stable, few-cycle, $6\text{-}\mu\text{m}$ idler pulses can be generated from the DFG process inside a $0.5\ \text{mm}$ thick zinc germanium phosphide (ZGP) crystal using $\mu\text{-J}$ level, $2.1\text{-}\mu\text{m}$ pulses as pump pulses and generated $2.5\text{-}3\ \mu\text{m}$ pulses as signal pulses. Generated nJ-level, $6\text{-}\mu\text{m}$ pulses can be used as the light source for further field-driven electron emission experiments on nanostructures and also for other MIR strong-field experiments.

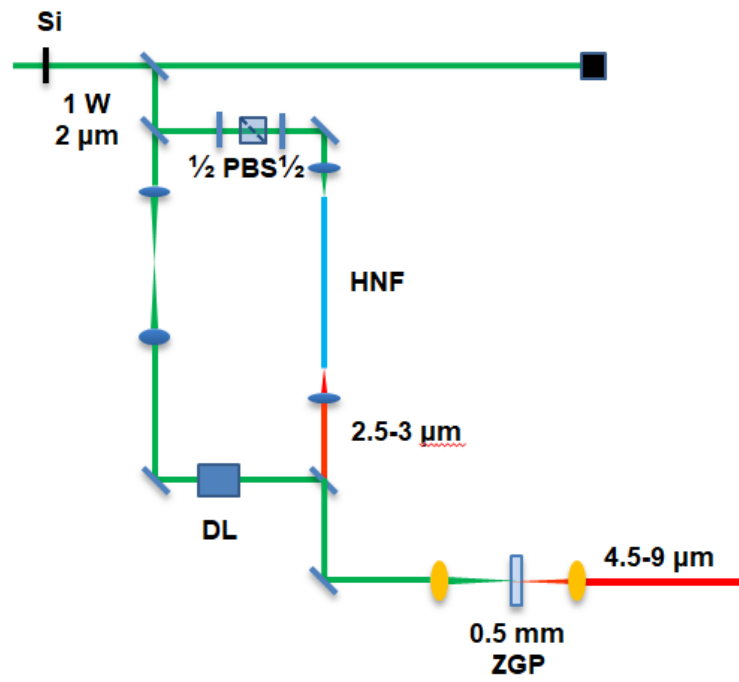


Figure 5. 4: Schematic construction of 6-μm generation.

BIBLIOGRAPHY

- [1] T. H. Maiman, "Stimulated optical radiation in ruby," *Nat.* 187, 493-494, 1960.
- [2] A. Javan, W. R. Bennett, Jr., and D. R. Herriott, "Population Inversion and Continuous Optical Maser Oscillation in a Gas Discharge Containing a He-Ne Mixture," *Phys. Rev. Lett.* 6(3), 106-110, 1961.
- [3] G. A. Mourou, T. Tajima, and S. V. Bulanov, "Optics in the relativistic regime," *Rev. Mod. Phys.* 78 (2), 309, 2006.
- [4] G. Steinmeyer, D. H. Sutter, L. Gallmann, N. Matuschek, U. Keller, "Frontiers in ultrashort pulse generation pushing the limits in linear and nonlinear optics," *Sci.* 286 (5444), 1507-1512, 1999.
- [5] S. Backus, C. G. Durfee III, M. M. Murnane, and H. C. Kapteyn, "High power ultrafast lasers," *Rev. Sci. Instrum.* 69 (3), 1207-1223, 1998.
- [6] S. Hädrich, J. Rothhardt, M. Krebs, S. Demmler, A. Klenke, A. Tünnermann, and J. Limpert, "Single-pass high harmonic generation at high repetition rate and photon flux," *J. Phys. B: At. Mol. Opt. Phys.* 49 (17), 172002-172028, 2016.
- [7] L. E. Myers, R. C. Eckardt, M. M. Fejer, and R. L. Byer, "Quasi-phase-matched optical parametric oscillators in bulk periodically poled LiNbO₃," *J. Opt. Soc. Am. B.* 12 (11), 2102-2116, 1995.
- [8] D. Huang, E. Swanson, C. Lin, J. Schuman, W. Stinson, W. Chang, M. Hee, T. Flotte, K. Gregory, C. Puliafito, and J. G. Fujimoto, "Optical coherence tomography," *Sci.* 254 (5035), 1178-1181, 1991.
- [9] C.-H. Li, A. J. Benedick, P. Fendel, A. G. Glenday, F. X. Kärtner, D. F. Phillips, D. Sasselov, A. Szentgyorgyi, and R. L. Walsworth, "A laser frequency comb that enables radial velocity measurements with a precision of 1 cm s⁻¹," *Nat.* 452, 610-612, 2008.
- [10] C. V. Shank, "Investigation of ultrafast phenomena in the femtosecond time domain," *Sci.* 233 (4770), 1276-1280, 1986.
- [11] A. H. Zewail, "Laser femtochemistry," *Sci.* 242 (4886), 1645-1653, 1988.
- [12] V. Sundström, "Femtobiology," *Annu. Rev. Phys. Chem.* 59, 53-77, 2008.
- [13] D. J. Jones, S. A. Diddams, J. K. Ranka, A. Stentz, R. S. Windeler, J. L. Hall, and S. T. Cundiff, "Carrier-envelope phase control of femtosecond modelocked lasers and direct optical frequency synthesis," *Sci.* 288 (5466), 635-639, 2000.
- [14] R. Holzwarth, T. Udem, T. W. Hansch, J. C. Knight, W. J. Wadsworth, and P. S. J. Russell, "Optical frequency synthesizer for precision spectroscopy," *Phys. Rev. Lett.* 85 (11), 2264-2267, 2000.
- [15] E. Esarey, C. B. Schroeder, and W. P. Leemans, "Physics of laser-driven plasma-based electron accelerators," *Rev. Mod. Phys.* 81(3), 1229-1285, 2009.
- [16] S. A. Akhmanov, A. I. Kovrigin, A. S. Piskarskas, V. V. Fadeev, and R. V. Khokhlov, "Observation of parametric amplification in the optical range," *JETP Lett.* 2, 191-193 (1965).
- [17] J. A. Giordmaine, and R. C. Miller, "Tunable Coherent Parametric Oscillation in LiNbO₃ at Optical Frequencies," *Phys. Rev. Lett.* 14(24), 973-976 (1965).
- [18] M. Bass, P. A. Franken, A. E. Hill, C. W. Peters, and G. Weinreich, "Optical Mixing," *Phys. Rev. Lett.* 8(1), 18 (1962).
- [19] S. Guha, and J. Falk, "The effects of focusing in the three-frequency parametric upconverter," *J. Appl. Phys.* 51, 50-60 (1980).
- [20] P. B. Corkum, "Plasma perspective on strong field multiphoton ionization," *Phys. Rev. Lett.* 71(13), 1994-1997 (1993).
- [21] P. Antoine, A. L'Huillier, and M. Lewenstein, "Attosecond Pulse Trains Using High-Order Harmonics," *Phys. Rev. Lett.* 77(7), 1234-1237 (1996).

- [22] Ch. Spielmann, N. H. Burnett, S. Sartania, R. Koppitsch, M. Schnürer, C. Kann, M. Lenzner, P. Wobrauschek, and F. Krausz, "Generation of Coherent X-rays in the Water Window Using 5-Femtosecond Laser Pulses," *Science* 278(5338), 661-664 (1997).
- [23] R. R. Alfano, and S. L. Shapiro, "Observation of Self-Phase Modulation and Small-Scale Filaments in Crystals and Glasses," *Phys. Rev. Lett.* 24(11), 592-594 (1970).
- [24] R. H. Stolen, and C. Lin, "Self-phase-modulation in silica optical fibers," *Phys. Rev. A* 17(4), 1448-1453 (1978).
- [25] N. Akhmediev, and M. Karlsson, "Cherenkov radiation emitted by solitons in optical fibers," *Phys. Rev. A* 51(3), 2602-2607 (1995).
- [26] S. Adachi, N. Ishii, Y. Nomura, Y. Kobayashi, A. Kosuge, J. Itatani, T. Kanai, S. Watanabe, D. Yoshitomi, and K. Torizuka, "CEP control of few-cycle multi-mJ OPCPA system for attosecond harmonics generation," *CLEO (Optical Society of America, 2009)* pp. 1-2.
- [27] S. Hädrich, M. Krebs, A. Hoffmann, A. Klenke, J. Rothhardt, J. Limpert, and A. Tünnermann, "Exploring new avenues in high repetition rate table-top coherent extreme ultraviolet sources," *Light Sci. Appl.* 4(8), e320, 2015.
- [28] C. M. Heyl, C. L. Arnold, A. Couairon and A. L'Huillier, "Introduction to macroscopic power scaling principles for high-order harmonic generation," *J. Phys. At. Mol. Opt. Phys.* 50(1), 013001, 2017.
- [29] M. D. Seaberg, D. E. Adams, E. L. Townsend, D. A. Raymondson, W. F. Schlotter, Y. Liu, C. S. Menoni, L. Rong, C. Chen, J. Miao, H. C. Kapteyn, and M. M. Murnane, "Ultrahigh 22 nm resolution coherent diffractive imaging using a desktop 13 nm high harmonic source," *Opt. Express* 19 (23), 22470-22479 (2011).
- [30] T. Rohwer, S. Hellmann, M. Wiesenmayer, C. Sohrt, A. Stange, B. Slomski, A. Carr, Y. Liu, L. M. Avila, M. Källäne, S. Mathias, L. Kipp, K. Rossnagel, and M. Bauer, "Collapse of long-range charge order tracked by time-resolved photoemission at high momenta," *Nat.* 471(7339), 490-493, 2011.
- [31] G. Ndashimiye, S. Ghimire, M. Wu, D. A. Browne, K. J. Schafer, M. B. Gaarde, and D. A. Reis, "Solid-state harmonics beyond the atomic limit," *Nat.* 534(7608), 520-523, 2016.
- [32] T. Tamaya, A. Ishikawa, T. Ogawa, and K. Tanaka, "Diabatic Mechanisms of Higher-Order Harmonic Generation in Solid-State Materials under High-Intensity Electric Fields," *Phys. Rev. Lett.* 116(1), 016601 (2016).
- [33] C. Heide, T. Higuchi, H. B. Weber, and P. Hommelhoff, "Coherent Electron Trajectory Control in Graphene," *Phys. Rev. Lett.* 121(20), 207401, 2018.
- [34] L. Ju, L. Wang, T. Cao, T. Taniguchi, K. Watanabe, S. G. Loui, F. Rana, J. Park, J. Hone, F. Wang, P. L. McEuen, "Tunable excitons in bilayer graphene," *Sci.* 358(6365), 907-910, 2017.
- [35] W. P. Putnam, R. G. Hobbs, P. D. Keathley, K. K. Berggren, and F. X. Kärtner, "Optical-field-controlled photoemission from plasmonic nanoparticles," *Nat. Phys.* 13, 335-339, 2017.
- [36] T. Rybka, M. Ludwig, M. F. Schmalz, V. Knittel, D. Brida, and A. Leitenstorfer, "Sub-cycle optical phase control of nanotunnelling in the single-electron regime," *Nat. Photonics* 10(10), 667-670, 2016.
- [37] M. F. Ciappina, J. A. Pérez-Hernández, A. S. Landsman, W. A. Okell, S. Zherebtsov, B. Förg, J. Schötz, L. Seiffert, T. Fennel, T. Shaaran, T. Zimmermann, A. Chacón, R. Guichard, A. Zair, J. W. G. Tisch, J. P. Marangos, T. Witting, A. Braun, S. A. Maier, L. Roso, M. Krüger, P. Hommelhoff, M. F. Kling, F. Frausz, and M. Lewenstein, "Attosecond physics at the nanoscale," *Rep. Prog. Phys.* 80(5), 054401, 2017.
- [38] D. Hoff, M. Krüger, L. Maisenbacher, A. M. Sayler, G. G. Paulus, and P. Hommelhoff, "Tracing the phase of focused broadband laser pulses," *Nat. Phys.* 13(10), 947-951, 2017.
- [39] M. Krüger, M. Schenk, and P. Hommelhoff, "Attosecond Emission Dynamics in Nonlinear Photoemission from Metal Tips," in *CLEO/Europe and EQEC 2011 Conference Digest (Optical Society of America, 2011)* p. EG3_5.
- [40] M. Müller, M. Kienel, A. Klenke, T. Gottschall, E. Shestaev, M. Plötner, J. Limpert, and A. Tünnermann, "1 kW 1 mJ eight-channel ultrafast fiber laser," *Opt. Lett.* 41(5), 3439-3442 (2016)
- [41] R. W. Boyd, *Nonlinear optics*, Academic press 2003.

- [42] J. Toulouse, "Optical nonlinearities in fibers: review, recent examples, and systems applications," *J. Lightwave Technol.* 23(11), 3625-3641 (2005).
- [43] R. Hellwarth, J. Cherlow, and T. -T. Yang, "Origin and frequency dependence of nonlinear optical susceptibilities of glasses," *Phys. Rev. B* 11(2), 964-967 (1975).
- [44] R. Hellwarth, "Third-order optical susceptibilities of liquids and solids," *Prog. Quant. Electron.* 5, 1-68 (1977).
- [45] A. C. S. van Heel, "A New Method of transporting Optical Images without Aberrations," *Nat.* 173, 39, 1954.
- [46] K. C. Kao, and G. A. Hockham, "Dielectric-fibre surface waveguides for optical frequencies," *Proc. Inst. Elect. Eng.* 113, 1151, 1966.
- [47] K. C. Kao, and T. W. Davies, "Spectrophotometric studies of ultra low loss optical glasses I: single beam method," *J. Phys. E* 2(1), 1063-1068, 1968.
- [48] D. Gloge, "Weakly guiding fibers," *Appl. Opt.* 10(10), 2252-2258, 1971.
- [49] W. A. Gambling, "The rise and rise of optical fibers", *IEEE J. Sel. Top. Quantum Electron.* 6(6), 1084-1093, 2000.
- [50] K. Jürgensen, "Dispersion-optimized optical single-mode glass fiber waveguides," *Appl. Opt.* 14(1), 163, 1975.
- [51] T. A. Birks, J. C. Knight, and P. St. J. Russell, "Endlessly single-mode photonic crystal fiber," *Opt. Lett.* 22(13), 961-963, 1997.
- [52] J. C. Knight, T. A. Birks, R. F. Cregan, P. S. J. Russell, and P. D. de Sandro, "Large mode area photonic crystal fibre," *Electron. Lett.* 34(13), 1347-1348, 1998.
- [53] G. P. Agrawal, *Nonlinear Fiber Optics*, Academic press 2000.
- [54] D. J. Kaup, and A. C. Newell, "An exact solution for a derivative nonlinear Schrödinger equation," *J. Math. Phys.* 19(4), 798-801, 2008.
- [55] R. Hirota, "Exact envelope-soliton solutions of a nonlinear wave equation," *J. Math. Phys.* 14(7), 805-809, 1973.
- [56] S. B. Poole, D. N. Payne, and M. E. Fermann, "Fabrication of low loss optical fibers containing rare earth ions," *Electron. Lett.* 21(17), 737-738, 1985.
- [57] S. Poole, D. Payne, R. Mears, M. Fermann, and R. Laming, "Fabrication and characterization of low-loss optical fibers containing rare-earth ions," *J. Lightwave Technol.* 4(7), 870-876, 1986.
- [58] B. K. Garside, and T. K. Lim, "Laser mode locking using saturable absorbers," *J. Appl. Phys.* 44(5), 2335-2342, 1973.
- [59] F. W. Wise, A. Chong, and W. H. Renninger, "High-energy femtosecond fiber lasers based on pulse propagation at normal dispersion," *Laser Photonics Rev.* 2(1-2), 58-73, 2008.
- [60] M. E. Fermann, M. J. Andrejco, Y. Silberberg, and M. L. Stock, "Passive mode locking by using nonlinear polarization evolution in a polarization-maintaining erbium-doped fiber," *Opt. Lett.* 18(11), 894-896, 1993.
- [61] K. Tamura, E. P. Ippen, H. A. Haus, and L. E. Nelson, "77-fs pulse generation from a stretched-pulse mode-locked all-fiber ring laser," *Opt. Lett.* 18(13), 1080-1082, 1993.
- [62] M. J. Guy, D. U. Noske, and J. R. Taylor, "Generation of femtosecond soliton pulses by passive mode locking of an ytterbium-erbium figure-of-eight fiber laser," *Opt. Lett.* 18(17), 1447-1449, 1993.
- [63] Y. S. Fedotov, A. V. Ivanenko, S. M. Kobtsev, and S. V. Smirnov, "High average power mode-locked figure-eight Yb fibre master oscillator," *Opt. Express*, 22(25), 31379-31386, 2014.
- [64] D. Brida, G. Krauss, A. Sell, and A. Leitenstorfer, "Ultrabroadband Er: fiber lasers," *Laser Photonics Rev.* 8(3), 409-428, 2014.
- [65] D. Mogilevtsev, T. A. Birks, and P. S. J. Russel, "Group-velocity dispersion in photonic crystal fibres," *Opt. Lett.* 23(21), 1662-1664, 1998.
- [66] H. A. Haus, J. D. Moores, and L. E. Nelson, "Effect of third-order dispersion on passive mode locking," *Opt. Lett.* 18(1), 51-53, 1993.
- [67] T. A. Birks, D. Mogilevtsev, J. C. Knight, P. St. J. Russell, "Dispersion Compensation Using Single-Material Fibers" *IEEE Photonics Technol. Lett.* 11(6), 674-676, 1999.

- [68] L. P. Shen, W. -P. Huang, G. X. Chen, and S. S. Jian, "Design and optimization of photonic crystal fibers for broad-band dispersion compensation," *IEEE Photonics Technol. Lett.* 15(4), 540-542, 2003.
- [69] K. Thyagarajan, R. K. Varshney, P. Palai, A. K. Ghatak, and I. C. Goyal, "A novel design of a dispersion compensating fiber," *IEEE Photonics Tech. Lett.* 8(11), 1510-1512, 1996.
- [70] C. J. Koester, and E. Snitzer, "Amplification in a fiber laser," *Appl. Opt.* 3(10), 1182-1186, 1964.
- [71] R. J. Mears, L. Reekie, I. M. Jauncey, and D. N. Payne, "Low-noise erbium-doped fibre amplifier operating at 1.54 μm ," *Electron. Lett.* 23(19), 1026-1028, 1987.
- [72] M. L. Dakss, and W. Miniscalco, "Fundamental limits on Nd^{3+} -doped fiber amplifier performance at 1.3 μm ," *IEEE Photonics Technol. Lett.* 2(9), 650-652, 1990.
- [73] R. Paschotta, J. Nilsson, A. C. Tropper, and D. C. Hanna, "Ytterbium-Doped Fiber Amplifiers," *IEEE J. Quantum Electron.* 33(7), 1049-1056, 1997.
- [74] J. Limpert, N. Deguil-Robin, I. Manek-Hönniger, F. Salin, F. Röser, A. Liem, T. Schreiber, S. Nolte, H. Zellmer, A. Tünnermann, J. Broeng, A. Petersson, and C. Jakobsen, "High-power rod-type photonic crystal fiber laser," *Opt. Express* 13(4), 1055-1058, 2005.
- [75] R. I. Laming, J. E. Townsend, D. N. Payne, F. Meli, G. Grasso, and E. J. Tarbox, "High-power erbium-doped-fiber amplifiers operating in the saturated regime," *IEEE Photonics Technol. Lett.* 3(3), 253-255, 1991.
- [76] A. Ashkin, J. M. Dziedzic, J. E. Bjorkholm, and S. Chu, "Observation of a single-beam gradient force optical trap for dielectric particles," *Opt. Lett.* 11(5), 288-290, 1986.
- [77] D. Strickland, and G. Mourou, "Compression of amplified chirped optical pulses," *Opt. Commun.* 55(6), 447-449, 1985.
- [78] J. Hein, S. Podleska, M. Siebold, M. Hellwing, R. Bödefeld, R. Sauerbrey, D. Ehrhart, and W. Wintzer, "Diode-pumped chirped pulse amplification to the joule level," *App. Phys. B* 79(4), 419-422, 2004.
- [79] J. Tümmler, R. Jung, H. Stiel, P. V. Nickles, and W. Sandner, "High-repetition-rate chirped-pulse-amplification thin-disk laser system with joule-level pulse energy," *Opt. Lett.* 34(9), 1378-1380, 2009.
- [80] S. Zhou, F. W. Wise, and D. G. Ouzounov, "Divided-pulse amplification of ultrashort pulse," *Opt. Lett.* 32(7), 871-873, 2007.
- [81] M. Hentschel, R. Kienberger, C. Spielmann, G. A. Reider, N. Milosevic, T. Brabec, P. Corkum, U. Heinzmann, M. Drescher, and F. Krausz, "Attosecond metrology," *Nat.* 414, 509-513, 2001.
- [82] M. Krebs, S. Hädrich, S. Demmler, J. Rothhardt, A. Zair, L. Chipperfield, J. Limpert, and A. Tünnermann, "Towards isolated attosecond pulses at megahertz repetition rates," *Nat. Photonics* 7, 555-559, 2013.
- [83] T. Tamaya, A. Ishikawa, T. Ogawa, and K. Tanaka, "Higher-order harmonic generation caused by elliptically polarized electric fields in solid-state materials," *Phys. Rev. B* 94(24), 241107, 2016.
- [84] J. P. Marangos, "High-harmonic generation: Solid progress," *Nat. Phys.* 7, 97-98, 2011.
- [85] Z. G. Lu, P. Campbell, and X. -C. Zhang, "Free-space electro-optics sampling with a high-repetition-rate regenerative amplified laser," *App. Phys. Lett.* 71(5), 593-595, 1997.
- [86] F. Silva, D. R. Austin, A. Thai, M. Baudisch, M. Hemmer, D. Faccio, A. Couairon, and J. Biegert, "Multi-octave super continuum generation from mid-infrared filamentation in a bulk crystal," *Nat. Commun.* 3, 807, 2012.
- [87] A. G. Griffith, R. K. W. Lau, J. Cardenas, Y. Okawachi, A. Mohanty, R. Fain, Y. H. D. Lee, M. Yu, C. T. Phare, C. B. Poitras, A. L. Gaeta, and M. Lipson, "Silicon-chip mid-infrared frequency comb generation," *Nat. Commun.* 6, 6299, 2015.
- [88] C. Erny, K. Moutzouris, J. Biegert, D. Kühlke, F. Adler, A. Leitenstorfer, and U. Keller, "Mid-infrared difference-frequency generation of ultrashort pulses tunable between 3.2 and 4.8 μm from a compact fiber source," *Opt. Lett.* 32(9), 1138-1140.
- [89] D. Brida, C. Manzoni, G. Cirimi, M. Marangoni, S. D. Silvestri, and G. Cerullo, "Generation of broadband mid-infrared pulses from an optical parametric amplifier," *Opt. Express*, 15(23), 15035-15040, 2007.

- [90] M. K. Reed, and M. K. S. Shepard, "Tunable infrared generation using a femtosecond 250 kHz Ti:sapphire regenerative amplifier," *IEEE J. Quantum Electron.* 32(8), 1273-1277, 1996.
- [91] N. Leindecker, A. Marandi, R. L. Byer, and K. L. Vodopyanov, "Broadband degenerate OPO for mid-infrared frequency comb generation," *Opt. Express* 19(7), 6296-6302, 2011.
- [92] A. Ruehl, A. Marcinkevicius, M. E. Fermann, and I. Hartl, "80 W, 120 fs Yb-fiber frequency comb," *Opt. Lett.* 35(18), 3015-3017, 2010.
- [93] Y. Ma, F. Meng, Y. Liu, F. Zhao, G. Zhao, A. Wang, and Z. Zhang, "Visible astro-comb filtered by a passively stabilized Fabry-Perot cavity," *Rev. Sci. Instrum.* 90, 013102, 2019.
- [94] A. Vernaleken, J. Weitenberg, T. Sartorius, P. Russbueldt, W. Schneider, S. L. Stebbings, M. F. Kling, P. Hommelhoff, H. -D. Hoffmann, R. Poprawe, F. Krausz, T. W. Hänsch, and T. Udem, "Single-pass high-harmonic generation at 20.8 MHz repetition rate," *Opt. Lett.* 36(17), 3428-3430, 2011.
- [95] J. Rothhardt, M. Krebs, S. Hädrich, S. Demmler, J. Limpert, and A. Tünnermann, "Absorption-limited and phase-matched high harmonic generation in the tight focusing regime," *New J. Phys.* 16, 033022, 2014.
- [96] A. Cabasse, G. Machinet, A. Dubrouil, E. Cormier, and E. Constant, "Optimization and phase matching of fiber-laser-driven high-order harmonic generation at high repetition rate," *Opt. Lett.* 37(22), 4618-4620, 2012.
- [97] T. Eidam, S. Hanf, E. Seise, T. V. Adersen, T. Gabler, C. Wirth, T. Schreiber, J. Limpert, and A. Tünnermann, "Femtosecond fiber CPA system emitting 830 W average output power," *Opt. Lett.* 35(2), 94-96, 2010.
- [98] W. Liu, D. N. Schimpf, T. Eidam, J. Limpert, A. Tünnermann, F. X. Kärtner, and G. Chang, "Pre-chirp managed nonlinear amplification in fibers delivering 100 W 60 fs pulses," *Opt. Lett.* 40(2), 151-154, 2015.
- [99] J. S. Feehan, J. H. V. Price, T. J. Butcher, W. S. Brocklesby, J. G. Frey, and D. J. Richardson, "Efficient high-harmonic generation from a stable and compact ultrafast Yb-fiber laser producing 100 μ J, 350 fs pulses based on bendable photonic crystal fiber," *Appl. Phys. B* 123(1), 43, 2017.
- [100] A. Fernández, L. Zhu, A. J. Verhoef, D. Sidorov-Biryukov, A. Pugzlys, A. Galvanauskas, F. Ö. Ildaly, and A. Baltuška, "Pulse fidelity control in a 20- μ J sub-200-fs monolithic Yb-fiber amplifier," *Laser Phys.* 21, 1329-1335, 2011.
- [101] Y. Liu, P. Krogen, K. -H. Hong, Q. Cao, P. Keathley, and F. X. Kärtner, "Fiber-amplifier-pumped, 1-MHz, 1- μ J, 2.1- μ m, femtosecond OPA with chirped-pulse DFG front-end," *Opt. Express*, 27(6), 9144-9154, 2019.
- [102] R. Biswas, A. S. Kuar, and S. Mitra, "Process optimization in Nd:YAG laser microdrilling of alumina-aluminium interpenetrating phase composite," *J. Mater. Res. Technol.* 4(3), 323-332, 2015.
- [103] P. P. Pronko, S. K. Dutta, J. Squier, J. V. Rudd, D. Du, G. Mourou, "Machining of sub-micron holes using a femtosecond laser at 800 nm," *Opt. Commun.* 114(1-2), 106-110, 1995.
- [104] D. N. Schimpf, T. Eidam, E. Seise, S. Hädrich, J. Limpert, and A. Tünnermann, "Circular versus linear polarization in laser-amplifiers with Kerr-nonlinearity," *Opt. Express*, 17(21), 18774-18781, 2009.
- [105] A. M. Weiner, *Ultrafast Optics*, John Wiley & Sons Ltd. 2009.
- [106] A. -L. Calendron, H. Çankaya, and F. X. Kärtner, "High-energy kHz Yb:KYW dual-crystal regenerative amplifier," *Opt. Express* 22(20), 24752-24762, 2014.
- [107] K. -H. Hong, J. T. Gopinath, D. Rand, A. M. Siddiqui, S. -W. Huang, E. Li, B. J. Eggleton, J. D. Hybl, T. Y. Fan, and F. X. Kärtner, "High-energy, kHz-repetition-rate, ps cryogenic Yb:YAG chirped-pulse amplifier," *Opt. Lett.* 35(11), 1752-1754, 2010.
- [108] L. E. Zapata, H. Lin, A. -L. Calendron, H. Cankaya, M. Hemmer, F. Reichert, W. R. Huang, E. Grannados, K. -H. Hong, and F. X. Kärtner, "Cryogenic Yb:YAG composite-thin-disk for high energy and average power amplifiers," *Opt. Lett.* 40(11), 2610-2613, 2015.
- [109] D. N. Schimpf, J. Limpert, and A. Tünnermann, "Controlling the influence of SPM in fiber-based chirped pulse amplification systems by using an actively shaped parabolic spectrum," *Opt. Express* 15(25), 16945-16953, 2007.

- [110] A. Chong, H. Liu, B. Nie, B. G. Bale, S. Wabnitz, W. H. Renninger, M. Dantus, and F. W. Wise, "Pulse generation without gain-bandwidth limitation in a laser with self-similar evolution," *Opt. Express*, 20(13), 14213-14220, 2012.
- [111] M. E. Ferman, V. I. Kruglov, B. C. Thomsen, J. M. Dudley, and J. D. Harvey, "Self-Similar Propagation and Amplification of Parabolic Pulses in Optical Fibers," *Phys. Rev. Lett.* 84(26), 6010, 2000.
- [112] S. Witte, and K. S. E. Eikema, "Ultrafast Optical Parametric Chirped-Pulse Amplification," *IEEE J. Sel. Top. Quantum Electron.* 18(1), 296-307, 2011.
- [113] F. Röser, T. Eidam, J. Rothhardt, O. Schmidt, D. N. Schimpf, J. Limpert, and A. Tünnermann, "Millijoule pulse energy high repetition rate femtosecond fiber chirped-pulse amplification system," *Opt. Lett.* 32(24), 3495-3497, 2007.
- [114] F. Röser, J. Rothhardt, B. Ortac, A. Liem, O. Schmidt, T. Schreiber, J. Limpert, and A. Tünnermann, "131 W 220 fs fiber laser system," *Opt. Lett.* 30(20), 2754-2756, 2005.
- [115] A. Braun, S. Kane, and T. Norris, "Compensation of self-phase modulation in chirped-pulse amplification laser systems," *Opt. Lett.* 22(9), 615-617, 1997.
- [116] I. Pupeza, S. Holzberger, T. Eidam, H. Carstens, D. Esser, J. Weitenberg, P. Rußbüldt, J. Rauschenberger, J. Limpert, T. Udem, A. Tünnermann, T. W. Hänsch, A. Apolonski, F. Krausz and E. Fill, "Compact high-repetition-rate source of coherent 100 eV radiation," *Nat. Photon.* 7, 608-612, 2013.
- [117] K. Murari, G. J. Stein, H. Cankaya, B. Debord, F. G r me, G. Cirmi, O. D. M cke, P. Li, A. Ruehl, I. Hartl, K.-H. Hong, F. Benabid, and F. X. K rtner, "Kagome-fiber-based pulse compression of mid-infrared picosecond pulses from a Ho:YLF amplifier," *Optica* 3(8), 816-822, 2016.
- [118] P. Wang, Y. Li, W. Li, H. Su, B. Shao, S. Li, C. Wang, D. Wang, R. Zhao, Y. Peng, Y. Leng, R. Li, and Z. Xu, "2.6 mJ/100 Hz CEP-stable near-single-cycle 4 μ m laser based on OPCPA and hollow-core fiber compression," *Opt. Lett.* 43(9), 2197-2200, 2018.
- [119] G. Fan, T. Bal iunas, T. Kanai, T. Fl ry, G. Andriukaitis, B. E. Schmidt, F. L gar , and A. Baltuška, "Hollow-core-waveguide compression of multi-millijoule CEP-stable 3.2 μ m pulses," *Optica* 3(12), 1308-1311, 2016.
- [120] W. Liu, S. -H. Chia, H. Chung, R. Greinert, F. X. K rtner, and G. Chang, "Energetic ultrafast fiber laser sources tunable in 1030-1215 nm for deep tissue multi-photon microscopy," *Opt. Express* 25(6), 6822-6831, 2017.
- [121] W. Liu, D. N. Schimpf, T. Eidam, J. Limpert, A. T nnermann, F. X. K rtner, and G. Chang, "Pre-chirp managed nonlinear amplification in fibers delivering 100 W, 60 fs pulses," *Opt. Lett.* 40(2), 151-154, 2015.
- [122] P. L. Kelley, "Self-Focusing of Optical Beams," *Phys. Rev. Lett.* 15(26), 1005, 1965.
- [123] M. Neuhaus, H. Fuest, M. Seeger, J. Sch tz, M. Trubetskov, P. Russbueltd, H. D Hoffmann, E. Riedle, Z. Major, V. Pervak, M. F. Kling, and P. Wnuk, "10 W CEP-stable few-cycle source at 2 μ m with 100 kHz repetition rate," *Opt. Express* 26(13), 16074-16085, 2018.
- [124] M. Schultze, T. Binhammer, A. Steinmann, G. Palmer, M. Emons, and U. Morgner, "Few-cycle OPCPA system at 143 kHz with more than 1 μ J of pulse energy," *Opt. Express* 18(3), 2836-2841, 2010.
- [125] D. Brida, C. Manzoni, G. Crimi, M. Marangoni, S. Bonora, P. Villoresi, S. D. Silvestri and G. Cerullo, "Few-optical-cycle pulses tunable from the visible to the mid-infrared by optical parametric amplifiers," *J. Opt.* 12, 013001, 2010.
- [126] F. Tavella, A. Willner, J. Rothhardt, S. H drich, E. Seise, S. D sterer, T. Tschentscher, H. Schlarb, J. Feldhaus, J. Limpert, A. T nnermann, and J. Rossbach, "Fiber-amplifier pumped high average power few-cycle pulse non-collinear OPCPA," *Opt. Express*, 18(5), 4689-4694, 2010.
- [127] K. -H. Hong, S. Huang, J. Moses, X. Fu, C. Lai, G. Cirmi, A. Sell, E. Granados, P. Keathley, and F. X. K rtner, "High-energy, phase-stable, ultrabroadband kHz OPCPA at 2.1 μ m pumped by a picosecond cryogenic Yb:YAG laser," *Opt. Express* 19(16), 15538-15548, 2011.
- [128] B. W. Mayer, C. R. Phillips, L. Gallmann, and U. Keller, "Mid-infrared pulse generation via achromatic quasi-phase-matched OPCPA," *Opt. Express*, 22(17), 20798-20808, 2014.

- [129] O. Chalus, P. K. Bates, M. Smolarski, and J. Biegert, "Mid-IR short-pulse OPCPA with micro-Joule energy at 100 kHz," *Opt. Express* 17(5), 3587-3594, 2009.
- [130] M. Schultze, T. Binhammer, G. Palmer, M. Emons, T. Lang, and U. Morgner, "Multi- μ J, CEP-stabilized, two-cycle pulses from an OPCPA system with up to 500 kHz repetition rate," *Opt. Express* 18(26), 27291-27297, 2010.
- [131] J. Moses, C. Manzoni, S. Huang, G. Cerullo, and F. X. Kärtner, "Temporal optimization of ultrabroadband high-energy OPCPA," *Opt. Express* 17(7), 5540-5555, 2009.
- [132] J. Rothhardt, S. Demmler, S. Hädrich, J. Limpert, and A. Tünnermann, "Octave-spanning OPCPA system delivering CEP-stable few-cycle pulses and 22 W of average power at 1 MHz repetition rate," *Opt. Express* 20(10), 10870-10878, 2012.
- [133] J. M. Dudley, G. Genty, and S. Coen, "Supercontinuum generation in photonic crystal fiber," *Rev. Mod. Phys.* 78, 1135-1184, 2006.
- [134] I. Cristiani, R. Tediosi, L. Tartara, and V. Degiorgio, "Dispersive wave generation by solitons in microstructured optical fibers," *Opt. Express* 12(1), 124-135, 2004.
- [135] D. R. Austin, C. M. D. Sterke, B. J. Eggleton, and T. G. Brown, "Dispersive wave blue-shift in supercontinuum generation," *Opt. Express* 14(25), 11997-12007, 2006.
- [136] M. Erkintalo, G. Genty, and J. M. Dudley, "Giant dispersive wave generation through soliton collision," *Opt. Lett.* 35(5), 658-660, 2010.
- [137] X. Liu, J. Laegsgaard, R. Legorov, A. S. Svane, F. Ö. Ilday, H. Tu, S. A. Boppart, and D. Turchinovich, "Nonlinearity-tailored fiber laser technology for low-noise, ultra-wideband tunable femtosecond light generation," *Photon. Res.* 5(6), 750-761, 2017.
- [138] S. S. Sané, S. Bennetts, J. E. Debs, C. C. N. Kuhn, G. D. Mcdonal, P. A. Altin, J. D. Close, and N. P. Robins, "11 W narrow linewidth laser source at 780nm for laser cooling and manipulation of Rubidium," *Opt. Express* 20(8) pp. 8915-9, 2012.
- [139] F. Kienle, K. K. Chen, S. Alam, C. B. E. Gawith, J. I. Mackenzie, D. C. Hanna, D. J. Richardson, and D. P. Shepherd, "High-power, variable repetition rate, picosecond optical parametric oscillator pumped by an amplified gain-switched diode," *Opt. Express* 18(8), 7602-7610, 2010.
- [140] M. Kienel, A. Klenke, T. Eidam, S. Hädrich, J. Limpert, and A. Tünnermann, "Energy scaling of femtosecond amplifiers using actively controlled divided-pulse amplification," *Opt. Lett.* 39(4), 1049-1052, 2014.
- [141] H. Jacqmin, A. Jullien, B. Mercier, M. Hanna, F. Druon, D. Papadopoulos, and R. Lopez-Martens, "Passive coherent combining of CEP-stable few-cycle pulses from a temporally divided hollow fiber compressor," *Opt. Lett.* 40(5), 709-712, 2015.
- [142] H. Jacqmin, A. Jullien, B. Mercier, and R. Lopez-Martens, "Temporal pulse division in hollow fiber compressors," *J. Opt. Soc. Am. B* 32(9), 1901-1909, 2015.
- [143] S. Zhou, F. W. Wise, and D. G. Ouzounov, "Divided-pulse amplification of ultrashort pulses," *Opt. Lett.* 32(7), 871-873, 2007.
- [144] D. Eimerl, L. Davis, and S. Velsko, "Optical, mechanical, and thermal properties of barium borate," *J. App. Phys.* 62(5), 1968-1983, 1987.
- [145] A. Bruner, D. Eger, M. B. Oron, P. Blau, M. Katz, and S. Ruschin, "Temperature-dependent Sellmeier equation for the refractive index of stoichiometric lithium tantalite," *Opt. Lett.* 28(3), 194-196, 2003.

